TWO-AXIS TORQUE CONTROL OF

BLDC MOTORS FOR ELECTRIC

VEHICLE APPLICATIONS

By

Bradley Shields

University of KwaZulu-Natal

BScEng

2014

Submitted in fulfillment of the academic requirement for the degree of Master of Science in Engineering in the School of Electric, Electronic and Computer Engineering at the University of KwaZulu-Natal, South Africa.

Date: March 1st, 2014

Supervisor: Mr B Burton

Co-Supervisor: Prof R Harley

Final Submission

As the candidate's supervisor I agree to the submission of this thesis.

Supervisor: _____

Mr B Burton

Co-Supervisor: _____

Prof R Harley

I, Bradley Arthur Shields declare that:

a) The research reported in this thesis, except where otherwise indicated, is my original work.

b) This thesis has not been submitted for any degree or examination at any other university.

c) This thesis does not contain other persons' data, pictures, graphs or other information, unless specifically acknowledged as being sourced from other persons.

d) This thesis does not contain other persons' writing, unless specifically acknowledged as being sourced from other researchers. Where other written sources have been quoted, then:

e) Their words have been re-written but the general information attributed to them has been referenced.

f) Where their exact words have been used, their writing has been placed inside quotation marks, and referenced.

g) Where I have reproduced a publication of which I am an author, co-author or editor, I have indicated in detail which part of the publication was actually written by myself alone and have fully referenced such publications.

h) This thesis does not contain text, graphics or tables copied and pasted from the Internet, unless specifically acknowledged, and the source being detailed in the thesis and in the References sections.

Signed: _____

Mr B Shields

DON'T QUIT

When things go wrong as they sometimes will,
When the road you're trudging seems all uphill,
When the funds are low and the debts are high,
And you want to smile, but you have to sigh,
When care is pressing you down a bit,
Rest, if you must, but don't you quit.

Life is queer with its twists and turns,
As every one of us sometimes learns,
And many a failure turns about,
When he might have won had he stuck it out,
Don't give up though the pace seems slow,
You may succeed with another blow.

Success is failure turned inside out,
The silver tint of the clouds of doubt,
And you never can tell how close you are,
It may be near when it seems so far,
So stick to the fight when you're hardest hit,
It's when things seem worst,

That you must not quit.

Author unknown

Abstract

_____

This thesis begins with a literature review focusing on electric vehicle (EV) applications. Systems used for steering, braking and energy storage are investigated, with specific concentration on torque control in various DC and AC motors commonly used in EVs. A final solution for a low-range personal transportation EV in the form of a wheelchair is proposed.

The theme for this thesis is motion control, focusing on a two axis (or two wheel drive) brushless DC hub motor (BLDCHM) EV, with torque and direction control tracking a user reference. The operation principle for a BLDCHM is documented and the dynamic and electrical equations derived. Simulation results for motor response under different load and speed conditions are compared to practical measurements. Current and torque control loops are designed, implemented and tuned on a single-axis test-bed with an induction motor (IM) load coupled via a torque transducer. A Texas Instrument DSP development kit is used for the control algorithm bench testing.

The final control algorithm is then duplicated and expanded in simulation to form a dynamic two-axis system for an electric wheelchair. It incorporates both motor drive and regenerative capabilities. After demonstrating two axis controls for BLDCHMs, a control algorithm is designed simulated and compared to traditional systems. The final solution focuses specifically on an intuitive response to the driver input whilst maintaining direction tracking, even when there is a difference in smoothness of the individual terrains traversed by the left and right wheels. In addition the motor drives are equipped with controllers that ensure regenerative braking in order to recover as much energy as possible when the wheelchair is commanded to decelerate.

Acknowledgments

_____

Table of Contents

_____

List of Figures

_____

_____

List of Tables

_____

List of Symbols and Abbreviations

_____

Abbreviation		Unit
A	Anode	
AC	Alternating Current	amps
AFC	Alkaline Fuel Cells	
Al-Air	Aluminium-Air	
B	Pertaining to electrical equations, it is the flux density	tesla
B	Pertaining to mechanical equations, it is the frictional coefficient	
BDC	Brushed Direct Current	
BEMF	Back Electromotive Force	volts
BLDC	Brushless Direct Current	
BLDCHM	Brushless Direct Current Hub Motor	
BLDCM	Brushless Direct Current Motor	
C	Cathode	
DC	Direct Current	
Deg	Degree – the measure of angle	degrees
DMFC	Direct Methanol Fuel Cells	
DSP	Digital Signal Processors	
D_ω	Offset between left and right BLDCHMs	rad/sec
E	Vector for instantaneous values of induced voltage	volts
E	Instantaneous value for induced voltage	volts
E_a	The induced voltage or back EMF in phase A	volts

E_b	The induced voltage or back EMF in phase B	volts
E_c	The induced voltage or back EMF in phase C	volts
EMF	Electro motive force	volts
EV	Electric vehicle	
EW	Electric wheelchair	
e_i	Error between current reference and feedback	amps
FC	Fuel cell	
$f(\theta e)$	The linear piecewise function describing the back EMF wave of a trapezoidal BLDCM	volts
$Fa(\theta e)$	The linear piecewise function describing the back EMF wave for phase A	volts
$Fb(\theta e)$	The linear piecewise function describing the back EMF wave for phase B	volts
$Fc(\theta e)$	The linear piecewise function describing the back EMF wave for phase C	volts
FET	Field effect transistor	
FOC	Field orientated control	
$Gc(s)$	Controller transfer function	
$Gi(s)$	Inverter transfer function	
$Gp(s)$	Plant transfer function	
GUI	Graphical user interface	
$Hall_1$	Analogue feedback signal from the first Hall effect sensor	volts
$Hall_1$	Analogue feedback signal from the second Hall effect sensor	volts
HEV	Hydrogen electric vehicle	
HBS	Hydraulic braking system	

I	Vector for instantaneous values of current	amps
I_t	Total current from the inverter	amps
I_a	The current though phase A	amps
I_b	The current though phase B	amps
I_c	The current though phase C	amps
i_{ds}	d component of the stator current vector	amps
i_{qs}	q component of the stator current vector	amps
I_{ref}	Reference current	amps
ICE	Internal combustion engine	
ICEV	Internal combustion engine vehicle	
IGBT	Insulated-gate bipolar transistor	
IM	Induction motor	
J	The motor inertia	kg.m^2
K_p	Proportional gain	
K_i	Integral gain	
K_t	The motor torque constant	N-m/A
K_v	The motor speed constant	rad/V.s
ℓ	Liter	liters
l	Rotor length	m
L	Average phase inductance	henry
L_a	The self inductance of phase A	henry
L_b	The self inductance of phase B	henry
L_c	The self inductance of phase C	henry
L_{ab}	The mutual inductance between phase A and phase B	henry

L_{ac}	The mutual inductance between phase A and phase C	henry
L_{bc}	The mutual inductance between phase B and phase C	henry
L_t	Total inductance	henry
$L1$	Abbreviation for the difference between the L and M	henry
Li-Ion	Lithium-ion	
Li-Polymer	Lithium-polymer	
M	Mutual inductance	henry
MCFC	Molten carbonate fuel cell	
MMF	Magnetomotive force	amps
MOSFET	Metal-oxide-semiconductor field-effect transistor	
MSc	Master of science	
MUT	Motor under test	
N	The number of windings per phase	
NASA	National Aeronautics and Space Administration	
$Na/NiCl_2$	Sodium/nickel chloride	
Na/S	Sodium/sulphur	
Nd	Neodymium	
NdFeB	Neodymium iron and boron alloy	
Ni-Cd	Nickel cadmium	
Ni-Zn	Nickel zinc	
NiMH	Nickel-metal hydride	
NRF	National research foundation	
P	Number of pole pares	
PAFC	Phosphoric acid fuel cells	

PCB	Printed circuit board	
PI	Proportional and integral	
PM	Permanent magnet	
PMDCM	Permanent magnet direct current motor	
PMSM	Permanent magnet synchronous motor	
PWM	Pulse width modulation	
r	The internal radius of the rotor	meters
rad	Radian	rad
R	Average phase resistance	ohms
Ra	Resistance of phase A	ohms
Rb	Resistance of phase B	ohms
Rc	Resistance of phase C	ohms
RR	Regeneration ratio	
S_f	User defined sensitivity factor	
SCIM	Squirrel cage induction motor	
SmCo	Samarium cobalt	
SOFC	Solid oxide fuel cells	
SPFC	Solid polymer fuel cell	
SRM	Switched reluctance motor	
SSE	State space equation	
THD	Total harmonic distortion	
T_e	The electrical torque	N-m
T_l	The load torque	N-m
T_{L_elec}	Electrical output torque produced by the left BLDCHM	N-m

List of Symbols and Abbreviations

$T_{L\_limit\_MAX}$	The maximum torque implemented by the low pass limiter	N-m
T_{L_ref}	Torque reference for the left BLDCHM controller	N-m
T_{L_error}	The error between the torque reference for the left BLDCHM controller, and the torque feedback	N-m
T_{ref}	Torque reference	N-m
T_{R_elec}	Electrical output torque produced by the right BLDCHM	N-m
T_{R_ref}	Torque reference for the right BLDCHM controller	N-m
T_{R_error}	The error between the torque reference for the right BLDCHM controller, and the torque feedback	N-m
USABC	United states advanced battery consortium	
USD	United states dollar	
V	Vector for instantaneous values of voltage	volts
v	The rotational velocity of the motor	m/s
V_{an}	Voltage over the A phase to the neutral point	volts
V_{bn}	Voltage over the B phase to the neutral point	volts
V_{cn}	Voltage over the C phase to the neutral point	volts
V_n	Neutral point voltage within a BLDCM	
V_0	Inverter reference voltage	volts
Vn_0	Potential between the BLDCHM neutral point and the inverter reference potential	volts
VRLA	Valve-regulated lead-acid	
W	Watt	watts
ω_m	The rotor's mechanical angular velocity	rad/sec
ω_b	Rotor's base angular velocity	rad/sec
ω_l	Left motor's angular velocity	rad/sec

ω_r	Right motor's angular velocity	rad/sec
Zn-Air	Zinc-air	
°C	Degrees Celsius	
+Vcc	Supply maximum potential	volts
-Vcc	Supply minimum potential	volts
$\boldsymbol{I}_s$	Current vector	amps
$\boldsymbol{\lambda}_f$	Rotor flux linkage vector	webber*turns
λ_{dr}	d component of the rotor flux linkage vector	webber*turns
λ_{qr}	q component of the rotor flux linkage vector	webber*turns
Φ	The flux linkage between the rotor and each phase winding	webber
$\dfrac{d}{dt}$	Differential operator with respect to time	s^{-1}
θe	The motor electrical angular position	rad
θ_l	The left motor electrical angular position	rad
θ_r	The right motor electrical angular position	rad
θ_m	The motor mechanical angular position	rad

List of Symbols and Abbreviations

Chapter 1 - Introduction

_____

1.1   **General**

With the continuous rising demand on fossil fuels, and the exorbitant costs associated with manufacture and distribution, more and more emphasis is being placed on systems that are both environmentally friendly and efficient. This is placing a more urgent focus on the control and implementation of electrical motors in comparison to their internal combustion counterparts. The concept of an electric vehicle (EV) was first implemented in 1897. Many different types of EVs have been developed since then for applications ranging from industry to public as well as personal transportation [1].

Over the years, research and the demand by industry have advanced the semiconductor control technology, power electronics and motor designs in terms of functionality, availability, cost and efficiency, which have all contributed to improved dynamic performance at lower costs of adjustable speed motor drives. This thesis focuses on the feasibility of a short range personal transportation EV and describes the research available in this field. A mechanical and electrical design is proposed utilizing two brushless DC hub motors (BLDCHMs). The theme of the thesis is torque control of a BLDCHM and the control algorithms are designed, simulated and compared to practical results for a single motor. Once accurate control of the BLDCHM is shown, the feasibility of using two such motors to achieve steering of an EV, is simulated. The final results for a novel steering solution are documented.

The structure of this thesis is as follows:

- Chapter 2 – Literature Review: This chapter describes the available research regarding EV applications. The fields of research include motor and braking systems, torque control of various alternating current (AC) and direct current (DC) electric motors (EMs), motor drive technologies, energy sources and steering solutions. Based on this research a brushless DC hub motor is selected for this investigation, together with an appropriate power electronic circuit topology.

- Chapter 3 – BLDC Hub Motor Operation Theory: This chapter provides more detail on the BLDCHM selected in Chapter 2. The mechanical structure of the rotor and stator are

described as well as the position-based electrical commutation for both driving of this machine as a motor and regenerating with it as a generator. The inverter topology and switching sequences are also developed.

- Chapter 4 – Dynamic and Electrical Model of a BLDCHM: In this chapter a mathematical analysis of the BLDCHM and the power-electronic inverter is performed using an a,b,c reference axis approach for developing the equations. The final state space equation for a three-phase, star-wound, trapezoidal back EMF BLDCHM is obtained which describes the mechanical and electrical dynamic behavior of the BLDCHM.

- Chapter 5 – BLDCM Simulation and Controller Design: Based on the final state space equation developed in Chapter 4, a simulation model of the BLDCHM is developed using VisSim v6.0, a simulation package and embedded control developer from Texas Instruments®. A comparison of the simulated results for motor current, torque and rotational speed is compared to practical measurements on the motor and its inverter drive, illustrating the correct modeling and simulation of a BLDCHM. A torque controller based on current control is then designed and implemented on a Texas Instruments® DSP. Once again the simulated and practical results are compared. A sensorless torque controller under regeneration is then developed.

- Chapter 6 – Electric Vehicle Steering Algorithm: This chapter summarizes the requirements for an electric wheelchair (EW) to have a response to the control input which is intuitive for the user. The traditional control systems in an EW are simulated and compared with two novel systems proposed in this research, which are designed to provide user vector tracking whilst maintaining an ergonomic response.

1.2   **Novel contribution**

The major and novel finding of this investigation is the development of a steering methodology for an electric wheel chair with two BLDCHMs which ensures that the wheelchair accurately tracks the directional command of the user, irrespective of differences in the smoothness of the individual terrains traversed by the left and right wheels. In addition the motor drives are equipped with controllers that ensure regenerative braking in order to recover as much energy as possible when the vehicle is commanded to decelerate.

The control algorithm utilizes a torque controller on one motor and a speed controller on the second. Whilst this control configuration may not seem to be intuitive, when coupled with the

designed control algorithm, all of the user requirements for an ergonomic driving experience with direction tracking are met. The development for this solution and the simulated results are documented in Chapter 6.

1.3   **Summary**

This chapter has described the focus of this thesis, and has summarized the contents of each chapter, as well as the novel contributions of this thesis. Chapter 2 describes the literature review of motor drive topology and steering solutions for electric vehicles and makes a final selection of the topologies to be applied in this research.

Chapter 2   -   Literature Review

2.1   Introduction

This thesis describes the research, simulation and practical implementation of a battery powered, four wheeled, personal transportation vehicle. Figure 2.1 below shows the design of the electric vehicle (EV), which has two independently driven wheels in the front and two freewheeling wheels at the rear which are able to change orientation and speed independently. The user controls the vehicle via a joystick that controls the speed and direction of motion. The theme for this thesis is Motion Control and concentrates primarily on achieving a smooth and accurate control of the vehicle.

1 - Freewheeling rear wheels
2 - Front left hub motor
3 - Front right hub motor
4 - Joystick
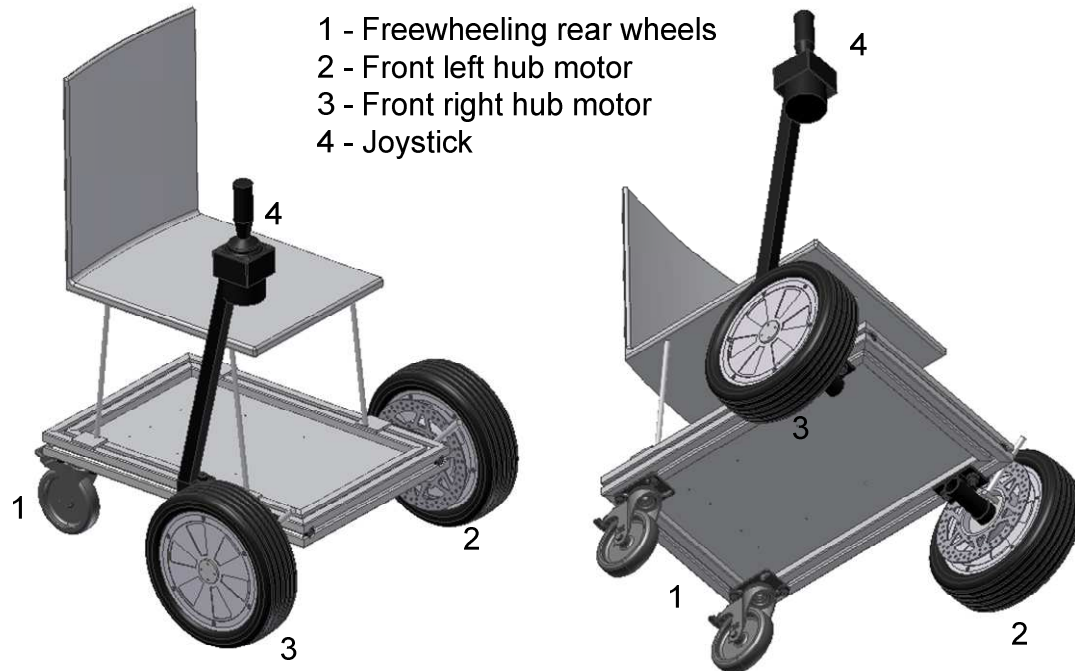
Figure 2.1 Electric vehicle design layout

The primary objectives include:

a) The correct commutation and torque control of the motors.

b) A commutation algorithm which provides two axis control (x and y directions) as the speed differential between the independent front hub motors is used to steer the EV.

c) Use of the system to increase battery life, thereby increasing the total travel distance of the EV.

d) The implementation of a braking scheme, which continues to allow for steering.

The secondary objectives include:

a) A prototype solution to demonstrate the practical implementation.

b) The design and manufacturing of custom circuitry for both control and power electronics.

c) The solution should be robust, light weight and compact with low maintenance.

This chapter reviews the published literature covering the proposed system. Based on this review, the design process of motor selection, hardware selection and control schemes is explored, and the final design selection is documented.

2.2   **Historical development**

The concept of an EV is not new. The first appearance of an EV was in 1897 [1] when "The London Electric Cab Company" was established. However these early EVs proved to be unreliable with limited traveling range and so the electric motors were replaced with an internal combustion engine (ICE).

However the development in battery, motor and drive technology over the years has made the implementation of EVs more realistic, though affordability is still in question. Advantages of using an electric motor (EM) over the ICE and hydraulic braking system (HBS) are summarized below [1, 2].

a) In an EM, the torque response is typically in the millisecond range and 10-1000 times faster than an ICE or HBS. This fast response allows for feedback control to change vehicle characteristics without the user having to adjust their input. Two mechanical systems which already use this principle in vehicles are "Anti Lock Braking Systems" when under deceleration and a "Traction Control System" when under acceleration. By

implementing these systems on an EV, the response time can be greatly reduced as the torque response is faster and this increases performance.

b) A distributed motor location can be achieved by attaching an independent EM to each wheel, (two motors for a two-wheel-drive vehicle, or four motors for a four-wheel-drive vehicle). This allows control of independently driven wheels, increasing the performance of the vehicle systems such as "Vehicle Stability Control" and "Direct Yaw Control".

c) Estimating the torque developed by an EM is simpler than for an ICE or HBS. This estimation in turn allows the driving force between the tyre and the road surface to be estimated which can be used to warn the driver of a change in road conditions such as snow on the road for example.

d) The conventional diesel, petrol and liquid petroleum gas propelled vehicles suffer from carbon emissions. Hydrogen motors overcome this problem by simply having water as an emission. Moreover all combustion engines also contribute to noise pollution, which an EV will not do. Even when taking into consideration the pollution caused by power plants producing electric power for EVs, the total environmental impact of an EV is still less than that of an ICE [2].

The two primary factors contributing to the viability of EVs are the cost and operational range [1]. Research to increase operational range is extensive, focusing on advancing the battery technology. However both the specific energy and the energy density of batteries cannot compare with that of gasoline. As a result, research into fuel cells has also increased. In order to reduce the cost of EVs, better design solutions are being implemented for motors, drive technology, power management, regeneration of energy and battery chargers.

2.3   Motor and drive topology for EVs

EVs have been developed in many different shapes and sizes for a multitude of applications ranging from short distance commuting (as with the Segway), city and highway travel (such as the General Motors EV1) and even space exploration (on NASA's Apollo missions). As a result many variations have been developed and some are evaluated in this section. The following fundamental aspects to the EV are considered [1].

a) Drive and braking systems with electric motors, to create acceleration and deceleration of the EV.

b) Portable energy sources to power the electric motors.

c) Motor control systems between the power source and motors with user input.

2.3.1 Motor and braking systems

An EM provides driving torque in EVs for bi-directional operation. Thus the EM under control produces torque by converting electrical energy to mechanical energy, to follow either a desired speed or position set point [3]. An EM can also be used as a generator, converting the vehicle's momentum into electrical energy, thus allowing for an efficient braking system. This electrical energy can then be stored back in the power source if this is allowed (see 2.3.2 below) or dissipated as heat into the atmosphere with a braking resistor. Electric motors (EMs) are connected to the power source via flexible electrical cables, thus they have the potential to not suffer from positioning limitations inside the vehicle otherwise caused by mechanical linkage. As a result six alternative configurations are typically used when designing EVs, as shown in Figure 2.2 [1].
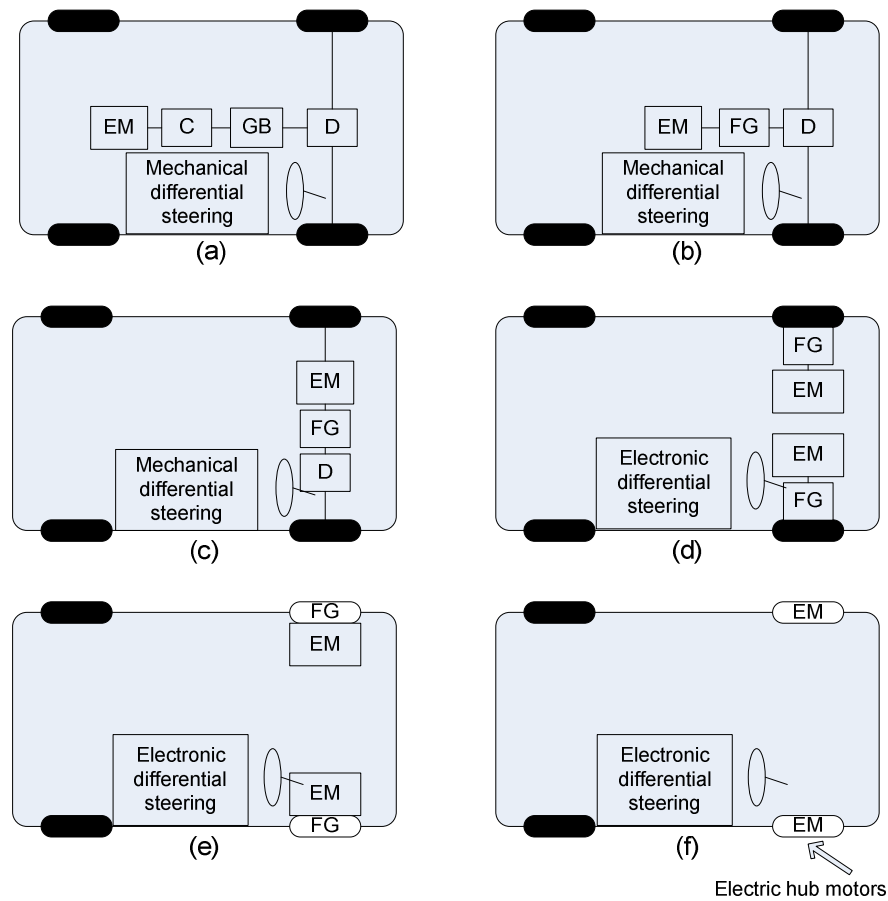
Figure 2.2 EV drive configurations [1]

where:

- EM – Electric Motor.
- C – Clutch.
- G – Gearbox.
- FG – Fixed Gearing.
- D – Differential.

The six configurations are for two-front-wheel-drive design but can be extrapolated to a four-wheel-drive design.

a) Figure 2.2 (a) shows the typical layout of an internal combustion engine vehicle (ICEV) converted to an EV. The ICE has been replaced by an EM, but the mechanical clutch, gearbox and differential are still in place. This solution allows for the use of the clutch to shift gears at different speeds providing high torque at low speeds and low torque at high

speeds. The differential is needed for cornering where the inner wheel must rotate slower than the outer wheel because it is covering less distance.

b) Figure 2.2 (b) shows an EM coupled to a fixed gearbox, and then a differential coupled to the wheels. This solution removes the clutch which allows a size and weight reduction. This is possible due to the torque-speed characteristics of an EM, and cannot be achieved with an ICE.

c) Figure 2.2 (c) is identical in operation to Figure 2.2 (b). The system is comparable to a transverse front mounted, front-wheel-driven ICEV. This is the most common configuration used for EVs.

d) In Figure 2.2 (d) the need for a differential, to create a speed offset between the driving wheels, is eliminated. This is possible by running the two separate motors at different speeds. This configuration has a motor and fixed gearbox mechanically coupled to each of the front driving wheels.

e) Figure 2.2 (e) shows a further reduction in the mechanical coupling system, by creating an "in-wheel drive" with the gearbox embedded into the wheel. Planetary gearing is favored as the ratio can be designed to meet the speed requirement of the vehicle and the inline arrangement of input and output shafts.

f) Figure 2.2 (f) shows the simplest of mechanical solutions. The motor is housed within the wheel. The motor has an inner stationary stator and an outer rotor is directly connected to the wheel. By doing this, the control of the motor speed is identical to the wheel speed. This solution is the least prone to mechanical failure and is favored more for low speed personal transportation. This solution also allows for the removal of mechanical steering. The speed differential between the two EMs is used to implement steering as seen for example on an electric wheel chair.

In general the use of a gearbox allows the EM to run at a much higher rotational speed than the wheels. For a given power level, the motor volume and weight decreases linearly as speed increases. Higher speed EMs are therefore much smaller then low speed EMs.

Development in EVs has produced a wide range suitable for a multitude of applications. Figure 2.3 shows those motor types which have potential EV applications. For efficient control in an EV, torque control is needed and a brief description is presented below for each motor.
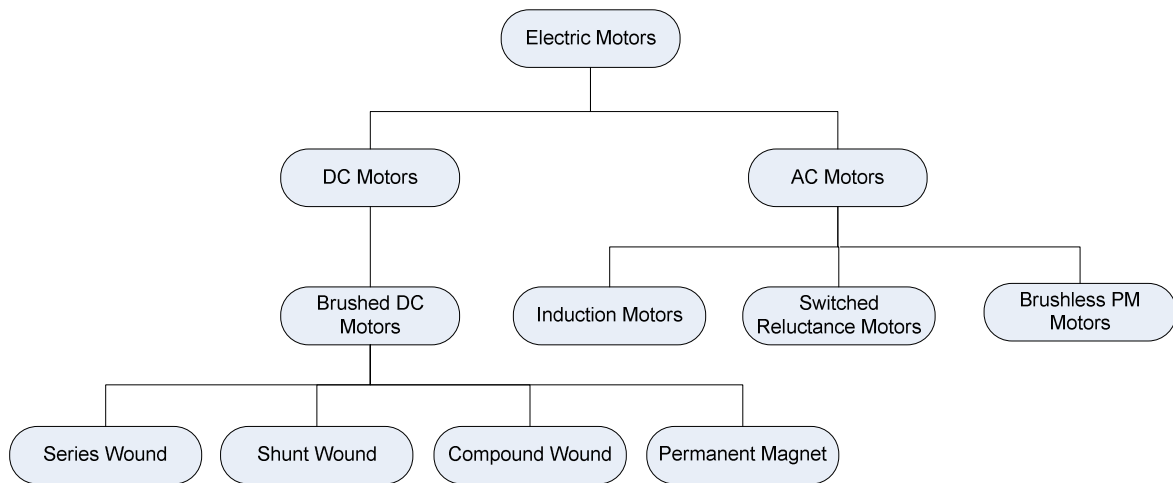
Figure 2.3 Electric motor categorization [4]

2.3.1.1   Direct current motors (DC motors)

A brushed DC motor (BDCM), as the name implies, is designed to work from a DC voltage source. The motor has two fundamental components, the rotor and stator. Typically the stator (fixed portion) houses so-called excitation or field windings which produce an electromagnetic field when energized by the DC supply. The rotating armature (or rotor) is comprised of many individual windings that are energized in turn by a rotating mechanical switch called a commutator. The commutator allows for the energizing of the individual rotor circuits, so that the magnetic field produced by the rotor is stationary in space and at an angle of 90° with respect to the magnetic field created by the stator poles. This angle produces a maximum torque proportional to the product of field current and armature current provided no saturation occurs. The different wiring possibilities between the field and armature provide different classifications, namely shunt or compound DC motors and series DC motors. The field windings can also be replaced by permanent magnets in which case the operating principle remains the same and these motors are called permanent magnet DC motors (PMDCM) [5].
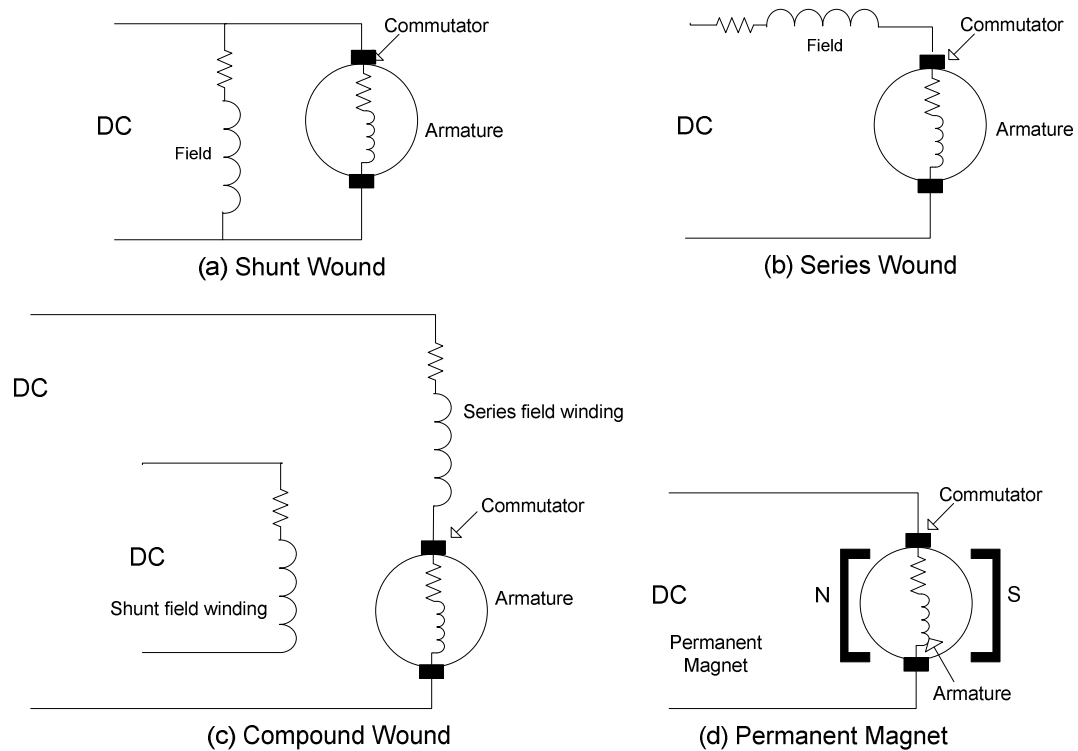
Figure 2.4 Equivalent circuits for different types of brushed DC circuits [5]

i)   Shunt wound DC motor:

      This motor has a parallel connection between the supply, field and armature windings. This
      connection has the advantage of a constant field flux generated by the field windings,
      allowing a nearly constant speed over the available torque range. Effective torque control is
      achieved through either field or armature current control, but varying both field and
      armature current simultaneously increases the complexity of the controller. The preferred
      way of power electronic speed control is to excite the field winding separately and keep the
      field current constant while varying the armature's own separate supply voltage in order to
      control the armature current. This ensures maximum torque for a given value of armature
      current. When the armature supply voltage reaches rated value, it is possible to reduce the
      field current, a condition known as field weakening, in order for the motor to operate at
      higher speeds provided it still produces sufficient torque. Braking is achieved by suitable
      control of the armature current.

ii) Series wound DC motor:

This motor has a series connection between the supply, field and armature windings. This connection provides torque proportional to the square of armature current in the absence of saturation and hence it has the highest output torque per amp relationship in DC motors. In large traction motors the current is typically allowed to rise as high as two or three times the rated value for short periods of time during startup, thus producing up to nine times rated torque. This high torque is desirable when accelerating heavy vehicles from standstill. The disadvantages for this type of motor are that the speed varies wildly depending on the load [38] and with no speed control and no shaft load it is possible for the motor to be damaged due to over-speed. Moreover speed and torque control are more sophisticated.

iii) Compound wound DC motor:

This motor is a hybrid between the series and shunt wound DC motors. The purpose is to combine the best features of both the shunt and the series motors. To achieve this a portion of the field windings is connected in series with the armature windings. The remaining field windings are connected in parallel with the armature windings. The compound wound DC motor thus produces more torque during startup than a shunt wound motor and will not over-speed at no-load like a DC series motor.

iv) Permanent magnet DC motors (PMDCM):

This motor has armature windings and a commutator with brushes, and uses permanent magnets on the stator to produce a constant field flux. The advantage is a linear torque speed characteristic resulting in torque being directly proportional to the armature current and allowing for simple torque control implementation. The permanent magnets also provide additional capabilities as the field flux density is higher than that produced by a traditional field winding. Braking is achieved by suitable control of the armature current. This is not a popular motor due to the commutator and brushes, and gave way to reversing the position of the armature windings and the magnets to form a motor that is then classified as a brushless AC machine.

While the brushed DC motors are simpler to control than AC motors, they are not considered further in this thesis due to the disadvantage of the commutator and the brushes which add weight, volume and require frequent maintenance. The possible candidate motors for EV applications are

therefore the permanent magnet motor family, the induction motors and the switched reluctance machines. These are now considered in turn.

2.3.1.2   Alternating current motors (AC motors)

i)   Permanent magnet (PM) motors in general:

With only one set of windings, in a PM Motor, commutator-less functionality is possible by placing the magnets on the rotor and electrically switching current to the individual field phases on the stator. The PM motor is identical in characteristics to the brushed DC motor, except that it is mechanically inverted as appears Figure 2.5. This allows for the removal of the mechanical commutator, but requires a rotating stator flux. To achieve this rotating flux the current through the stator phases is alternated based on the rotor position. A measurement or estimation of rotor position is therefore essential for switching the stator phases at exactly the correct moment in time.

PM machines are classified into two types depending on the way the stator winding has been wound in order to have either a trapezoidal back EMF or a sinusoidal back EMF. The trapezoidal machine is known as a brushless DC machine (BLDC), and the sinusoidal machine is known as a sinewave PM machine or sometimes just as a PM machine. The BLDC machine has a simpler stator winding configuration and the inverter controller only needs to know the rotor position at sixty degree intervals when commutation has to take place, hence a relatively inexpensive resolver can be mounted on the shaft. The sinewave machine has a more complex distributed stator winding, and the stator current controller needs to know the rotor position very accurately in fine increments and hence a more expensive incremental encoder has to be mounted on the shaft. A sinewave machine can position its rotor more accurately than a BLDC machine and thus the BLDC and sinewave machines each have their own areas of application [6, 7].
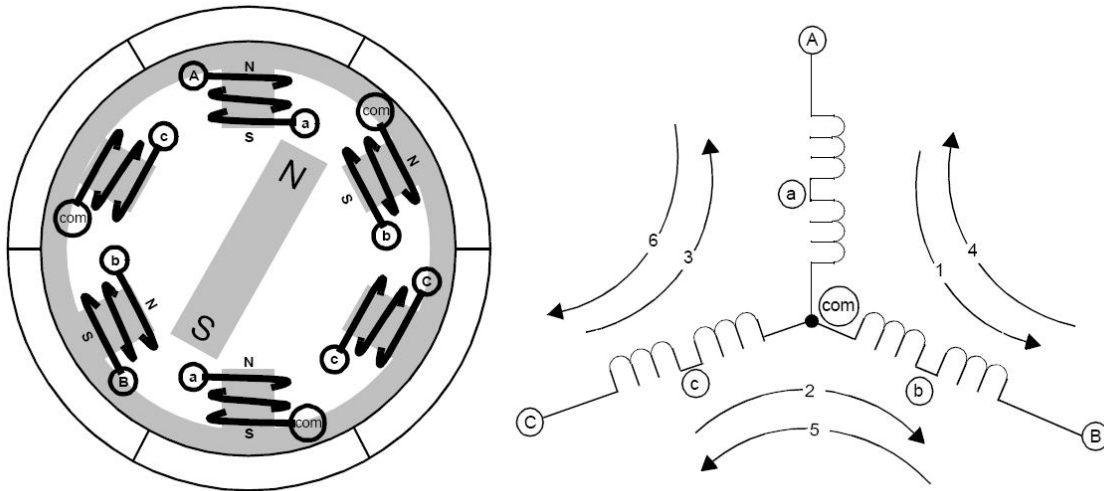
Figure 2.5 Simplified cross sectional view and circuit diagram for a BLDCM [8]

ii)   The induction motor (IM):

Due to its rugged design, the induction motor (IM) is the most widely used commutator-less drive system and in particular, the three phase squirrel cage induction motor (SCIM). The rotor comprises an iron core and aluminium or copper rotor bars, allowing for easy manufacturing [9]. The stator houses either a single phase or a three phase winding. A three phase stator winding carries balanced three phase currents, producing a rotating magnetic field at synchronous speed and constant amplitude. This rotating field induces voltages in the rotor circuits. The consequential rotor currents in turn produce a magnetic field that rotates with respect to the rotor at slip speed, so that this field rotates at the same synchronous speed in space as the stator's magnetic field, but displaced by some angle. Torque is produced by the interaction of the stator and rotor magnetic fields. However the rotor speed has to be less than synchronous speed for motor action and more than synchronous speed for generator action. The difference between the rotor speed and synchronous speed is defined as the slip [10].

While the induction motor is more rugged than the DC motor, its control is more complex. The most effective way of controlling the speed of an IM, is to change the frequency and the flux magnitude in the machine and several schemes are in use. The simplest method is known as "constant volts-per-hertz" or so-called V/f control with the hardware complexity varying depending on the accuracy required. The control requires a relatively simple speed sensor, but can function with speed estimate rather than a real sensor. The V/f control can also work in open-loop without a speed feedback sensor when accuracy is not important, for example when driving a fan or a pump.

For more accuracy than the V/f control with speed feedback, the so called field orientated control (FOC) or vector control method can be used in which the position (rather than speed) and magnitude of the rotating flux (either stator or rotor flux) in the machine are accurately controlled.

FOC enables the three phase IM to have a dynamic performance equal to that of a DC motor. Achieving these dynamics requires a reduction of the complex a,b,c voltages and currents of the squirrel cage induction motor (SCIM) into d,q variables, or first into so-called Space Phasors which can ultimately be reduced to d,q form [12]. Deriving the equations into d,q form makes it easier to understand the method of FOC and its objectives. Special relationships between the machine currents and flux are maintained by the current, speed and position loop controllers which operate on the d,q variables. The FOC method typically needs a shaft encoder [11]. Derivation of the SCIM two-axis or d,q model is not shown here as it is beyond the scope of this thesis but the effects of FOC are examined. The SCIM model show below assumes the following:

a) The magnetic field is linear and the effect of saturation is negligible, which is plausible provided the current in the SCIM does not exceed rated current.

b)   The iron and stray losses are negligible.

c) The air-gap MMFs and fluxes are sinusoidal.

d) The windings are balanced and symmetrical.

e) The distributed windings can be represented by equivalent concentrated windings.

A block diagram for the dynamic equations of a SCIM and the effects of implementing FOC appears below in Figure 2.6 [12].

Figure 2.6 Block diagram representation of the dynamic equations for a SCIM [12]

The objective of FOC is to establish and maintain an explicit angle (α in Figure 2.7) between the stator current vector and the rotor flux vector. This is done by controlling the slip in the SCIM to a value where the rotor flux vector is aligned with the d-axis of the stator current vector [12].
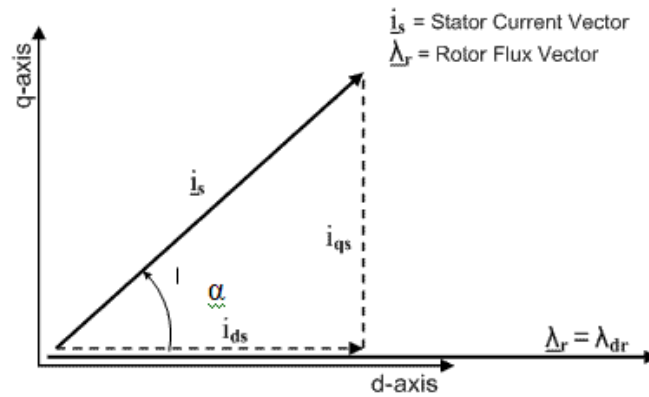
Figure 2.7 Current and flux vectors for a SCIM under FOC [12]

Figure 2.7 shows that the stator current vector has two orthogonal components (i_{ds}, i_{qs}), whilst the rotor flux vector has only one component on the d-axis (λ_{dr}). This means that the q-axis component (λ_{qr}) of the rotor flux vector has to be zero. If FOC is correctly implemented to control λ_{qr} to be zero, then the outputs at points A and B in Figure 2.6 are zero and the outputs at points C and D are equal. This condition allows the bold red lines in Figure 2.6 to be removed thus resulting in Figure 2.8 which is the model of a SCIM under FOC.
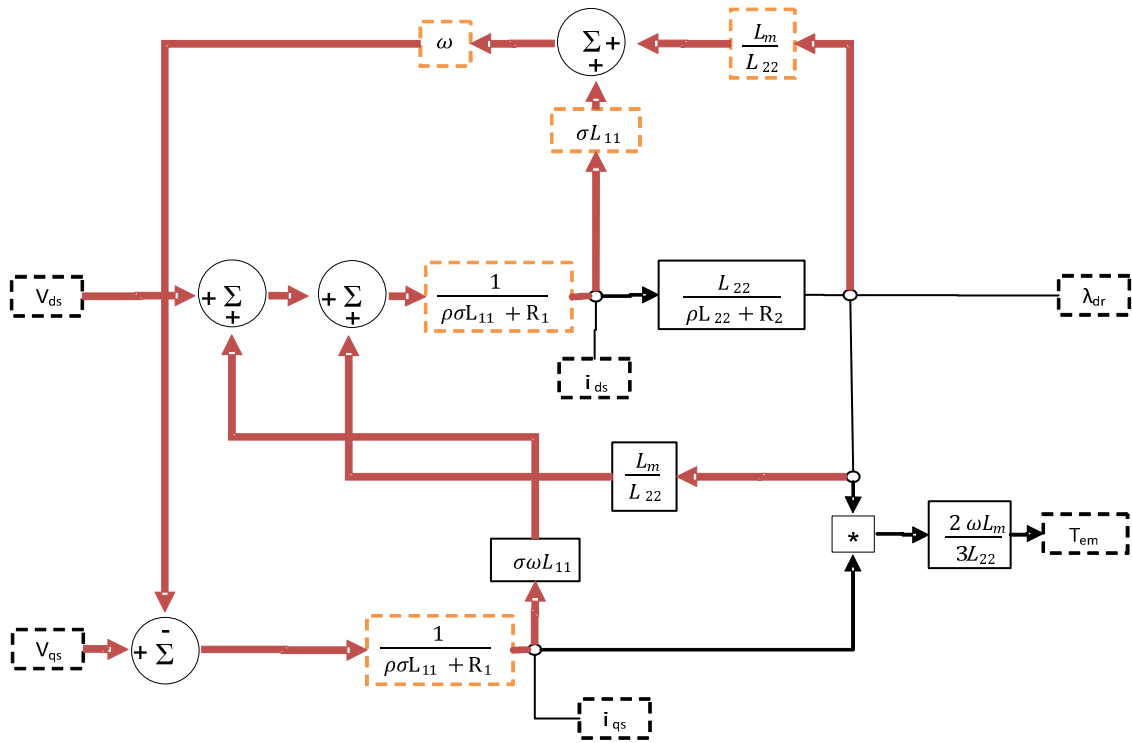
Figure 2.8 Block diagram of a SCIM under FOC [12]

Ref. [12] explains the FOC conditions that allow the bold red lines in Figure 2.8 to be removed, thus resulting in Figure 2.9 in which i_{ds} resembles the field current of a DC machine, and i_{qs} resembles the armature current of a DC machine. These two currents can then be used in the same kind of control loop as would be done on a real DC machine.
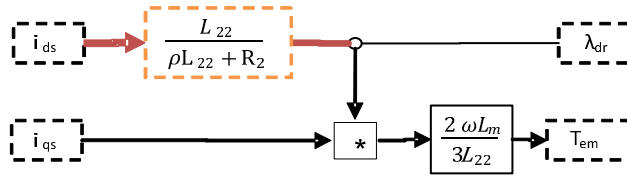
Figure 2.9 Block diagram of a SCIM under FOC, with controlled stator current [12]

Thus the FOC SCIM control strategy becomes similar to that of a DC machine where the value of field flux is controlled by i_{ds} and the motor torque is controlled via armature current i_{qs}. When in addition i_{ds} is a set fixed value, Figure 2.9 reduces to Figure 2.10 in which the electromagnetic torque T_{em} of the motor is solely dependent on the current i_{qs}, reducing the SCIM to an equivalent separately excited DC machine with fixed excitation, or a permanent magnet DC machine, or a BLDC machine.
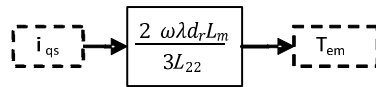
Figure 2.10 Final dynamic structure of a SCIM resulting from FOC [12]

iii)   Switched reluctance motor (SRM):

The torque in a switched reluctance motor (SRM) is not produced by the interaction of two magnetic fields, but rather the distortion of the magnetic field between the electromagnetic stator poles and the laminated sheet rotor which produces a reluctance torque. When comparing the SRM with other AC and DC motors, the following important advantages are noted [12 - 16].

a) Each stator phase winding is independent electrically, mechanically and magnetically from the other phase windings.

b) A laminated sheet rotor has no magnets or conductors, so high speeds can be achieved.

However there are also the following disadvantages [37].

a) A SRM cannot be run from AC mains or a DC bus as each individual coil needs to be electrically commutated.

b) Physically the doubly salient structure (stator and rotor) and the high saturation magnetic properties render non-linear flux per phase, inductance and motor torque that are all functions of rotor position and phase current, making the analysis and control strategies complicated.

c) Torque ripple causes resonant vibrations in the rotor and is a prominent source of acoustic noise during operation.

d) Having no winding on the rotor is an advantage over the induction machine whose rotor bars and/or end rings may eventually crack due to the stress caused by multiple direct online starts. In the IM differential heating and cooling between the rotor bars and laminations occurs, but not in the SRM, thus improving the reliability and increasing output power and torque-inertia ratio of the SRM compared to a similar size IM.

To obtain the magnetic field distortion within the air gap in the SRM, the rotor and stator have a different number of pole pairs and therefore a specialized commutation strategy is needed to generate and maintain torque for rotation (for example a 8/6 SRM refers to an 8 stator poles (4pole pairs) and 6 rotor poles (3 pole pairs) switched reluctance motor). Popular choices are the 6/4 (high speed) or the 8/6 (high torque) [17].

(a) Aligned Position (θ = 0°)   (b) Unaligned Position (θ = 30°)
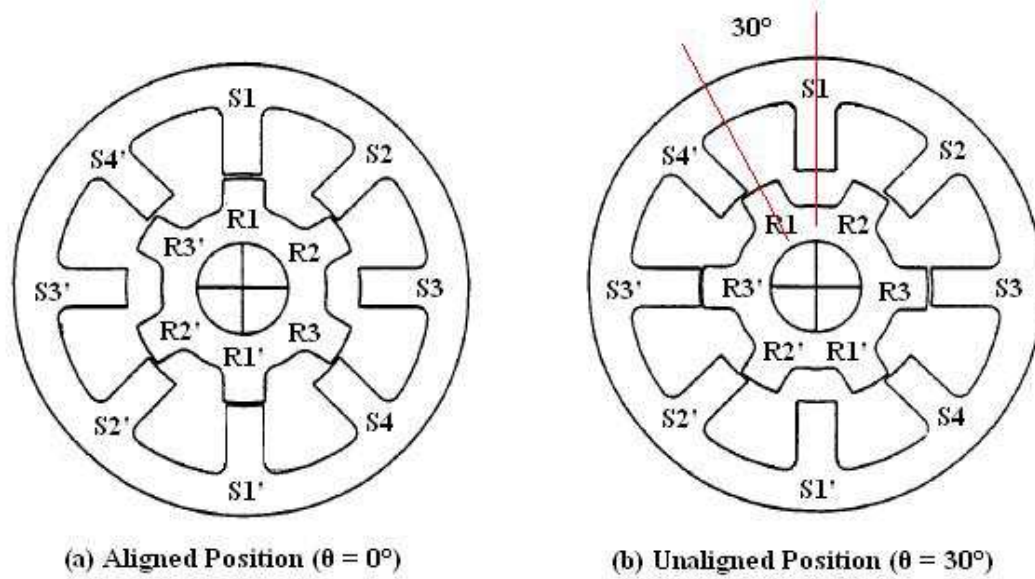
Figure 2.11 SRM internal structure of and 8/6 design [14]

To produce torque the reluctance of the air gap between the rotor and salient stator must vary with rotor position. This inherently produces a high torque ripple, affecting the machine's operation at lower speeds. At high speeds the high frequency of torque ripple has little effect on the speed due to the rotor inertia [14]. To acquire low torque ripple performance many non-linear control strategies and phase interconnections have been reported in literature [14 - 16] but all rely on motor specific characteristics.

The dynamic equations for flux and torque of a SRM are shown below [14].

$$\lambda(\theta, i) = \int (V(t) - i(t) * R)dt \tag{2.1}$$

$$T(\theta, i) = \frac{\partial}{\partial \theta} \int_0^i \lambda(\theta, i)di \tag{2.2}$$

where:

- λ is the flux linkage in Wb-turns from the stator to the rotor and depends on the rotor position (θ) and the stator phase current (i).
- V is the time varying voltage in volts applied to a phase winding.
- R is the constant phase resistance in ohms.
- i is the time varying current in amps flowing in the energized stator phase.
- T is the generated shaft output torque in N-m, dependent on position (θ) and current (i).

The non-linear relationship between the state variables (λ, T) and the input variables (V, R, i) is obtained experimentally. The data shown in Figure 2.12 are based on a 6/4 SRM and illustrates the extent of the non-linearities for that particular machine [16]. The flux points in Figure 2.12 (a) represent equation (2.1) and the torque points in Figure 2.12 (b) represent equation (2.2). Based on the data in Figure 2.12 (b), control of the shaft output torque can be done at a particular point in time, without a torque transducer, provided that the i and θ are known at that point in time.

Data of Flux vs Theta vs Current

(a)

Data of Current vs Theta vs Torque

(b)
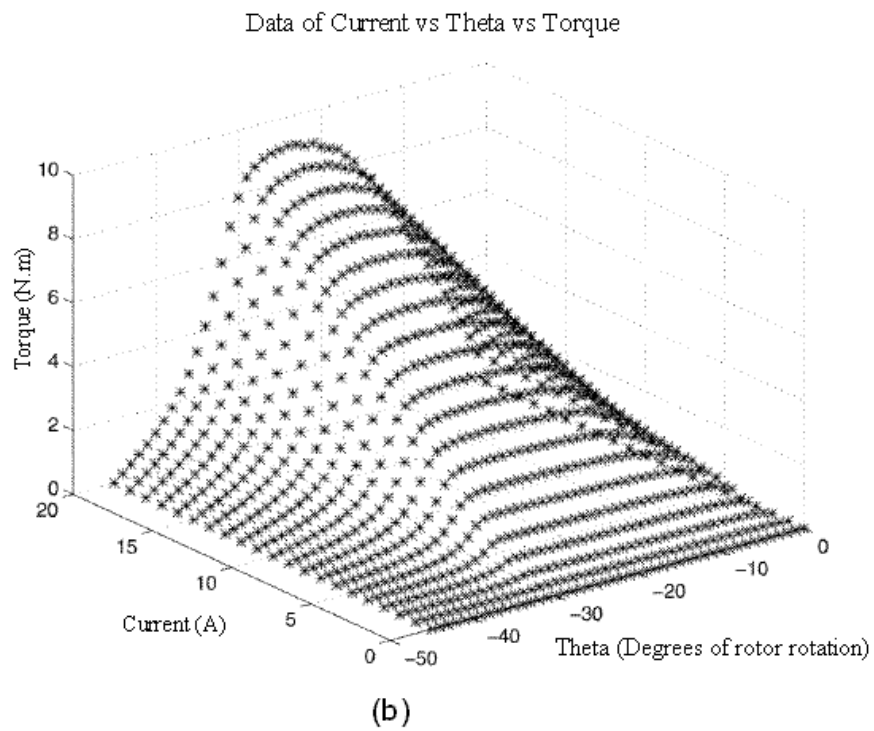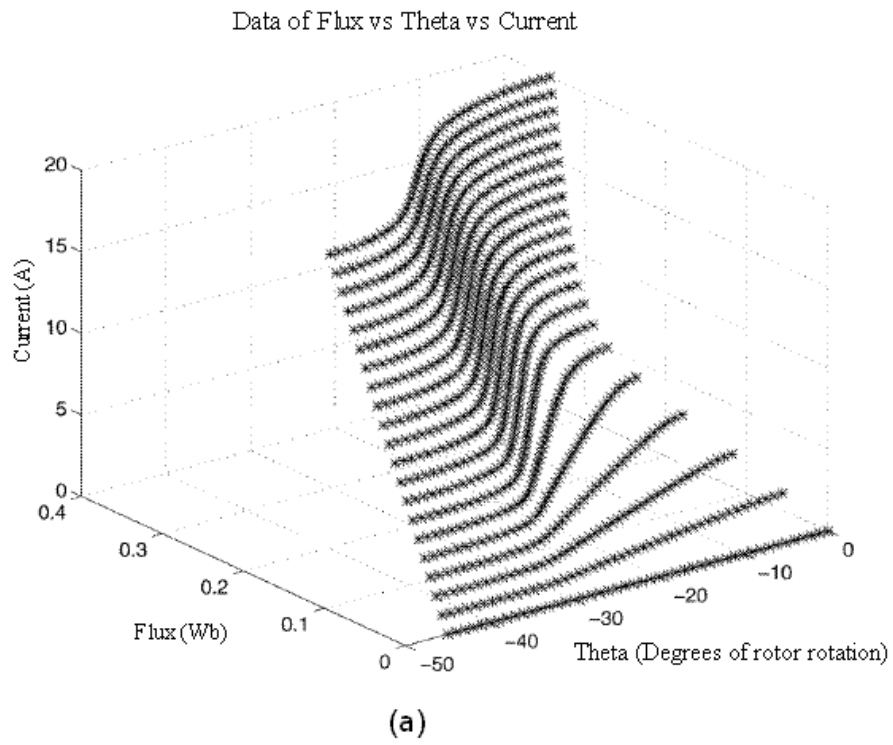
Figure 2.12 Nonlinear SRM model [14]

Torque ripple reduction in a SRM has two primary approaches.

1) Improve the magnetic design in the air gap by changing the stator and rotor pole geometry, but this will reduce the motor performance.

2) Multiphase operation is implemented as opposed to the generic single phase systems, with the aim of averaging out the torque ripple.

3) Sophisticated electronic algorithms can be used to implement torque control. This will improve performance and reduce operation noise.

The theme of this thesis is control, so the various electronic control strategies and phase connections are documented. The magnetic design of the SRM is beyond the scope of this thesis.

Multi phase operation of an SRM

In conventional SRM commutation, only one phase winding conducts at any point in time. In Figure 2.13 (a), the current to the leading phase A would just have switched to the working phase B. For the next 15° of rotation, as the rotor and stator poles align for phase B and the air gap between these poles is reduced, the flux will increase in magnitude, thus increasing the torque (demonstrated in Figure 2.12). When alignment is complete, the current will be switched to the trailing phase, ensuring correct commutation.

The disadvantage in driving or energizing only one phase at a time is that as the current is switched from the leading phase to the working phase, the flux linkage goes from a maximum magnitude to a minimum magnitude, which is extended to the torque. This is the fundamental cause for torque ripple in a SRM.
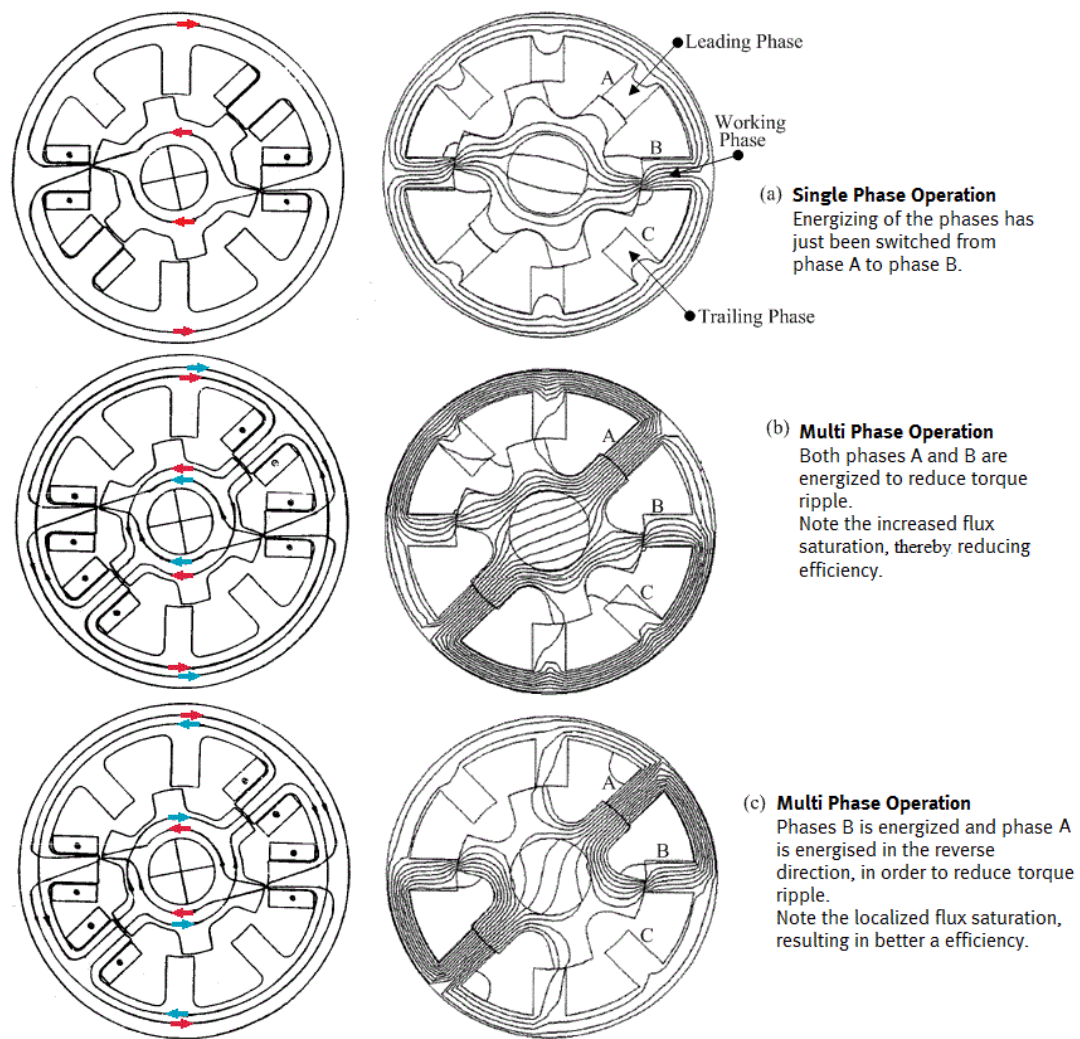
Figure 2.13 Finite element analysis of a 8/6 SRM rotating anti-clockwise [9]

Multiphase operation reduces the torque ripple by energizing two phases for a limited duration over the commutation angle. The total torque produced by the SRM is the sum of the torques produced by the individual phases. All the individual phase torque potential contributions are shown as curve A in Figure 2.14. With single phase operation, only one phase produces torque at any point during the motor rotation and the resultant torque for the motor is shown as curve B in Figure 2.14, and has a torque dip at the switching points. To overcome the torque dips in single phase operation, multiphase operation is implemented and the total torque is the sum of the energized phase torques. In Figure 2.14 curve C, for a 15° overlap is used to illustrate how effective multiphase operation can be at reducing the torque dips. However, this large overlap produces position torque spikes at the switching points.

During multiphase operation, additional flux is generated in the SRM as shown in Figure 2.13(b), and illustrates the increased saturation effects which will cause additional losses.

An alternative excitation strategy for the multiphase operation is shown in Figure 2.13(c); by reversing the excitation of phase A, the resultant flux is only between the poles of phases A and B, thus reducing the overall level of saturation and thus core losses when compared to Figure 2.13(b). The disadvantage of this excitation strategy is the need to have opposite polarity excitation of phase C, thus increasing hardware complexity.
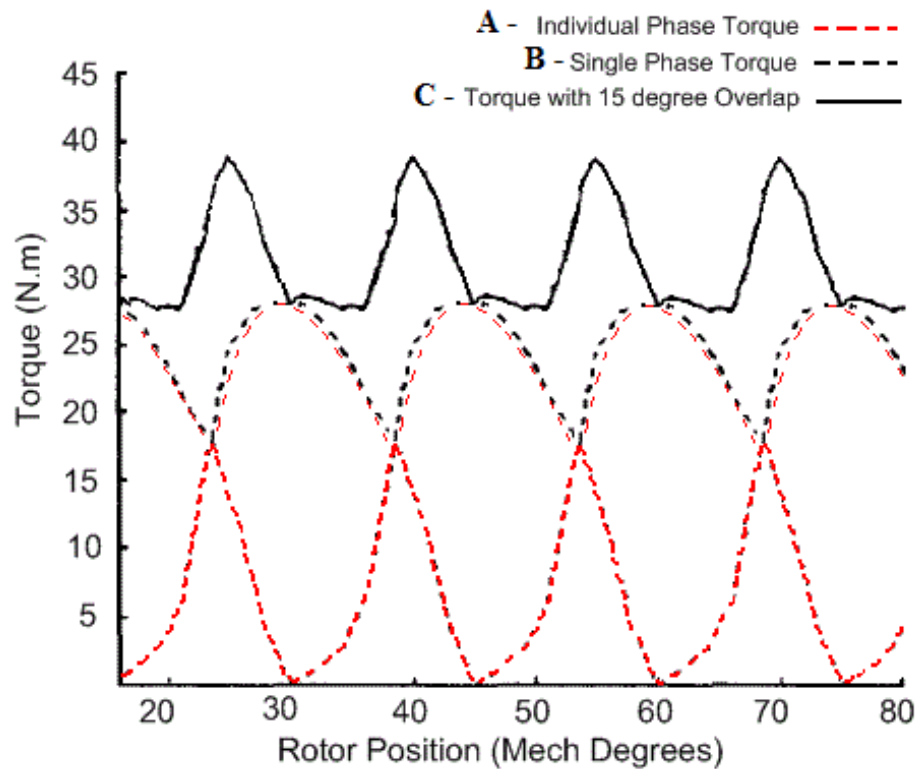
Figure 2.14 Torque comparison of single phase and 15° overlap multiphase operation [9]

Torque – angle – current control characteristics

This method of torque control is the most commonly implemented method for a SRM [14]. Experimental tests have to be performed to acquire the relationship between the motor shaft output torque, rotor position and phase current (either single or multiple phase operation) as shown in Figure 2.12 (b). The control is then implemented in a look-up table form, determining the optimal current required, based on the motor position and the torque input reference. This current is then fed as a reference into a current controller which is purposely designed. In more complex systems each phase will have a dedicated, custom designed current controller, whilst simpler solutions will have a single controller on the DC supply.

Flux– angle – current control characteristics

For this control method, experimental tests have to be performed [14] to acquire the relationship between the motor flux linkage, rotor position and phase current as appears Figure 2.12 (a) (either single or multiphase operation). The flux linkage data is then used to estimate the instantaneous value of the shaft output torque. This graphical data is obtained using a bi-cubic spline interpolation of the voltage and current data acquired experimentally at different rotor positions. The control algorithm then uses a third order polynomial (the coefficients are calculated and saved in the controller) to evaluate the instantaneous torque which is compared to a reference torque, with the error being fed into a current controller. This controller is thereafter implemented in the same way as for the torque-angle-current controller discussed above.

Control angle skewing control

The simplest method of crude torque control is achieved by varying the control angle and does not require any phase current control [12]. The control angle is defined as the rotational position when voltage is applied to the relevant phase winding, compared to the position when this voltage is removed. These two position angles can be advanced or retarded to increase or decrease the output torque. Whilst this method of torque control is simple, to acquire smooth torque control complex optimization algorithms are needed (such as neural networks and/or fuzzy logic). This type of control can be taken a step further. All current controllers have inherent limitations with fixed conduction angles. Consider a PWM controller maintaining constant phase current. The duty cycle will increase to counteract the back EMF as the motor speed increases. However, once the mark to space ratio equals one, and the motor is at maximum speed, no further control is possible by the

controller. This occurs at the motor's base speed and is defined as the highest speed the motor can reach, whilst maximum voltage and current are applied with fixed firing angles. Constant torque is not achievable at base speed due to the controller's inability to act on the current. However, with skewing of the control angles, a constant power region is achieved, analogous to field control in the brushed DC motor [15].

Torque sharing function control

This type of control [12] is a hybrid of the multi phase operation of a SRM and either torque-angle-current control or flux-angle-current control. The principle is that the total instantaneous torque (T_{total}) generated in the SRM is the sum of the individual instantaneous phase torques. This allows a lookup table reference to be used in conjunction with hysteresis current control.

$$T_{total} = T_{ref} * f_t(\theta)$$

(2.3)

where

$$f_t(\theta) \ = \ \sum_{i=1}^{n} f_i(\theta)$$

(2.4)

f_i is the per phase torque sharing function. f_i is based on the individual phase torque as shown in Figure 2.14 and is a function of rotor position.

The torque control algorithm then follows the strategy of:

    a) Obtain the torque reference (from a speed controller or user input).
    b) Measure the rotor position.
    c) From the torque sharing function, obtain a per phase torque reference.
    d) Obtain a current reference for each phase based on the lookup table strategy.
    e) Perform current control on each phase.

A suitable motor for an EV goes hand in hand with an appropriate power electronics drive for the motor. The next sub-section therefore considers the power electronics needed by the respective motors.

2.3.2   Motor drives

When using either an AC or DC motor for electric vehicle applications, control is implemented through both software and hardware (torque, speed and regenerative control). The hardware portion for the control is referred to as the "drive" and comprises of power electronics of which the output depends on the input control signals. This section considers the primary drive configurations and semiconductors implemented in drives. The design of a high performance drive must typically meet the following specifications [18]:

a) The speed response must be smooth without cogging effects or torque pulsations at low speeds even down to standstill.

b) Speed reversal and transition between motoring and regenerative modes must be smooth under dynamic loading conditions.

c) The drive system must be capable of constant rated torque up to rated (or base) speed and constant power operation when using field-weakening techniques to obtain speeds above base speed.

2.3.2.1   Solid state semiconductor switches

A solid state semiconductor is comprised of doped p-type and n-type layers. Different configurations for a single family are possible and result in either a p-type or n-type depletion regions within, thereby determining what type of control signal is needed to enable them. For this section, typical n-type semiconductors are depicted (where relevant).

The Thyristor

A thyristor (Figure 2.15) is a constructed from four layers of doped semiconductors. It is a current controlled device that will only conduct for a positive potential across the anode and cathode, once a gate signal has been applied. If the gate signal is then removed, the device will continue to conduct as long it is forward biased (the anode-cathode voltage is not reversed). This type of switching is ideal for current fed, AC applications where the source will turn the device off (natural commutation) during a negative half cycle.
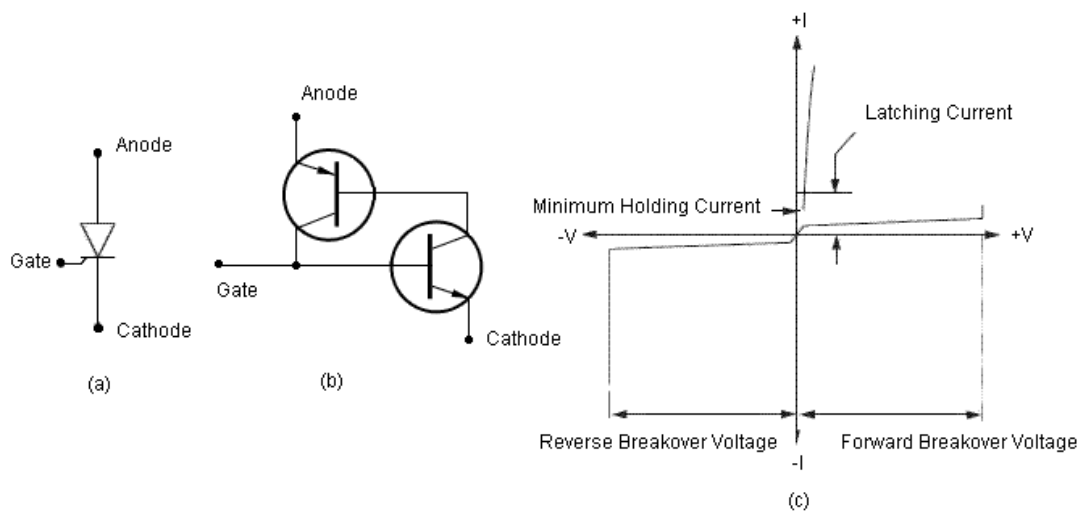
Figure 2.15 Thyristor (a)-circuit symbol (b)-equivalent circuit (c)-current characteristics [18]

The metal-oxide-semiconductor field-effect transistor (MOSFET)

This device is voltage controlled and will only conduct when the gate-source voltage (V_{gs}) is applied, allowing DC applications. The temperature coefficient is negative, eliminating possible thermal run-away damage and the typical on-resistance is less than that of an IGBT, thus improving efficiency.
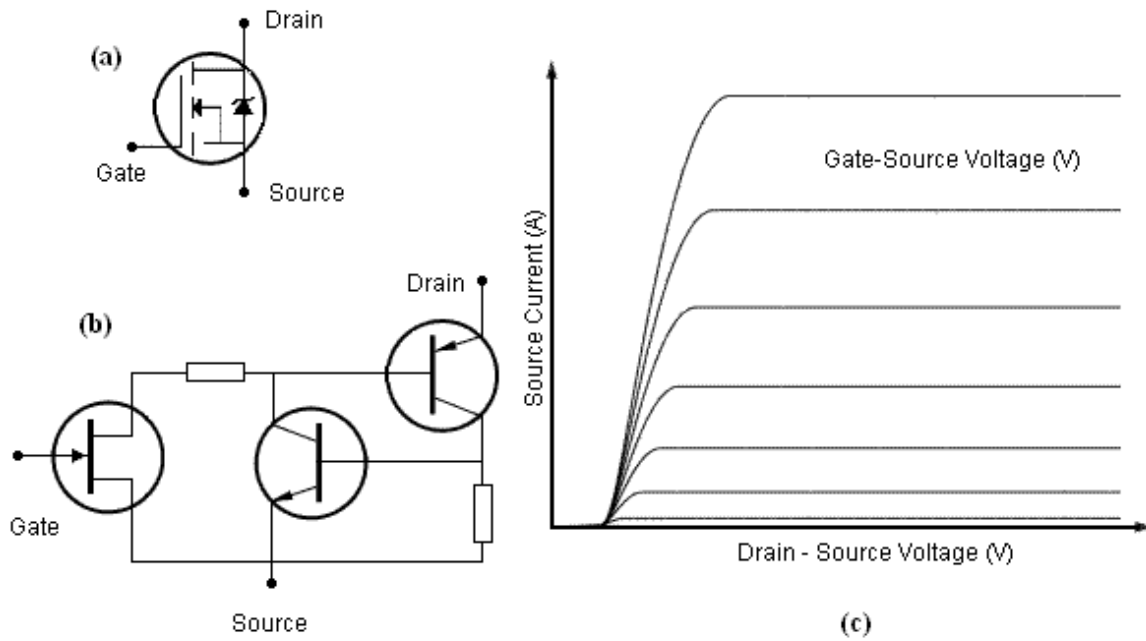
Figure 2.16 MOSFET (a)-circuit symbol (b)-equivalent circuit (c)-voltage characteristics [18]

The insulated-gate bipolar transistor (IGBT)

This device has four layers of doped semiconductors as with a thyristor. In addition, an IGBT has a field effect transistor (FET) on the gate, making it a voltage-controlled device which allows control of both turn-on and turn-off of the conduction. With this principle an IGBT can be used for DC (or AC) and high current applications. However, IGBTs have negative thermal characteristics, which can lead to thermal runaway. The structure of an IGBT is based on that of a MOSFET and the characteristics are similar. The physical difference being an IGBT and MOSFET is a p-type silicon base layer of the collector present in an IGBT [18]. The advantage for an IGBT, due to this layer, is a higher current capability to size ratio, with the disadvantage of a higher on-state resistance.
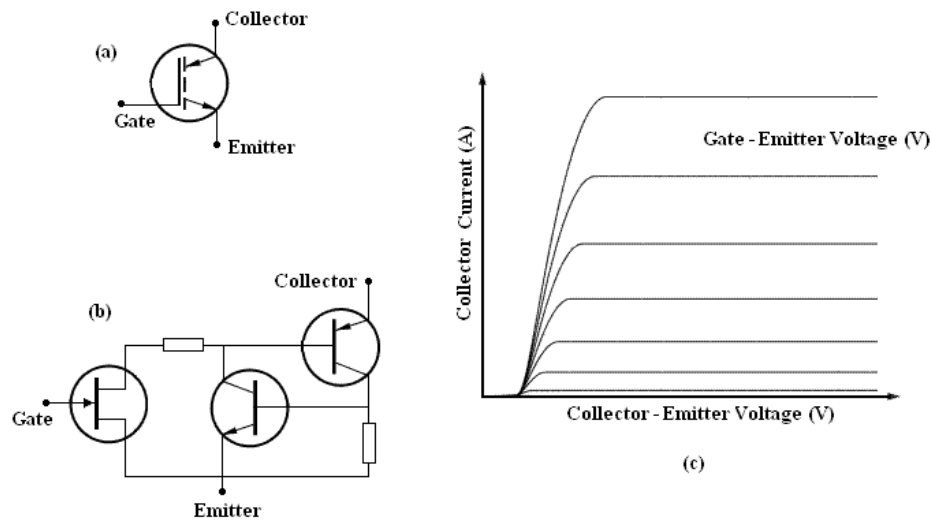
Figure 2.17 IGBT (a)-circuit symbol (b)-equivalent circuit (c)-voltage characteristics [18, 19]

The operating conditions for thyristor, MOSFET and IGBT are depicted in Figure 2.18, with the highest current capability module being that of the thyristor. Although the MOSFET is the most efficient (due to a lower on-state resistance) it has the lowest current capability [18].
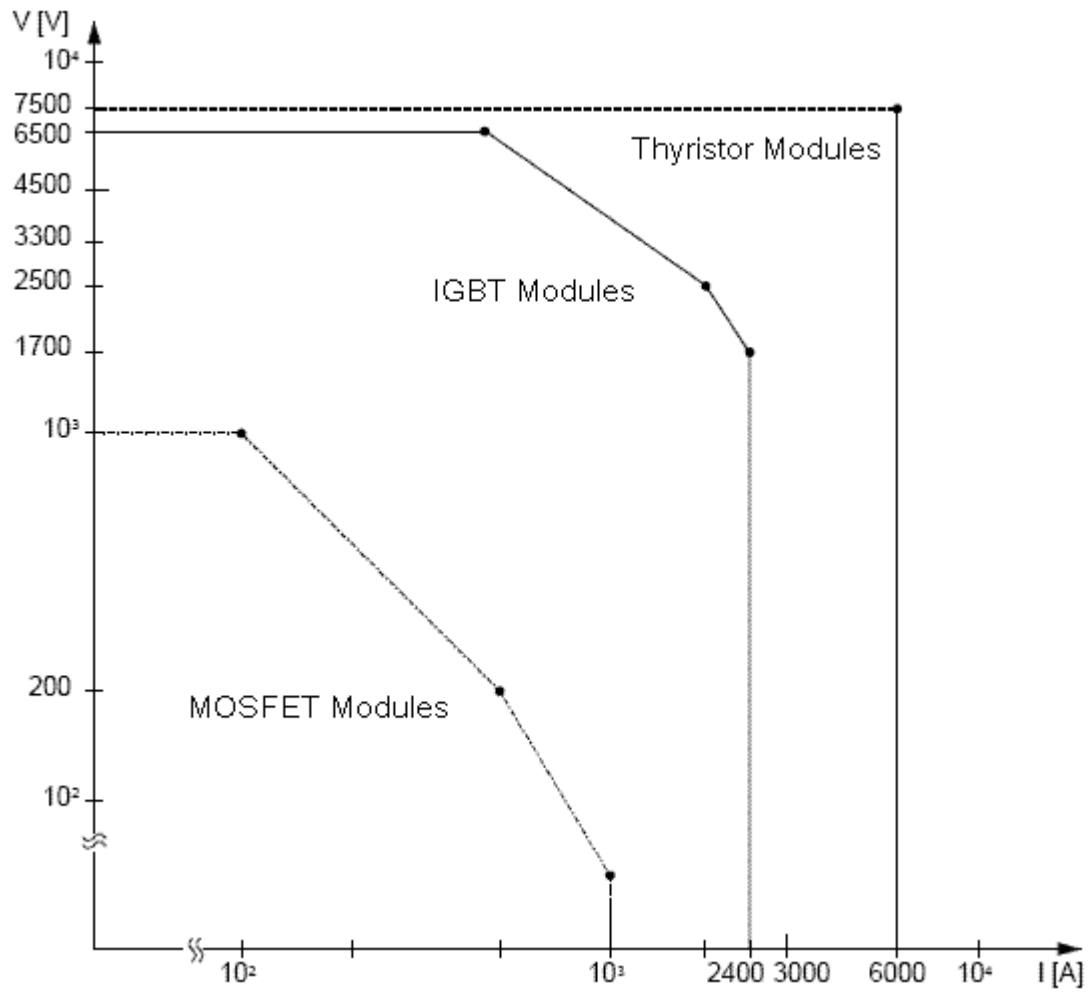
Figure 2.18 Application regions for power semiconductor modules [18]

2.3.2.2 DC drive topology

Traditional drive systems as documented in [20] are based on the principle of rectifying an AC supply and controlling the firing angle of a solid state semiconductor switch. This principle however does not satisfy all the necessary drive specifications stipulated above. With the development of faster switches and improved current and torque transducers, superior control has been achieved in recent years [18].

The most commonly implemented system for DC motor control is described in section 2.3.1.1. The field current is regulated to control the field flux, and current control in the armature allows for accurate torque control. The topology for the armature drive is typically an H-Bridge configuration, allowing bidirectional motor and regeneration operation (four quadrant operation) as shown in Figure 2.19. High frequency PWM signals from a controller implement the current control through the armature. When switches (depicted as MOSFETS, but can be IGBTs) Q1 and Q4 are on, the motor will be driven in one direction. The direction is reversed if switches Q2 and Q3 are enabled. Care needs to be taken not to switch Q1 and Q2 on at the same time or Q3 and Q4 on at the same time, as there is no load to limit the current, resulting in short-circuiting the supply. MOSFETs have inherent fly-back diodes for regenerative operation. However due to the diodes' current limitations, it is common practice to have higher rated schotky diodes in parallel with each semiconductor.
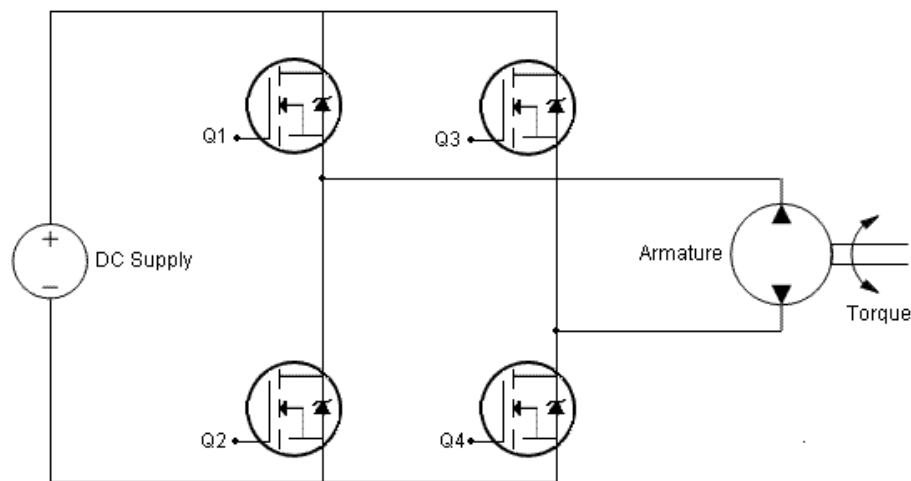
Figure 2.19 H-bridge [20]

2.3.2.3   AC drive topology

In most EV applications the AC motors (such as the IM and BLDC) have three phases, but for a SRM the number of phases may increase. Figure 2.20 shows a three phase DC supplied AC drive with an inverter connected to a motor. The semiconductors in the inverter can be either MOSFETS or IGBTs driven in PWM mode. Thyristors can also be used but require a forced commutated auxiliary circuit and are not used in PWM mode but rather produce a stepped output voltage wave. At low to medium power ratings, such as required in typical EVs, MOSFETs and IGBTs are preferred.
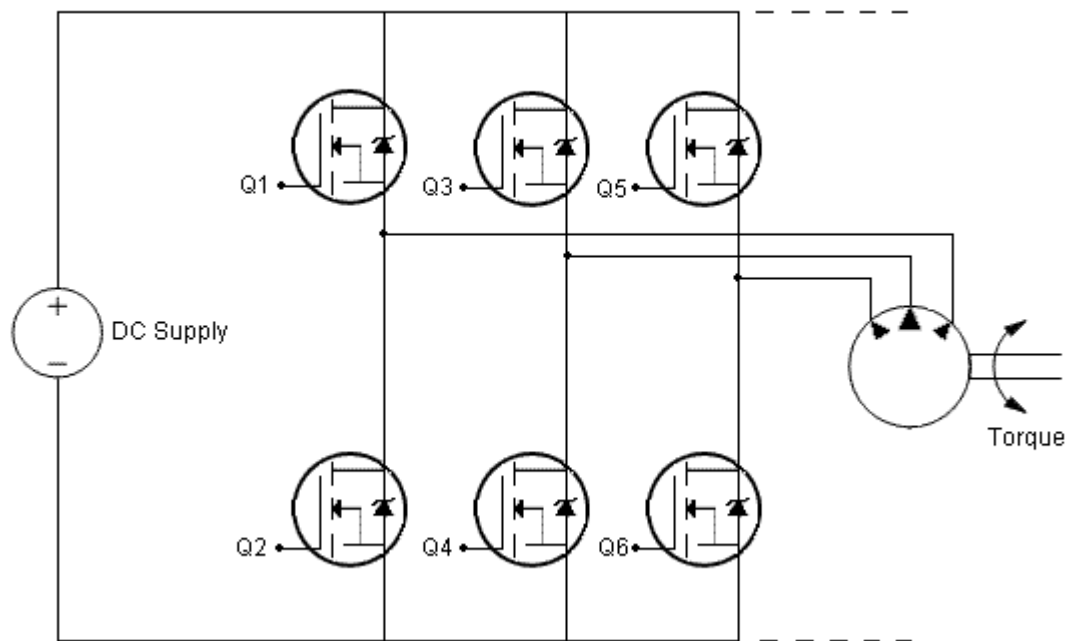
Figure 2.20 DC supplied AC drive via an inverter [20]

For drives with current ratings beyond that of IGBTs, gate-turn-off (GTO) thyristors (with a slower response than IGBTs) can be used, to remove the need for a force commutation auxiliary circuit that thyristor would need.

It must be noted that the drive topologies considered above will not work for a SRM as it requires each stator phase to be in series with the semiconductors switches as shown in Figure 2.21 [19].
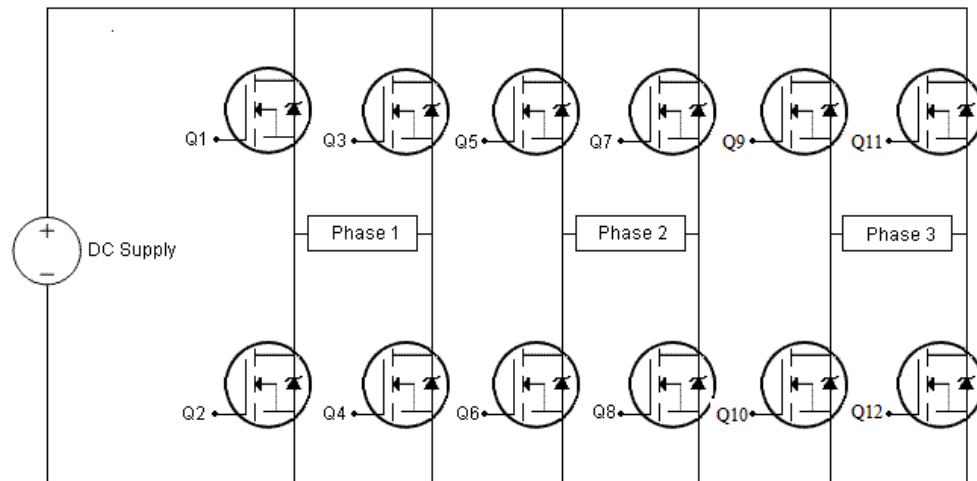
Figure 2.21 Drive for a 6/4 SRM [14]

2.3.3   Energy sources

The primary drawback to an EV is the operational distance, which is limited by the energy source. In 1992 the United States Advanced Battery Consortium (USABC) was established. The USABC is a cooperative endeavor between the U.S. Department of Energy and the automakers Chrysler Group, Ford Motor Co. and General Motors Co. The USABC aims to develop advanced electrochemical energy storage technologies which will allow the commercialization of fuel cell (FC), hybrid and electric vehicles which can perform as well as an ICEV [1]. The development criteria include:

a)   High specific energy (kWh/kg) and high energy density (kWh/L).

b)   High specific power (kW/kg) and high power density (kW/L).

c)   Fast charging and deep discharging capabilities.

d)   Long cycle and service lives.

e)   Low self-discharging rate and high-charging efficiency.

f)   Safe and cost effective.

g)   Maintenance free.

h)   Environmentally sound and recyclable.

Often more than one type of energy source is used when designing a vehicle. In this hybridization of energy sources, a better solution can be achieved eliminating the compromise between specific energy and specific power. An example of this is seen in the hydrogen electric vehicle (HEV) [1] where the hydrogen has a high specific energy for a long driving range and the battery has high specific power for acceleration. Other examples include battery and battery-hybrid (one battery will have high specific energy while the other battery will have high specific power); battery and ultra-capacitor hybrid; battery and high speed fly-wheel and battery and fuel cell hybrid.

2.3.3.1   Batteries

The most popular energy source for an EV is the battery, in which stored chemicals react, creating the electro motive force (EMF) to drive the motors. The reaction is thermally-dependent, thus during high current transients the internal resistance increases. The best batteries available at present are valve-regulated lead-acid (VRLA), nickel cadmium (Ni-Cd), nickel zinc (Ni-Zn), nickel-metal hydride (NiMH), zinc-air (Zn-Air), aluminium-air (Al-Air), sodium/sulphur (Na/S), sodium/nickel chloride (Na/NiCl$_2$), lithium-polymer (Li-Polymer) and lithium ion (Li-Ion) type batteries. The specific energy, energy density, specific power and power density are compared to the USABC development criteria in Table 2.1 [1]. It is important to note that the values given are guidelines as the specifics of a battery will change between manufacturers and even variations from one manufacturer as different models are produced to allow for the tradeoff between specific energy, specific power and life cycle.

Table 2.1 EV battery specifications [1]

	Specific Energy (Wh/kg)	Energy Density (Wh/L)	Specific Power (W/kg)	Cycle Life (cycles)	Estimated Cost (USD/kWh)
VRLA	30 - 45	60 – 90	200 – 300	400 – 600	150
Ni-Cd	40 – 60	80 – 110	150 – 350	600 – 1200	300
Ni-Zn	60 – 65	120 - 130	150 – 300	300	100 – 300
NiMH	60 – 70	130 – 170	150 – 300	600 – 1200	200 – 350
Zn-Air	230	270	105	NA*	90 -120
Al-Air	190 – 250	190 – 200	7 – 16	NA*	NA**
Na/S	100	150	200	800	250 – 450
Na/NiCl$_2$	86	150	150	1000	230 – 350
Li-Polymer	155	220	315	600	NA**
Li-Ion	90 – 130	140 – 200	250 – 450	800 – 1200	>200
USABC	200	300	400	1000	<100

NA* - Mechanically recharged by replacing metal plates

NA** - Not Available

Despite the initial high cost of a Li-Ion battery, its performance in the remaining criteria makes it the favorable choice for EV applications. The price should decrease as the demand increases and when mass production is implemented. Zn-Air batteries are also favored due to their higher specific energy, density and low cost. The disadvantage for Zn-Air batteries is that regeneration is not possible into the cells so a second battery type would be required and the two batteries would operate in a battery-hybrid configuration.

2.3.3.2   Fuel cells

The fuel cell (FC) works on an electrochemical principle similar to the battery. The chemicals are not stored as in a battery, but rather supplied to the system, allowing a stable energy source as long as fuel is available. The system is efficient, quiet, quick to refuel and has a low emission depending

on the chemicals chosen. To further understand the operation of a fuel cell, consider a hydrogen fuel cell.

There are three sections to the unit as shown in Figure 2.22. The anode (A) or fuel electrode is where the hydrogen oxidization occurs and drives free electrons into the external circuitry. The cathode (C) is where the oxygen reduction reaction occurs and receives the electrons from the circuitry. The electrolyte (E) allows a path for the hydrogen ions on the anode to pass to the cathode, whilst being an electron insulator [1].
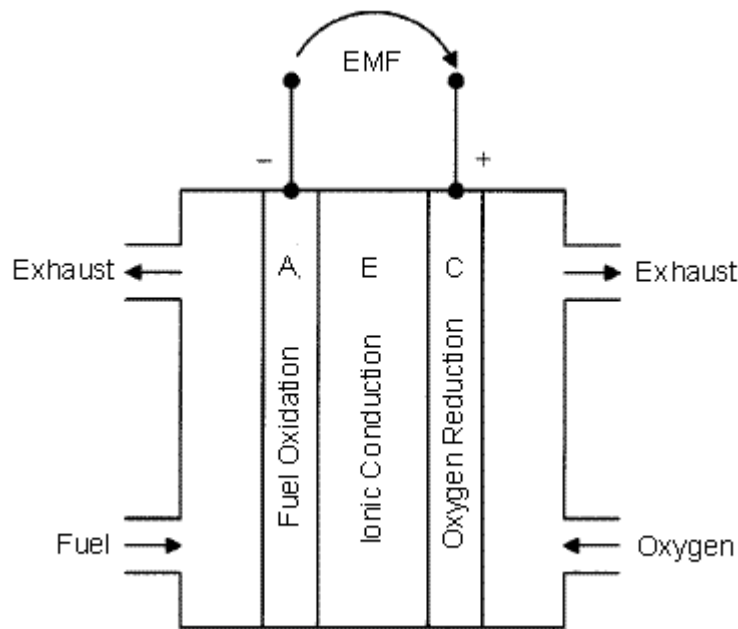
Figure 2.22 Hydrogen fuel cell [1]

Oxygen is readily available from the atmosphere, but hydrogen needs to be refined from fuels such as hydrocarbons, methanol or coal. There are three ways of storing the hydrogen for a FC [1].

a)   It can be compressed and stored at a pressure of 350 bar.

b)   When hydrogen is chilled to below its boiling point of -253°C, it can be stored as a liquid.

c)   Hydrogen can be stored as a compound such as a metal hydride. The reaction can then be reversed at temperatures ranging from 200°C upwards depending on the metal used. Fuel cells being used are phosphoric acid fuel cells (PAFC), alkaline fuel cells (AFC), molten carbonate fuel cells (MCFC), solid oxide fuel cells (SOFC), solid polymer fuel cells (SPFC), and direct methanol fuel cells (DMFC). A comparison between these metal hydrides is shown in Table 2.2 below [1].

Table 2.2 Metal hydride properties [1]

	Working Temp (°C)	Power Density (W/cm^2)	Projected Life (kh)	Estimated Cost (USD/kW)
PAFC	150 - 210	0.2 – 0.25	40	1000
AFC	60 - 100	0.2 – 0.3	10	200
MCFC	600 – 700	0.1 – 0.2	40	1000
SOFC	900 - 1000	0.24 – 0.3	40	1500
SPFC	50 – 100	0.35 – 0.6	40	200
DMFC	50 - 100	0.04 – 0.23	10	200

The presently preferred, commercially available fuel cell is in the form of pure hydrogen pressurized to 350 bar. Service systems (analogous to gas stations) currently installed, can only supply enough hydrogen for a few cars a day. The restriction is not from a lack of hydrogen, but the time the compressor takes to reach filling pressure. Though the storage is at 350bar, filling needs to be at 700bar. For prototype EV implementation a fuel cell is used in conjunction with a battery. The fuel cell provides the average power required by the EV's motors, and the battery is sized to provide power-demand surges during acceleration, and receive momentary power during regenerative braking [21].

2.3.3.3   Ultracapacitors

During urban commuting the number of acceleration and deceleration transients are high. This places a demand on the batteries to provide or receive peak power at regular time intervals, though the average power requirement of the EV is significantly less than these peaks. To accommodate this, the batteries are often over-designed and there is a reduction of their cycle life as current surges generate heat in the battery, increasing the internal resistance. Driving an EV from an energy source which can supply such peak energy demands, without reducing the cycle life of the batteries is more appropriate. The energy source can then be recharged during times of low energy requirement or regeneration. This auxiliary energy source has been widely investigated and is called an 'ultracapacitor" or 'supercapacitor' [21]. This type of capacitor has a low specific energy and subsequently cannot be used on its own, but it has very high discharge and recharge rates that

provide fast and efficient regeneration and acceleration. The series resistance of this capacitor is lower and shunt resistance is higher when compared to a conventional capacitor, which increases the self-discharge time constant.

There is no single energy source which is ideal to supply an EV. A combination of a battery and ultracapacitor is used to gain the advantages of both sources and eliminating the disadvantages of each source, creating an ideal energy source known as a "battery and ultracapacitor hybrid energy system". This system increases the life cycle of the sources and the range of an EV. For example a 32% range increase compared to running on batteries alone has been reported (for the same energy consumption) [22]. While an ultracapacitor connected across the battery terminals will reduce the transient currents, the best method is to use an energy management controller. The controller ensures that at low speeds the ultracapacitor is fully charged for possible upcoming acceleration and at high speeds the ultracapacitor is sufficiently discharged in preparation for regenerative braking. A DC/DC converter is used in boost mode during discharge, and then in buck mode when charging from the battery or braking. To better ensure that current is sourced from the batteries during steady-state EV travel, and that for short duration transients current is fed from the ultracapacitor, the EV control algorithm is based on the frequency of speed deviation. By implementing an ultracapacitor for short range EV applications, the size of the required battery is reduced, and thus the weight and cost of the EV. This implementation should be done based on a vehicle requirement survey because if the EV is used on highways, with fewer acceleration and deceleration transients, the implementation of the ultracapacitor is rendered pointless and the smaller battery size will reduce the performance of the EV.

If EVs are to be the future of transportation, the following commercial support infrastructures need to be considered.

a) Availability of charging stations.

b) Standardization of EV batteries for charging.

c) Regulation of clean and safe charging.

d) Impact on the power utilities.

The primary concern regarding EVs is the charging facility availability, as a support structure (gas stations) is already in place for ICEVs.

When charging EV batteries, three schemes can be used:

a) Fast Charge: This scheme will rapidly recharge the EV's batteries by applying a high current to the batteries. It is used when the shortest duration stop is possible but will reduce cycle life of the batteries.

b) Normal Charge: This scheme is used under general conditions to allow the batteries to be charged fully and not at the maximum current ratings, allowing optimal cycle life of the batteries.

c) Trickle Charge: If batteries are left for long periods of time, they lose their charge and a so-called dead cell can occur. Trickle charging is used during such long periods, with a small amount of current supplied so as to keep the battery fully charged without overcharging it.

For the domestic environment normal and trickle charging schemes are implemented, whilst public charging facilities can cater for all three charging schemes. The energy demand from the power utility can be scheduled to off-peak times (charging over night) and this can potentially reduce the cost to the customer. Charging does inject current harmonics into the grid, especially during fast-charging but there are methods to reduce the effect by using either passive or active filters, but they add cost. Each vehicle being charged at a station will create harmonics, however as the number of charging vehicles and types of chargers increases, the average or total harmonic distortion (THD) will probably be less than expected as some of them will cancel from one charger to another [22].

2.3.4   Steering solutions

When an EV is running along a straight line, the velocity of the two driven wheels is required to be the same. However when the vehicle changes direction or turns a corner, the outer drive wheel requires a speed increase and the inner drive wheel requires a speed decrease. Figure 2.2 illustrates two fundamental methods of achieving this difference in speed. For Figure 2.2 (a-c) this speed differential is accomplished mechanically whilst in Figure 2.2 (d-f) an electrical implementation is required.

2.3.4.1   Mechanical steering solutions

Figure 2.2 (a-c) accomplishes a speed differential between the two driven wheels with the use of a differential gearbox. A coupling from the steering wheel is used to mechanically determine the offset between the transmission shaft from the motor and the left and right driving wheels [1, 23].

2.3.4.2   Electrical steering solutions

The advantage for Figure 2.2 (d-f) is the elimination of the mechanical losses by removing the differential gearbox. The disadvantage lies in the need for increased complexity in the drive algorithms to create the differential speed. If the correct speed difference is not acquired for the turning radius commanded, the vehicle traction needs to be broken as in a "skid steer" vehicle. This concept is widely used in construction vehicles such as bob cats, which operate at reduced speeds. The catastrophic effects of loosing traction whilst cornering at high speeds, is self explanatory.

An electrical alternative to complex algorithms is possible. As the driver mechanically adjusts the direction of the drive wheels by means of a steering wheel, the difference in speed produces a difference in back EMF (BEMF) between the two motors, and this inherent property is exploited by wiring the drive circuitry in series as appears in Figure 2.23 to realize constant torque throughout the turn [23].
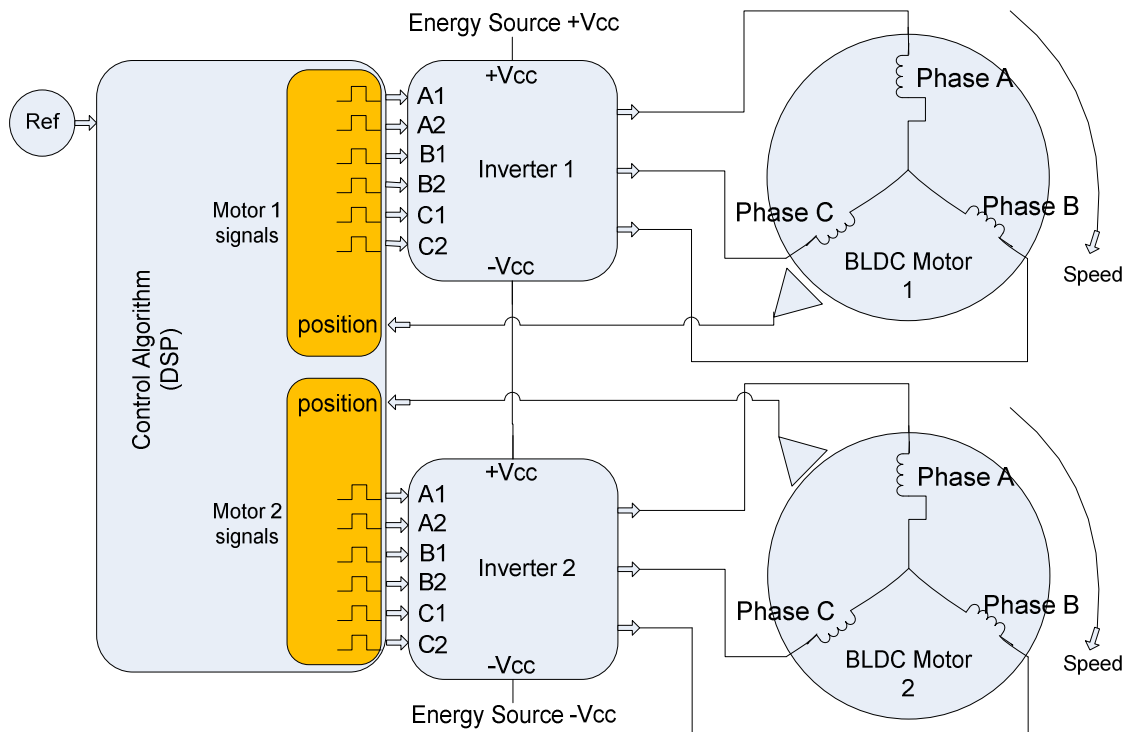
Figure 2.23 Drive and control system to achieve differential speed

The assumption made for Figure 2.2 is that the user physically adjusts the steering direction as found in a car, with the front drive wheels swiveling to the orientation stipulated. A second solution is to have the drive wheels at a fixed orientation, and the free running wheels swivel, as seen on an

electric wheel chair. For this second solution the user's steering input is electrically implemented by driving the two motors in Figure 2.23 at different speeds to achieve turning and cornering. This eliminates the need for differential algorithms as the driver acts as the feedback loop controlling the motors, and the swiveling wheels adjust speed and orientation automatically.

2.4   **Final selection**

Based on the surveys described above, a selection is now made for wheel chair applications.

a) The drive configuration depicted in Figure 2.2 (f) is chosen as it is the simplest mechanical design and will allow two axis control algorithms.

b) The preferred motor is a SRM as it is most robust, however it is not commercially available in a hub wheel format. A BLDC motor is the next best solution. Two hub type BLDC motors of 500 W each, are selected for the wheel chair application of this project.

c) The power electronics to drive the motors comprises MOSFETS as they have the lowest on-state resistance, improving efficiency and are readily available.

d) The power supply for the vehicle would ideally be lithium ion batteries (section 2.3.3.1) with an ultra capacitor and power management control algorithm (section 2.3.3.3). However as the theme for this thesis is motion control, the additional cost required is not warranted so Lead Acid Batteries are used during the motor bench testing.

e) The steering solution proposed in section 2.3.4, with a differential torque on the two motors resulting in vehicle orientation is used.

f) The control processor is selected based on the application hardware. The functionality required (analog inputs, outputs and PWM outputs etc.) can only be determined once the final selection is made. For this application when considering either microcontrollers or digital signal processors (DSPs), a variety of units can be used. Available at the University of Kwa-Zulu Natal, at the time of this research, is a TMS320F2812 motor control development board. Control algorithms are implemented on this platform and programmed using Visual Solutions software, VisSim.

2.5   **Summary**

This chapter has documented research by others into the field of electric vehicles and control strategies in general. Based on this information and available hardware for this project, a final selection of the technology is made and used as a development platform to achieve the objectives of propelling an electrically powered wheel chair as described in the introduction to this chapter.

More details for the BLDC motor and its controls are discussed in Chapter 3.

Chapter 3   -   BLDC Hub Motor Operation Theory

3.1   Introduction

A brushless DC motor (BLDCM) is a synchronous motor, which uses a direct current voltage source and solid-state switches to create continuous rotational kinetic energy. This kinetic energy is used in a multitude of applications. The concept of a BLDC Motor has been briefly introduced in Chapter 2, along with various AC and DC motors. This chapter documents the operational theory, commutation strategies and regenerative braking for a BLDC motor, with particular focus on a BLDC hub motor (BLDCHM). It has centralized stationary phase windings and an external rotor comprised of rare earth permanent magnets. This configuration is used primarily as an electric wheel for electric vehicle (EV) applications and is also referred to as an inverted DC motor due to the physical architecture.

3.2   Construction of a BLDCHM

A three-phase BLDCHM is comprised of two fundamental portions. The first is the rotating permanent magnets, and the second is the stationary electromagnets. A simplified cross sectional representation of the BLDCHM appears in Figure 3.1 and is used to further examine the construction and operation of the motor [8].
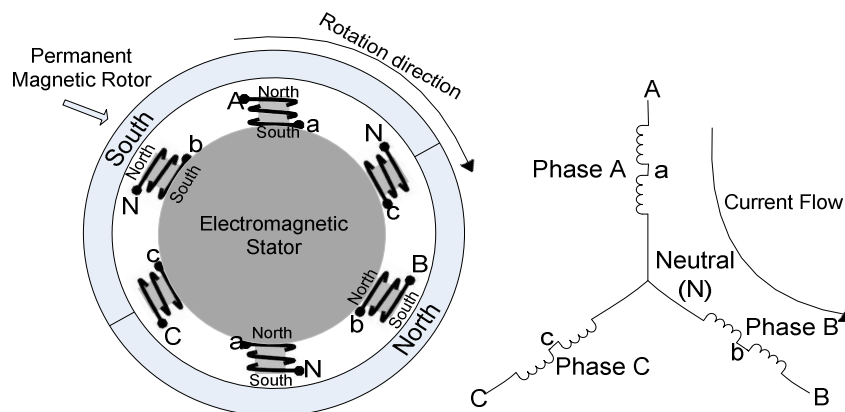
Figure 3.1 Simplified cross sectional view and circuit diagram for a BLDCHM [8]

3.2.1   Stator construction

The stator of a BLDC motor is the stationary electromagnetic portion of the motor. It is formed from stacked steel laminations. These steel laminations are stacked along the motor's rotational center, either on the exterior (if the permanent magnet rotor is used as a shaft drive) or interior (if the permanent magnet rotor is used as a hub motor as appears in Figure 3.2). A series of formed coils are then wound within the lamination slots. When the coils are energized, the laminated steel portion within each coil, directs the flux path, acting as the electromagnet. The BLDC motor phases are star-connected (as appears in Figure 3.1) and are formed from the many coils being wired in a specific arrangement to form an even number of pole pairs.
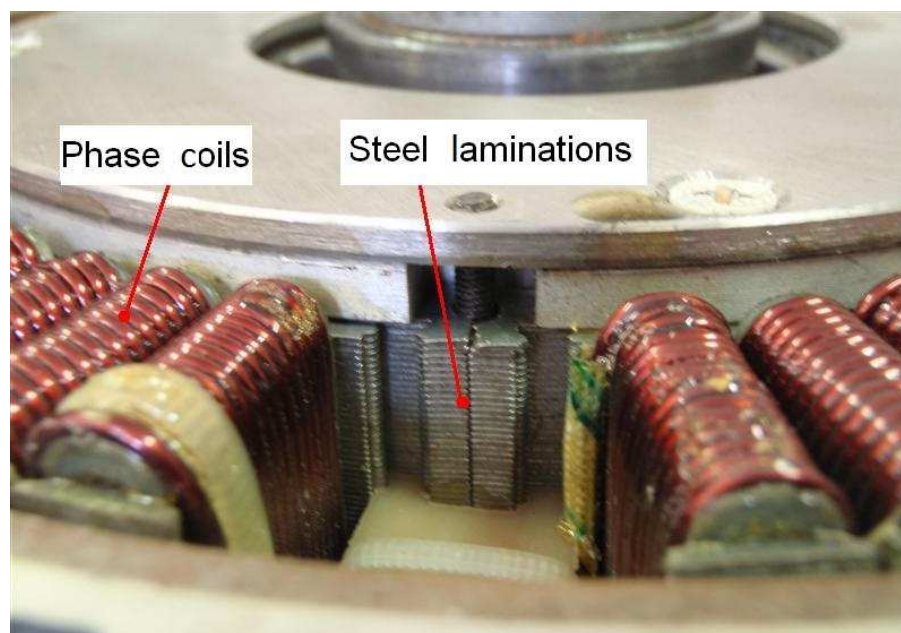
Figure 3.2 BLDCHM electromagnetic stator

Depending on the wiring configuration of the phases, two types of motors can be designed. The first is a trapezoidal motor (also referred to as a brushless dc motor, or BLDC motor) and the second is a sinusoidal motor. These names are derived from their respective back electromotive force (back EMF) waveforms, shown in Figure 3.3 and Figure 3.4 respectively. The sinusoidal PM motor has the advantage of a smoother torque output due to the current change within the motor being continuous. However to achieve this, a more complex interconnection and configuration between the phase coils is required, and for Field Orientated or Vector Control an expensive shaft encoder is needed, thus altogether resulting in a higher cost. This type of motor is also commonly known as a permanent magnet synchronous motor (PMSM) [6, 7].

The trapezoidal back EMF BLDC motor's stator windings have a simpler interconnection, requiring a much cheaper resolver for vector control. Vector control of this motor is the focus of this thesis. The limitation of the BLDC motor is in position control applications and the effects of torque cogging.

For the purpose of this thesis, the term BLDCHM therefore refers to a trapezoidal back EMF motor mounted in the hub of a wheel.
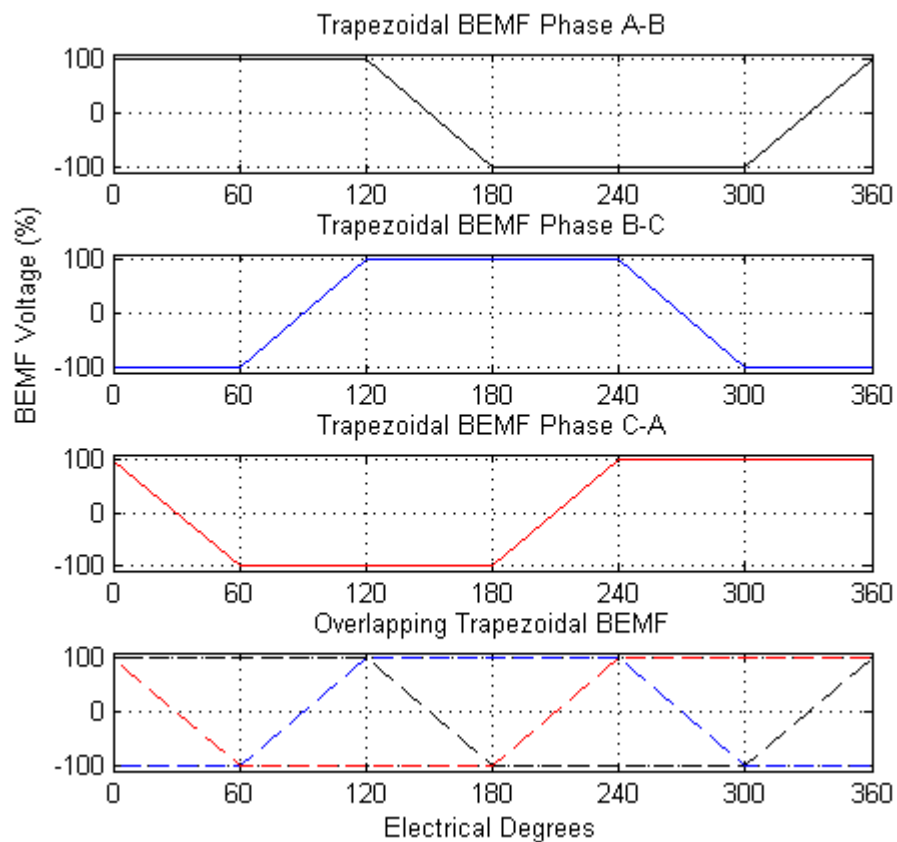
Figure 3.3 Back EMF waves of a trapezoidal BLDCHM [4]
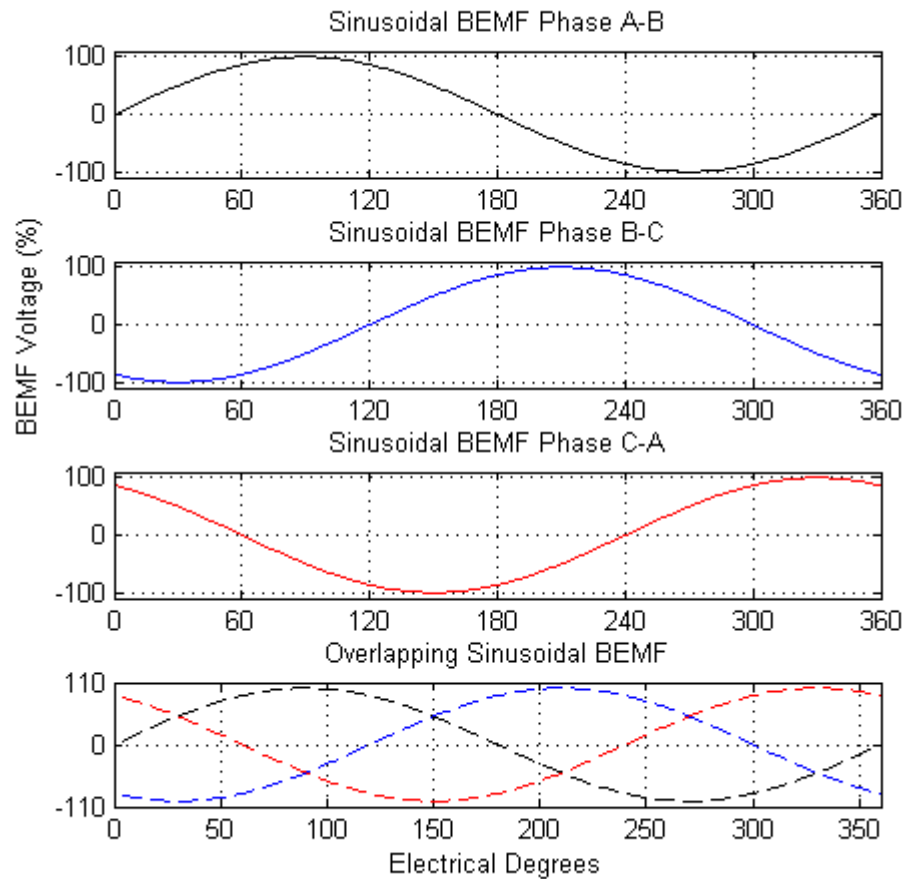
Figure 3.4 Back EMF waves of a sinusoidal PMSM [4]

3.2.2   Rotor construction

The rotor of a BLDC motor comprises an even number of permanent magnetic poles. Traditionally the rotor construction uses ferrite magnets, however as development in the field expands, rare earth alloys as permanent magnets have been more successful in producing a greater flux, allowing the BLDCMs of equal output torque, to be smaller in physical size. Some of the rare earth alloys include neodymium (Nd), samarium cobalt (SmCo) and an alloy of neodymium, iron and boron (NdFeB) [5]. However, China has become the major source of rare earth permanent magnets and has steadily increased the price which has become a concern to some of the motor manufacturers outside of China. The US Department of Energy issued a call for proposals "Funding Opportunity Number: DE-FOA-0000239" in December 2010 which states inter alia that "there are concerns regarding the lack of transparency in the rare earth magnet supply market and its price structures, which imply rare earth magnets could be significantly more expensive and possibly not available in

quantities appropriate for their use in vehicle traction drives in the future. Because of this, it is desired to pursue motor technologies that sufficiently reduce/eliminate the use of rare earth permanent magnets [5]."

For the BLDCHM, the rotor is the external housing as indicated in Figure 3.5.
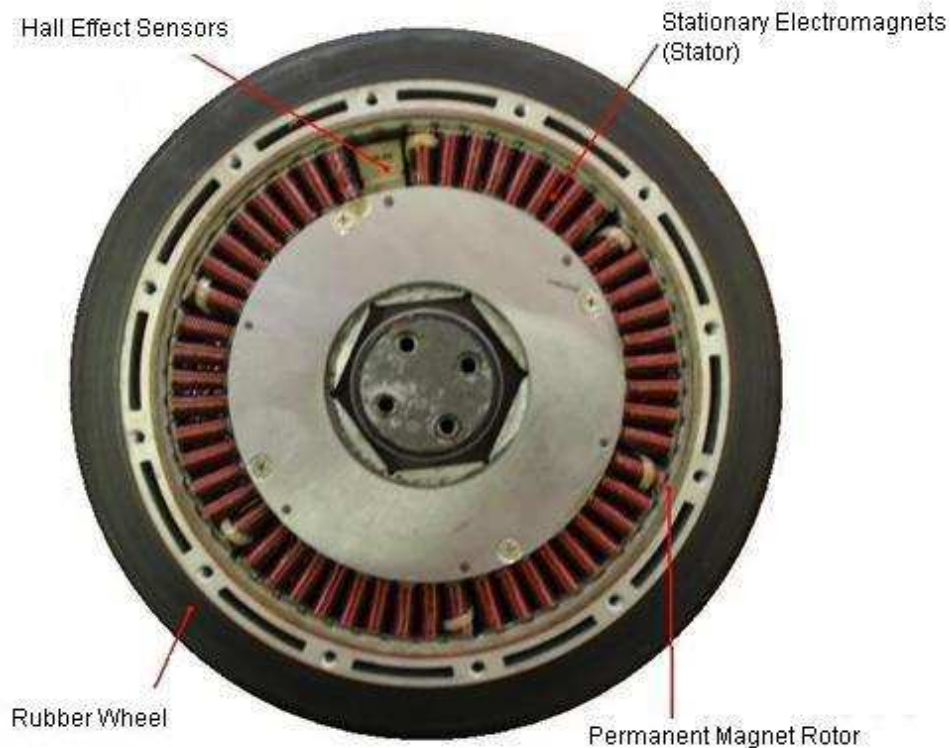
Figure 3.5 Cross section of a 28 pole BLDCHM with uniform air gap

To reduce the effect of cogging torque two primary mechanical design effects are used;

    a)   Uniform air gap compared to non-uniform air gap.

    b)   Magnet skewing effect.

3.2.2.1   Uniform air gap compared to non-uniform air gap

Figure 3.6 depicts a BLDC motor with a centralized rotor and exterior stator, though the principle in this section can be extrapolated to a BLDCHM. A uniform air gap (Figure 3.6 (1)) [24] compared to non-uniform air gap (Figure 3.6 (2)) can be implemented in a BLDCM. In Figure 3.6 (1) the magnet surface at the air gap is shaped into three flat surfaces which is almost an arc concentric to the stator surface, thus producing an air gap that is almost uniform. However in

Figure 3.6 (2) the magnet surface at the air gap is the shape of a "bread loaf", thus producing a non-uniform air gap that is shorter at the centre of the rotor pole, and longer at the edges of the rotor pole. Reference [24] reports that the non uniform air gap design with the "bread loaf" shaped magnets produces a lower cogging torque than the uniform air gap design as illustrated in Figure 3.6; moreover, the amount of reduction depends on the exact profile of the "bread loaf".

To obtain the results in Figure 3.6, the authors in [24] rotated the rotor by a fraction of the stator slot pitch, calculated the resulting torque, and repeated the process.
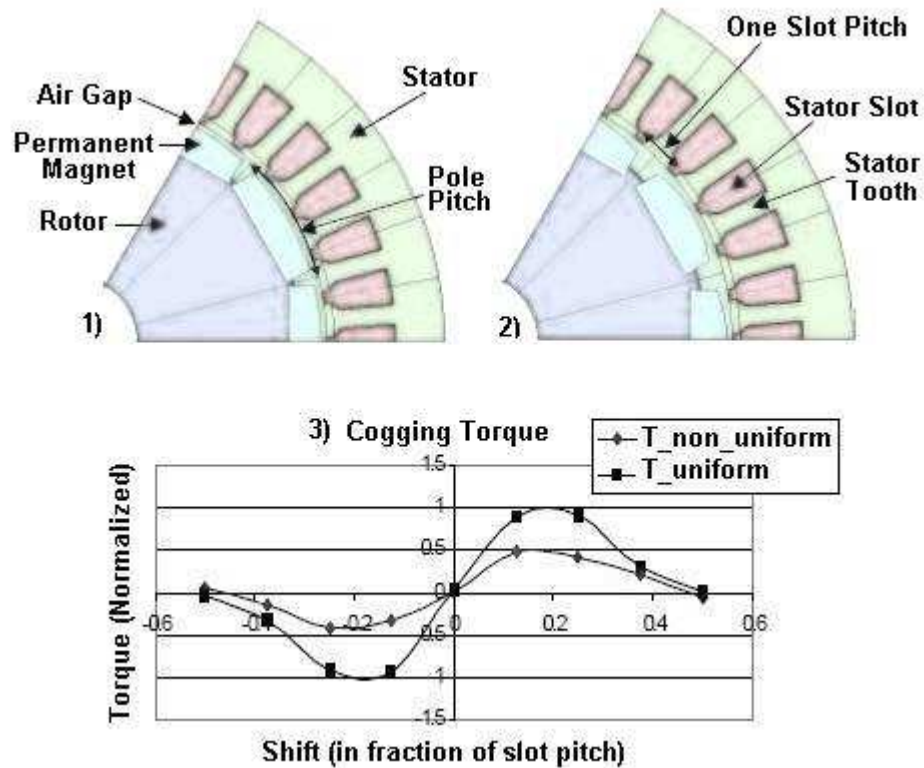
Figure 3.6 The effects of air gap uniformity on cogging torque [24]

3.2.2.2   Magnet skewing effect

The magnets on the rotor can be skewed by spatially skewing one end of the magnet with respect to the other as depicted in Figure 3.7 (a) [24]. The amount of skew determines the reduction in cogging torque. Figure 3.7 (b) shows the variation of cogging torque when the stator is skewed by different fractions of the rotor slot pitch. Skewing by one complete rotor slot pitch gives the best results in Figure 3.7 (b), but there are the following disadvantages:

a) The magnets need to be manufactured with the specific skewing shape, which results in complex geometry, thus increasing cost.

b) The total efficiency of the motor is reduced as the magnetic flux between the 'd' and 'q' axes are no longer at 90°.
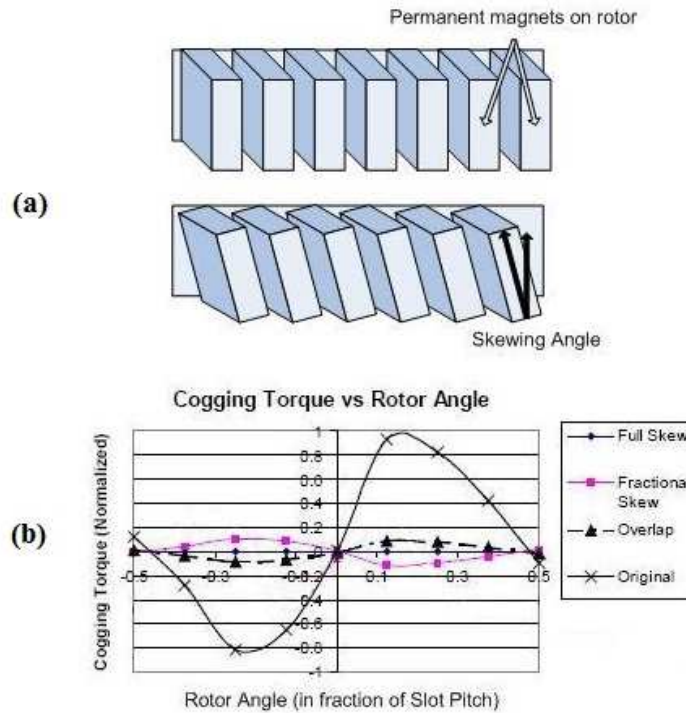
Figure 3.7 Cogging torque as a function of rotor angle at different skewing angles [24]

3.3 Correct commutation operation

A brushless direct current hub motor (BLDCHM) has no mechanical commutator and it uses an electrical commutator in the form of IGBTs or MOSFETs but their switching of current through the phase windings has to be in a sequence which is position-dependent as described in section 3.2. The position sensor is described in section 3.4. A commutation algorithm is needed to determine the switching sequence for the BLDCHM phase voltages. Based on the trapezoidal back EMF of a BLDCHM (Figure 3.8 A), two commutation strategies for the phase voltages are shown in Figure 3.8 B, namely 120 degree commutation and 180 degree commutation. The resulting current for each of these commutation strategies is shown for a single phase in Figure 3.8 C.
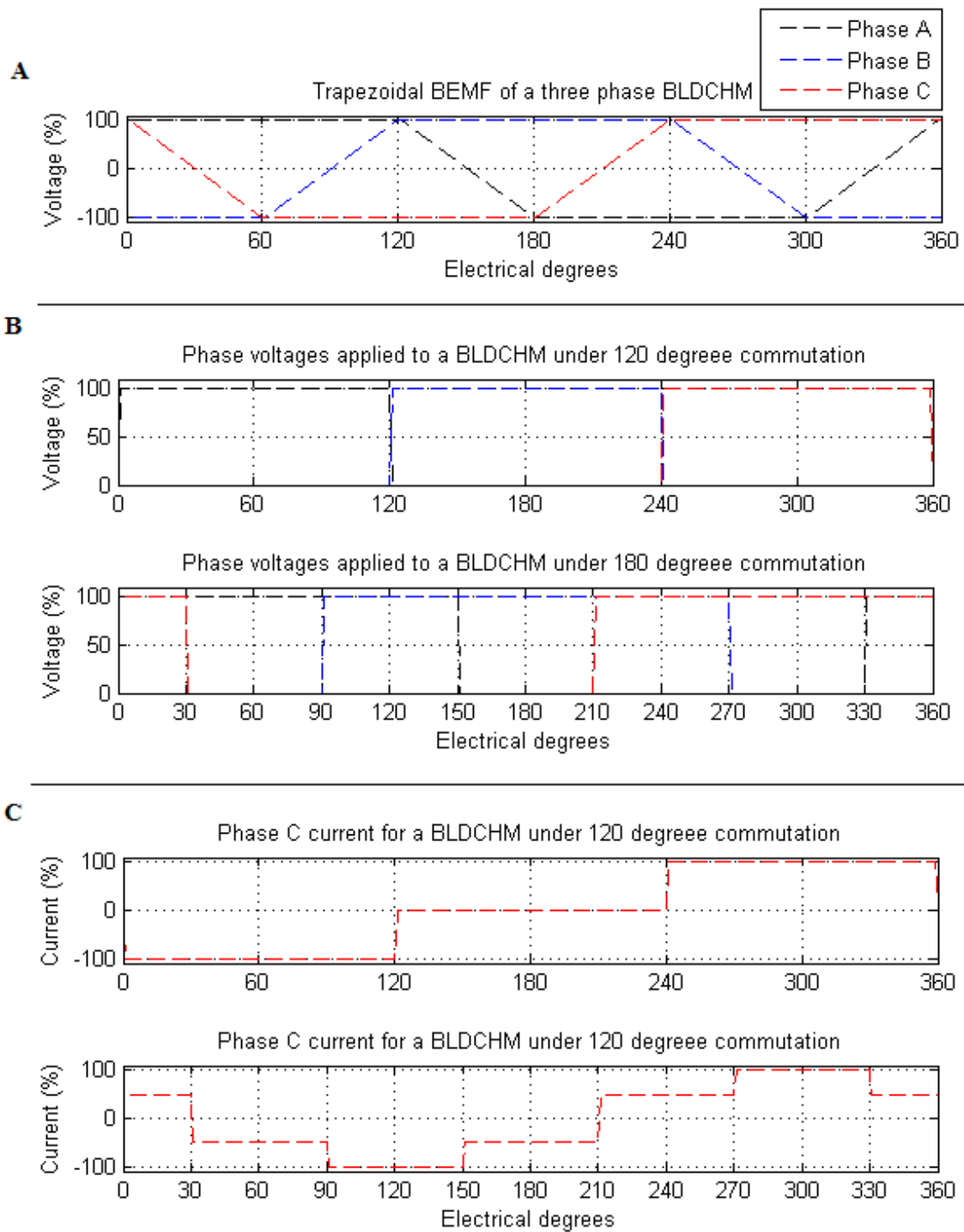
Figure 3.8 Commutation strategies based on the back EMF of a BLDCHM

3.3.1   120 degree commutation

From the back EMF waveforms in Figure 3.3, a six step commutation scheme is devised. When a phase has maximum back EMF, current is sourced into the phase and when the back EMF is at a minimum, current is sunk from the phase. Only two phases conduct at any point in time, and the conduction path is position dependent [4, 5, 25]. The current flow explanation for the six step commutation is documented in Table 3.1 and a diagram for the current flow appears in Figure 3.9. This commutation strategy is the most widely implemented solution for a BLDCHM [26].

Table 3.1 Description of current flow in a BLDC motor during 120 degree commutation [4]

θ_e (degrees)		Description
0 - 60	1	Current flows from Phase A to Phase B, whilst Phase C has a floating potential
60 - 120	2	Current flows from Phase A to Phase C, whilst Phase B has a floating potential
120 – 180	3	Current flows from Phase B to Phase C, whilst Phase A has a floating potential
180 – 240	4	Current flows from Phase B to Phase A, whilst Phase C has a floating potential
240 – 300	5	Current flows from Phase C to Phase A, whilst Phase B has a floating potential
300 – 360	6	Current flows from Phase C to Phase B, whilst Phase A has a floating potential
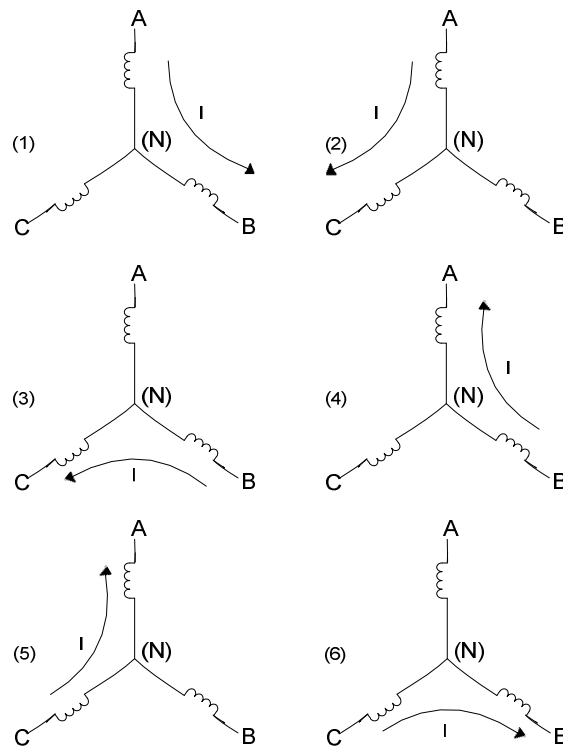
Figure 3.9 Current flow in a BLDC motor during 120 degree commutation [4]

3.3.2   180 degree commutation

180 degree commutation is suggested by Jani [27]. The concept is to increase the torque output of the motor by having all three phases conduct throughout one complete revolution of the shaft, as opposed to 120 degree commutation where each phase only conducts for 66% of one complete revolution of the shaft. However a dead band between upper and lower MOSFETs is imperative to prevent shoot-through currents. This commutation method provides a smoother output torque as the current switching between phases is overlapped electrically and allows for control strategies such as space vector modulation.

The current flow explanation for the six step commutation is documented in Table 3.2 and a diagram for the current flow appears in Figure 3.10.

Table 3.2 Description of current flow in a BLDC motor during 180 degree commutation [27]

θ_e (degrees)		Description
30 - 90	1	Current flows from Phase A to Phase B and C
90 - 150	2	Current flows from Phase A and B to Phase C
150 – 210	3	Current flows from Phase B to Phase A and C
210 – 270	4	Current flows from Phase B and C to Phase A
270 – 330	5	Current flows from Phase C to Phase A and B
330 – 30	6	Current flows from Phase A and C to Phase B
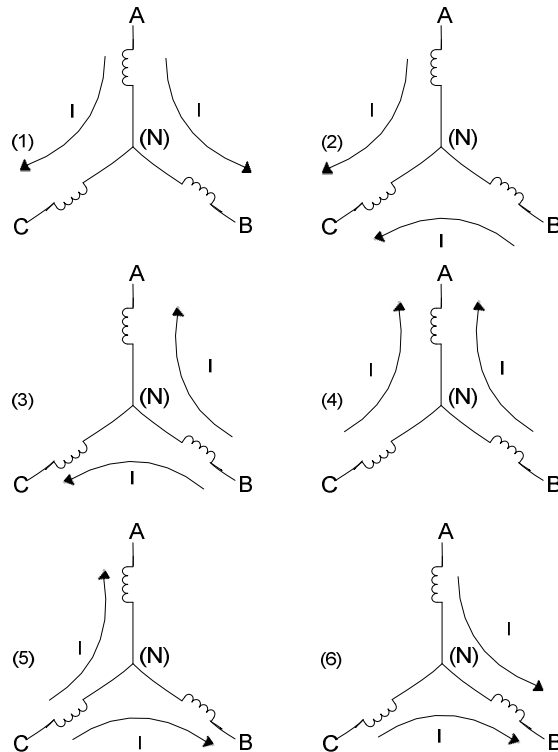
Figure 3.10 Current flow in a BLDC motor during 180 degree commutation [27]

3.3.3   Control of solid-state switches

There are three possible states that a motor phase can be in.

1. High: The phase is connected to the supply maximum potential (+Vcc) and current flows to the neutral point (N).

2. Low: The phase is connected to the supply minimum potential (-Vcc if it is a split power supply or 0V) and current flows from the neutral point.

3. Floating: The phase is not connected and thus has no current flow through it. In this state the potential measured on the phase is the same as the neutral point (denoted by a "-" in Table 3.3).

To achieve these three states only two switches per phase are required. The switching positions are determined from Figure 3.9 and Figure 3.10 for 120 and 180 degree commutation strategies respectively and are shown in Table 3.3 and Table 3.4 respectively. For each commutation strategy there are six discrete switching configurations, allowing each strategy to be referred to as a "six-step" commutation strategy.

Table 3.3 Commutation using 120 degree switching [4]

θ_e (Deg)	θ_e (rad)	Phase A	Phase B	Phase C
$0 < \theta_e \leq 60$	$0 < \theta_e \leq \frac{1}{3}\pi$	High	Low	-
$60 < \theta_e \leq 120$	$\frac{1}{3}\pi < \theta_e \leq \frac{2}{3}\pi$	High	-	Low
$120 < \theta_e \leq 180$	$\frac{2}{3}\pi < \theta_e \leq \pi$	-	High	Low
$180 < \theta_e \leq 240$	$\pi < \theta_e \leq \frac{4}{3}\pi$	Low	High	-
$240 < \theta_e \leq 300$	$\frac{4}{3}\pi < \theta_e \leq \frac{5}{3}\pi$	Low	-	High
$300 < \theta_e \leq 360$	$\frac{5}{3}\pi < \theta_e \leq 2\pi$	-	Low	High

120 degree switching is the most common system implemented. The phase voltages are applied at the same electrical position as the peak of the back EMF wave.

Table 3.4 Commutation using 180 degree switching [27]

θ_e (Deg)	θ_e (rad)	Phase A	Phase B	Phase C
$30 < \theta_e \leq 90$	$\frac{1}{6}\pi < \theta_e \leq \frac{1}{2}\pi$	High	Low	Low
$90 < \theta_e \leq 150$	$\frac{1}{2}\pi < \theta_e \leq \frac{5}{6}\pi$	High	High	Low
$150 < \theta_e \leq 210$	$\frac{5}{6}\pi < \theta_e \leq \frac{7}{6}\pi$	Low	High	Low
$210 < \theta_e \leq 270$	$\frac{7}{6}\pi < \theta_e \leq \frac{3}{2}\pi$	Low	High	High
$270 < \theta_e \leq 330$	$\frac{3}{2}\pi < \theta_e \leq \frac{11}{6}\pi$	Low	Low	High
$330 < \theta_e \leq 330$	$\frac{11}{6}\pi < \theta_e \leq \frac{1}{6}\pi$	High	Low	High

The layout for the six solid-state switches in the inverter, allows for current flow though each phase, in either direction. The electrical connection for the MOSFET inverter is documented in Chapter 2.

3.4   **Position sensing and estimation**

For electrical commutation of the current in a BLDCHM, the electrical position of the rotor is typically required at 60 degree intervals. The most common method is to place three Hall effect sensors inside the motor. Another method is that of sensorless commutation, which is based on accurate position estimation. It is important to note that the electrical position is seldom the same as the mechanical position of the motor as the number of pole pairs need to be taken into account.

3.4.1   Discrete sensor

Discrete Hall effect sensors within the stator detect the permanent magnetic field of the rotor. As a pole passes the sensor, it returns either a high level indicating a north pole or a low level indicating a south pole. This is shown in

Figure **3.11** and the circuit configuration is depicted in Figure 3.12. Within the control algorithm, these position signals are then interpreted and used to switch the inverter, and thus control the current in the motor.

Discrete 120 degree sensing is a cheap solution but has disadvantages. The position resolution is limited to a discrete interval depending on the number of embedded sensors, which makes speed control inaccurate at low speeds. To calculate which of the six-step locations the motor is in, a minimum of three such sensors are required. With the sensors mechanically positioned 120 electrical degrees apart, a resolution of 60 electrical degrees is obtained. The next section describes how to obtain a finer resolution than only every sixty electrical degrees.
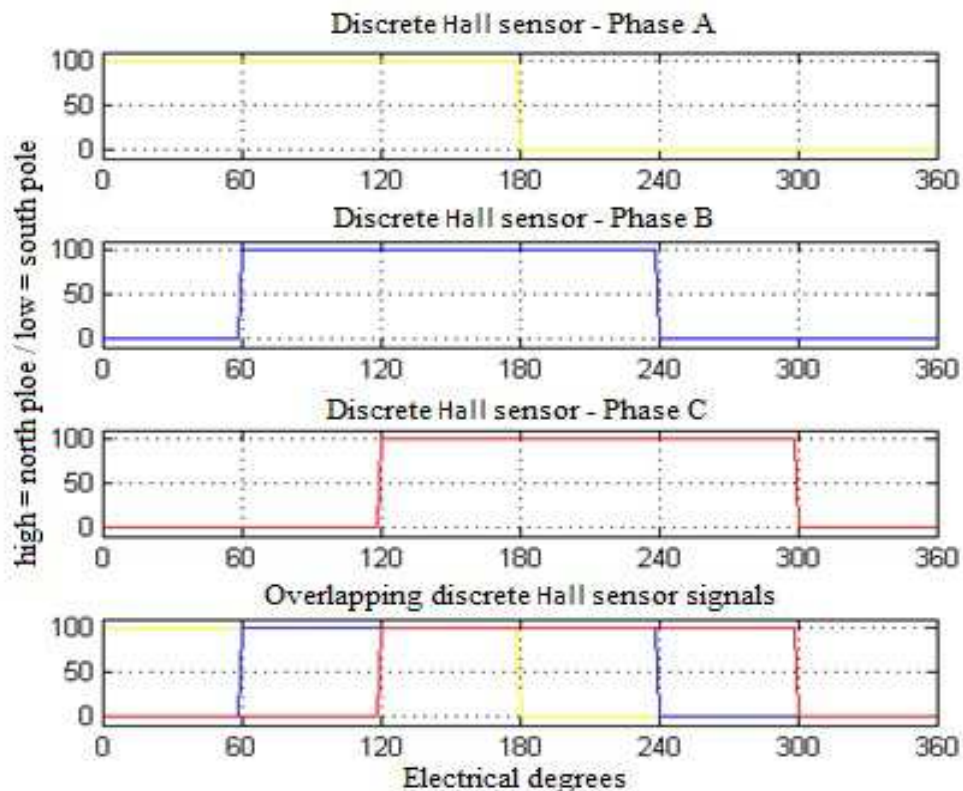
Figure 3.11 Signals received from discrete Hall sensors [26]
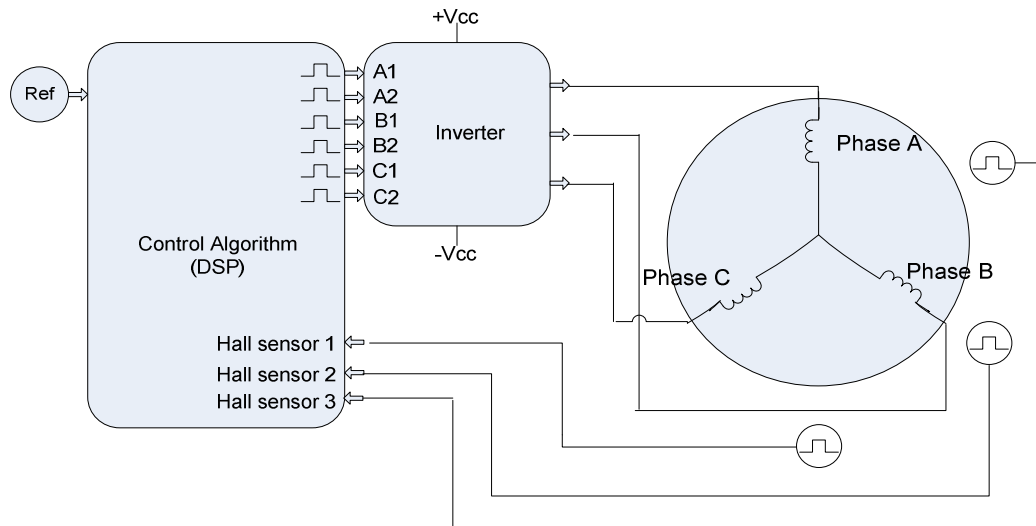
Figure 3.12 Circuit configuration for discrete Hall sensors

3.4.2   Continuous sensors

To determine the position of a rotor with a finer resolution than only every sixty electrical degrees, an encoder can be used instead of discrete sensors at 120 degree intervals. Another approach is to place analogue Hall effect sensors on the stator and for this setup, there are two sensors within the motor. The feedback from each sensor is sinusoidal and directly dependent on the sensor's position relative to a pole. With the placement of two of such units, 90 electrical degrees apart (as appears in Figure 3.14), the exact position of the rotor can be determined by using the analogue feedback signals from Hall sensor 1 and Hall sensor 2 [28]. Equation (3.1) is calculated within the control unit, and then used for the inverter timing, thereby controlling the current in the motor. The circuit configuration appears in Figure 3.14. This implementation has the advantage of increased position resolution, allowing for accurate calculation of the motor speed (first integral of position) and acceleration (second integral of position) for moment to moment.

$$\theta_e = atan2\left(\frac{Hall_1}{Hall_2}\right) \tag{3.1}$$

where:

- θ_e is the electrical angle of the rotor (degrees).

- *Hall₁* is the magnitude of the analogue voltage feedback signal from the first Hall effect sensor.

- *Hall₂* is the magnitude of the analogue voltage feedback signal from the second Hall effect sensor.
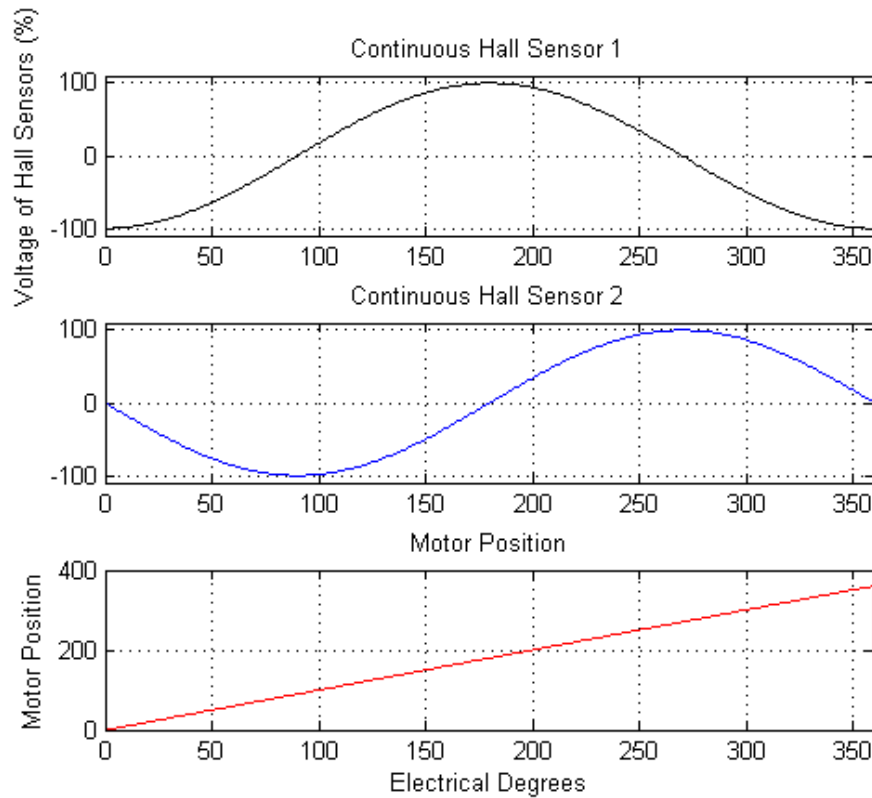
Figure 3.13 Motor position and continuous Hall sensor signals for a rotor turning at constant speed [26]
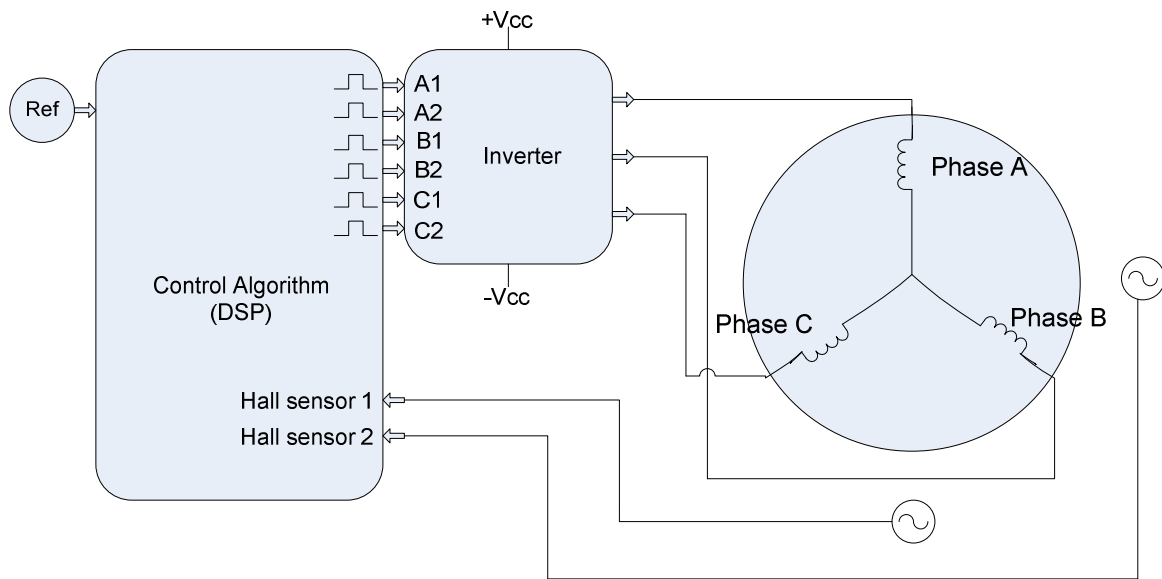
Figure 3.14 Circuit configuration for continuous Hall sensors

3.4.3   Sensorless position estimation

The back EMF waveforms in a BLDCHM are trapezoidal, as appears in Figure 3.3.There are many applications that allow for a basic position estimation to be based directly measuring on the back EMF, thereby eliminating the expense of position sensors. It is important to note that only one of the two types of commutation strategy (120 and 180 degrees) discussed in section 3.3, can use sensorless position estimation. The common 120 degree commutation strategy drives only two of the phase windings at any particular point in time. This allows the measurement of the back EMF of the floating phase. When a phase is open circuit, the back EMF measured across its terminals follows the profile in Figure 3.3. The commutation algorithm can detect the per phase back EMF as it crosses the average or zero point (situated half way between the positive and negative rails). This happens twice per phase in a single electrical cycle. Based on the time interval between zero detection, the rotational speed can be estimated and then used to calculate the position. Once a position estimate is obtained, the inverter timing can be calculated. The basic circuit layout is shown in Figure 3.15. The primary problem with this sensorless position estimation occurs at low speeds where there is a small back EMF from which to monitor the zero crossing and at zero speed the position is impossible to determine.
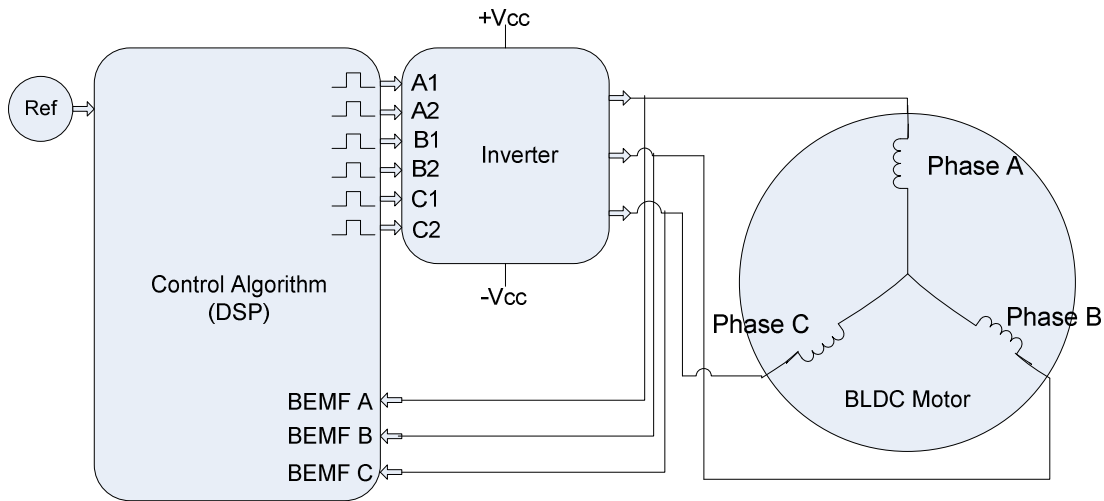
Figure 3.15 Hardware configuration for sensorless commutation

3.5   Torque generation in a BLDC motor

Figure 3.16 shows the winding structure of a BLDCH motor with central stationary windings and an outer permanent magnet rotor. The individual phase voltages and currents are shown as well as the flux vector from the permanent magnetic rotor. To generate torque in a BLDCHM, the resultant current vector (i_s) must lead the exterior rotor flux (λ_f) linkage vector. For maximum torque production and the most efficient current to torque ratio the angle between i_s and λ_f should be 90° [4]. A leading current vector is illustrated in Figure 3.17 where λ_f is at 0° with respect to Phase A. Considering the winding structure of the BLDCHM (as appears in Figure 3.16), for a resulting i_s to be produced at 90° leading λ_f, the following is required:

- Phase A carries zero current, thus producing no flux.
- Phase B carries a positive current, thus producing a current flux vector at 120°.
- Phase C carries a negative current equal in magnitude to Phase B, producing a current flux vector at 60°.

These conditions will result in i_s leading λ_f as required. This principle is the basis for determining the commutation strategies in section 3.3.
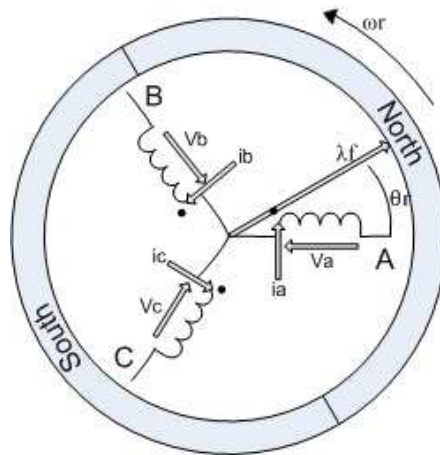
Figure 3.16 Winding structure of a BLDCHM with per phase current and voltage vectors [4]
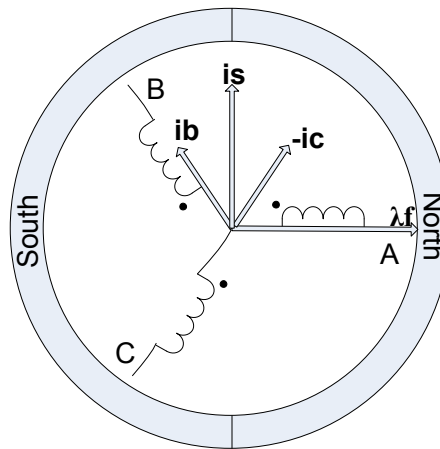
Figure 3.17 Resultant current and flux vector within a BLDCHM at 0° [4]

3.6   **Regenerative braking of a BLDCHM**

The need for braking in any EV is apparent and this is achieved by controlling the motor to become a generator. The advantages of using the BLDCHM as a generator are:

- In braking (or generator) mode, the BLDCHM acts as a brake, thus removing the cost of a hydraulic braking system.
- It allows the implementation of regeneration, converting mechanical energy into electrical energy which is stored in the battery, thus increasing the operational distance of the EV.

When the vehicle is in braking mode, the kinetic energy is converted into electrical energy and reduces the velocity of the vehicle. There are two electrical states during braking, namely energy storage in magnetic fields and energy used to recharge batteries. To further understand the operation, consider a BLDCHM rotating from 0° to 60° electrically [13, 31, 32].

a) Energy Storage: When the BLDCH motor is at 0°, Figure 3.8 A shows that phase A is at a maximum back EMF potential and Phase B is at a minimum back EMF potential. Only Q2 in Figure 3.18 is switched to an on-state, creating a circulating current path as appears in Figure 3.18 (a) and energy is stored in the magnetic fields of phases A and B.

b) Recharging: When Q2 is switched to an off state, the only available current path for the stored energy in phases A and B is via the fly back diodes and into the batteries as appears in Figure 3.18 (b). This reverse current through the batteries recharges them.

When steps a) and b) above are repeated at high frequency by using a PWM signal to the bottom MOSFETs in a position dependent sequence, a regenerative state is produced. This process is extended to Q4 and Q6 to achieve regeneration through 360° of motor rotation.
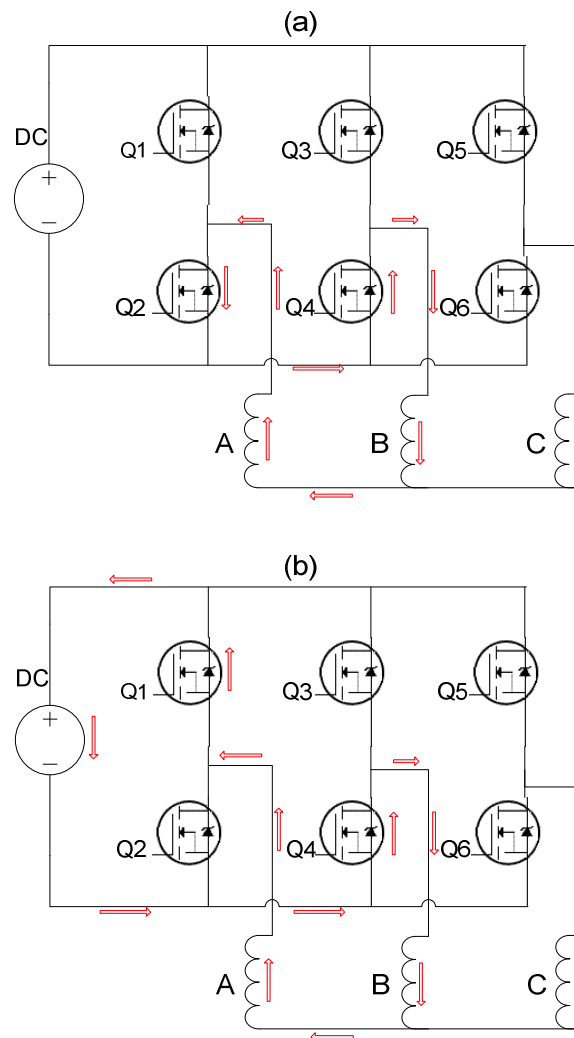
Figure 3.18 Current paths during regenerative braking operation [30]

3.7   **Summary**

This chapter has considered the structure and control of the BLDCHM as well as the required position sensors and regenerative braking. The construction and operation of the rotor and stator have been documented as well as mechanical alterations, which reduce cogging torque. The inverter commutation is position-dependent and position-sensing and estimation principles have been investigated. To understand the electrical and dynamic responses of a BLDCM (and by extension, the power inverter), the mathematical equations, which govern them, are developed in Chapter 4.

Chapter 4 - Dynamic and Electrical Model of a BLDCHM

4.1   Introduction

The brushless DC hub motor (BLDCHM) is a star-connected three phase motor, using an inverter with a specific, position-dependent, commutation pattern to control the current into each of the motor phases. The motor cannot be fed from an AC supply like an induction motor, or directly from a DC supply like a conventional DC motor. A specific sequence needs to be followed to enable correct commutation.

This chapter focuses on the equivalent electrical circuit of the BLDCHM, and a mathematical analysis is done on both the motor and the inverter.

4.2   Mathematical model for the BLDC motor

In many "sinusoidal motor" types that require sinusoidal voltage or current supplies, such as induction and certain permanent magnet synchronous machines, a *d,q* axis mathematical model is used. With the BLDCHM an *a,b,c* mathematical model approach is preferred because the back EMF wave forms are trapezoidal which complicates a mathematical transformation into the *d,q* reference frame. Whilst doing a Fourier Transform of the trapezoidal back EMF and then transferring each harmonic to a *d,q* reference frame is theoretically possible, it is not undertaken as the result is complex [4, 6, 37]. Thus in this investigation the modeling of the BLDCM assumes a purely trapezoidal back EMF although on the measured waveforms the corners of the back EMF are slightly rounded. For purposes of mathematical analysis it is nevertheless assumed that the back EMF is purely trapezoidal and that it can be represented by a linear piecewise function dependent on the rotor position and for which the magnitude is proportional to speed.

The simplified winding structure for the BLDCHM used in this research is shown in Figure 4.1. The motor is a 56-pole, 3-phase BLDCM with inner stator windings around the stationary shaft assembly and permanent magnets mounted on the inside surface of the cylindrical outer rotating assembly of the wheel. This version is called a surface-mounted BLDCM or BLDCHM. The equivalent electrical circuit is shown in Figure 4.2. Each one of the three phase windings is

represented by a resistance in series with a self inductance, a voltage source representing the back EMF, and a mutual inductance between the phases.

Assumptions used to simplify the BLDCHM model are as follows [36, 40]:

- The magnetic circuit is linear (saturation is neglected).
- The cogging torque is not considered.
- The effect of temperature on the stator windings and laminations is not considered.

Considering Figure 4.2, the voltage vector for a BLDCHM is represented below and the full equation is derived in this chapter:

$$\boldsymbol{V} = [R]\boldsymbol{I} + \rho[L]\boldsymbol{I} + \boldsymbol{E} \tag{4.1}$$

where:

- $\boldsymbol{V}$ is the vector of the applied phase voltage voltages.
- R is the scalar for the individual phase resistances.
- $\boldsymbol{I}$ is the vector of the resultant phase currents.
- ρ is the Heaviside Differential Operator.
- L is the scalar for the individual phase inductances.
- $\boldsymbol{E}$ is the back EMF vector.
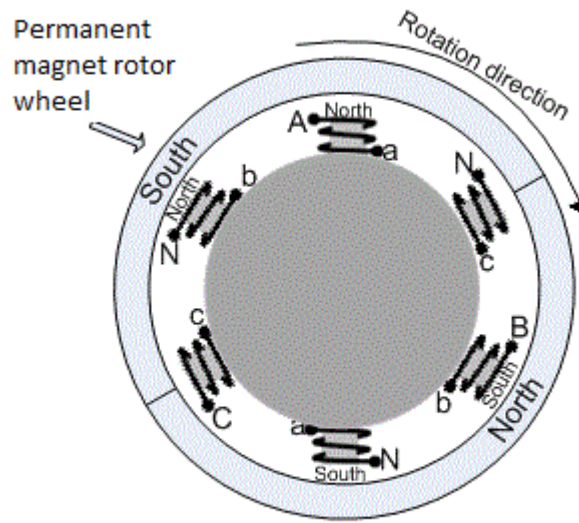
Figure 4.1 Simplified structure for the BLDCHM [8]

*Note the Neutral connection is only within the motor
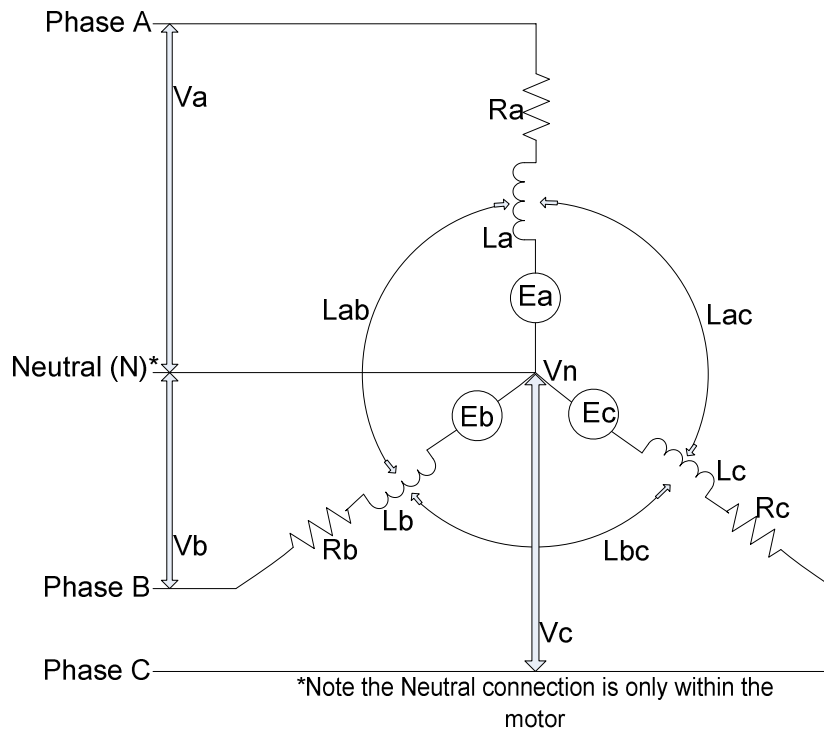
Figure 4.2 BLDCHM equivalent circuit diagram [4]

The voltage across phase A to neutral is denoted as:

$$V_{an} = (R_a) * I_a + \frac{d}{dt}\left((I_a * L_a) + (I_b * L_{ba}) + (I_c * L_{ca})\right) + E_a \tag{4.2}$$

where:

- V_{an} is the instantaneous voltage across the A phase to the neutral point (V).
- R_a is the phase series resistance (Ω).
- I_a is the instantaneous current though phase A (amps).
- I_b is the instantaneous current though phase B (amps).
- I_c is the instantaneous current though phase C (amps).
- L_a is the self inductance of phase A (henry).
- L_{ab} is the mutual inductance between phases A and B (henry).
- L_{ac} is the mutual inductance between phases C and A (henry).
- E_a is the instantaneous induced voltage or back EMF in phase A (V).

similarly:

$$V_{bn} = (R_b) * I_b + \frac{d}{dt}\left((I_b * L_b) + (I_a * L_{ba}) + (I_c * L_{bc})\right) + E_b \tag{4.3}$$

and

$$V_{cn} = (R_c) * I_c + \frac{d}{dt}\left((I_c * L_c) + (I_a * L_{ca}) + (I_b * L_{ca})\right) + E_c \tag{4.4}$$

The complete vector equation for the motor can be obtained when substituting equations (4.2), (4.3) and (4.4) into equation (4.1). V_{an}, V_{bn} and V_{cn} are denoted as V_a, V_b and V_c respectively from here on.

$$\begin{bmatrix} V_a \\ V_b \\ V_c \end{bmatrix} = \begin{bmatrix} R_a & 0 & 0 \\ 0 & R_b & 0 \\ 0 & 0 & R_c \end{bmatrix}\begin{bmatrix} I_a \\ I_b \\ I_c \end{bmatrix} + \frac{d}{dt}\begin{bmatrix} L_a & L_{ab} & L_{ac} \\ L_{ba} & L_b & L_{bc} \\ L_{ca} & L_{cb} & L_c \end{bmatrix}\begin{bmatrix} I_a \\ I_b \\ I_c \end{bmatrix} + \begin{bmatrix} E_a \\ E_b \\ E_c \end{bmatrix} \tag{4.5}$$

The assumption can be made that the mutual inductance between phases is the same. Thus $L_{ab} = L_{ac}$ = $L_{ba} = L_{bc} = L_{ca} = L_{cb} = M$, where M is known as the mutual inductance. This reduces equation (4.5) to (4.6).

$$\begin{bmatrix} V_a \\ V_b \\ V_c \end{bmatrix} = \begin{bmatrix} R_a & 0 & 0 \\ 0 & R_b & 0 \\ 0 & 0 & R_c \end{bmatrix} \begin{bmatrix} I_a \\ I_b \\ I_c \end{bmatrix} + \frac{d}{dt} \begin{bmatrix} L_a & M & M \\ M & L_b & M \\ M & M & L_c \end{bmatrix} \begin{bmatrix} I_a \\ I_b \\ I_c \end{bmatrix} + \begin{bmatrix} E_a \\ E_b \\ E_c \end{bmatrix} \qquad (4.6)$$

A further simplification can be made if the motor is considered ideal, thus assuming the three phases have equal resistance and neglecting the relationship between winding resistance and temperature [28, 36]. Then R_a, R_b and R_c are equal and can be denoted as R. If the phase inductances are also presumed to be equal, then they can be denoted by the term L. Hence

$$\begin{bmatrix} V_a \\ V_b \\ V_c \end{bmatrix} = \begin{bmatrix} R & 0 & 0 \\ 0 & R & 0 \\ 0 & 0 & R \end{bmatrix} \begin{bmatrix} I_a \\ I_b \\ I_c \end{bmatrix} + \frac{d}{dt} \begin{bmatrix} L & M & M \\ M & L & M \\ M & M & L \end{bmatrix} \begin{bmatrix} I_a \\ I_b \\ I_c \end{bmatrix} + \begin{bmatrix} E_a \\ E_b \\ E_c \end{bmatrix} \qquad (4.7)$$

The BLDCHM stator windings are assumed to be star connected, thus when considering the neutral point, Kirchhoff's current law states that:

$$I_a + I_b + I_c = 0 \qquad (4.8)$$

This allows for the following simplification:

$$\frac{d}{dt}[L * I_a + M * I_b + M * I_c]$$

$$= \frac{d}{dt}[L * I_a + M(I_b + I_c)]$$

$$= \frac{d}{dt}[L * I_a + M(-I_a)]$$

$$= \frac{d}{dt}[I_a * (L - M)] \qquad (4.9)$$

Substituting equation (4.9) into equation (4.7) reduces the voltage vector equation to (4.10).

$$\begin{bmatrix} V_a \\ V_b \\ V_c \end{bmatrix} = \begin{bmatrix} R & 0 & 0 \\ 0 & R & 0 \\ 0 & 0 & R \end{bmatrix} \begin{bmatrix} I_a \\ I_b \\ I_c \end{bmatrix} + \frac{d}{dt} \begin{bmatrix} L - M & 0 & 0 \\ 0 & L - M & 0 \\ 0 & 0 & L - M \end{bmatrix} \begin{bmatrix} I_a \\ I_b \\ I_c \end{bmatrix} + \begin{bmatrix} E_a \\ E_b \\ E_c \end{bmatrix} \qquad (4.10)$$

In a BLDCH motor, the torque output is directly related to the current flowing through the phase windings. So to obtain a smooth torque, an accurate current controller is required. When making the current the subject of the formula, equation (4.10) can be re-arranged as:

$$\frac{d}{dt}\begin{bmatrix} I_a \\ I_b \\ I_c \end{bmatrix} = \frac{\begin{bmatrix} V_a \\ V_b \\ V_c \end{bmatrix} - \begin{bmatrix} R & 0 & 0 \\ 0 & R & 0 \\ 0 & 0 & R \end{bmatrix}\begin{bmatrix} I_a \\ I_b \\ I_c \end{bmatrix} - \begin{bmatrix} E_a \\ E_b \\ E_c \end{bmatrix}}{L - M} \tag{4.11}$$

To simplify the notation, let *(L-M)* be replaced by the symbol *L1*:

$$\frac{d}{dt}\begin{bmatrix} I_a \\ I_b \\ I_c \end{bmatrix} = \begin{bmatrix} V_a/L1 \\ V_b/L1 \\ V_c/L1 \end{bmatrix} - \begin{bmatrix} R/L1 & 0 & 0 \\ 0 & R/L1 & 0 \\ 0 & 0 & R/L1 \end{bmatrix}\begin{bmatrix} I_a \\ I_b \\ I_c \end{bmatrix} - \begin{bmatrix} E_a/L1 \\ E_b/L1 \\ E_c/L1 \end{bmatrix} \tag{4.12}$$

In a regular industrial type BLDC motor the rotor architecture uses permanent magnets and while the flux density varies across a rotor magnetic pole, the total flux per pole is nevertheless constant. The trapezoidal shape of the back EMF waveform depends on the position of a phase winding relative to the magnets, with a phase shift of 120 degrees between phases. The amplitude of the back EMF depends only on the motor speed. The equations for the back EMF are shown below. An assumption is made that phase A and the electrical position feedback θ_e are aligned. In practice this is not necessarily the case and an offset to the position feedback might be required.

$$E_a = K_v * \omega_m * f(\theta_e)$$

$$E_b = K_v * \omega_m * f(\theta_e + 120) = K_v * \omega_m * f(\theta_e + \frac{2}{3}\pi)$$

$$E_c = K_v * \omega_m * f(\theta_e - 120) = K_v * \omega_m * f(\theta_e - \frac{2}{3}\pi) \tag{4.13}$$

where:

- E_a, E_b and E_c are the instantaneous trapezoidally shaped induced back EMFs (V).
- K_v is the motor speed constant (V.s/rad).
- ω_m is the motor rotational speed (rad/sec).
- $f(\theta_e)$ is the linear piecewise function describing the back EMF wave (no unit).

The back EMF wave has the same shape for all three phases, but with an angular phase-shift of 120 degrees ($\frac{2}{3}\pi$ radians). This shift is a mechanical property designed in the layout of the rotor magnets and stator windings. To further understand the linear piecewise function for the back EMF, phase A (E_a) is considered. The ideal back EMF waveforms are shown in Figure 4.3.

$$E_a = K_v * \omega_m * \begin{cases} 1 & \text{where } 0 \leq \theta_e < \pi/3 \\ 1 & \text{where } \pi/3 \leq \theta_e < 2\pi/3 \\ -\left(6*(\theta_e - 2\pi/3)\right)/\pi & \text{where } 2\pi/3 \leq \theta_e < \pi \\ -1 & \text{where } \pi \leq \theta_e < 4\pi/3 \\ -1 & \text{where } 4\pi/3 \leq \theta_e < 5\pi/3 \\ \left(6*(\theta_e - 5\pi/3)\right)/\pi & \text{where } 5\pi/3 \leq \theta_e < 2\pi \end{cases} \tag{4.14}$$
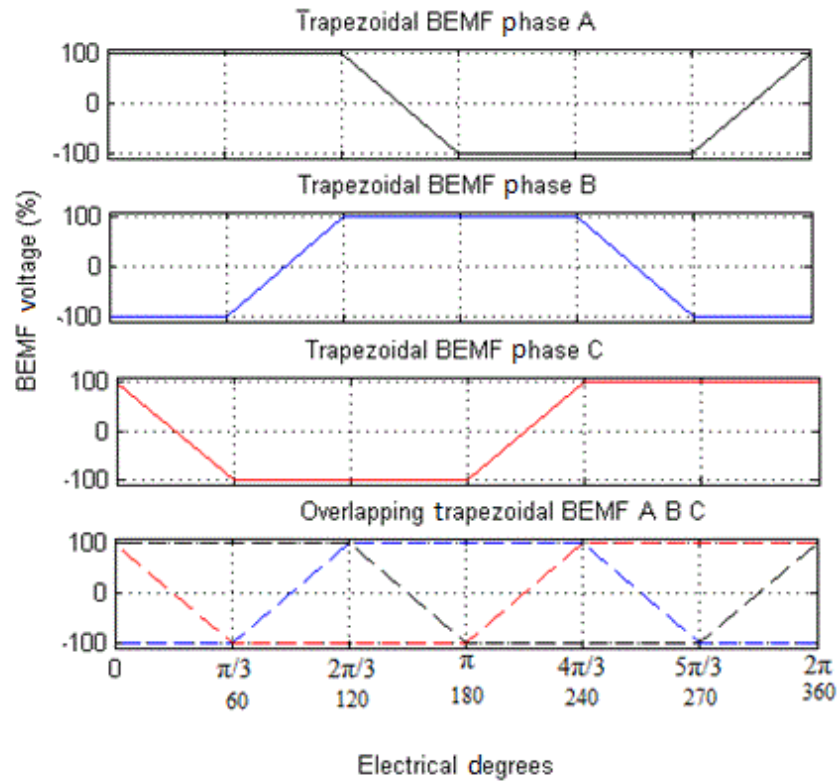
Figure 4.3 Ideal back EMF waveforms from a BLDC motor [4]

The electromagnetic torque is the quotient of the total electromagnetic power and the electrical rotational speed, as a function of time.

$$T_e(t) = (E_a * I_a + E_b * I_b + E_c * I_c)/\omega_m$$

$$T_e(t) = (E_a * I_a + E_b * I_b + E_c * I_c)/(\omega_e * P/2) \tag{4.15}$$

The mechanical equation of motion for the motor is:

$$J\left[\frac{d\omega_m}{dt}\right] + B_f \omega_m = T_e(t) - T_l(t)$$

$$J\left[\frac{d\omega_e}{dt}\right] + B_f \omega_e = \frac{P}{2}[T_e(t) - T_l(t)] \tag{4.16}$$

where:

- J is the motor inertia (kg.m^2).

- B_f is the friction coefficient (N-m per radian per second).

- T_e *(t)* is the electrical torque as a function of time (N-m).

- T_l *(t)* is the load torque as a function of time (N-m).

- P is the number of pole pairs in the motor.

The rotational inertia of a BLDCHM (or object) is a property of the mass and distance between the mass and the centre of rotation and can thus be determined mathematically using the integration of the mass and distance over the profile of the wheel. This becomes difficult when the object such as a BLDCHM, is made of a complex profile and multiple materials. The coefficient of friction between the BLDCHM wheel and the surface is a physical property and cannot be altered electrically.

From equation (4.16) the electromagnetic torque depends on the rotational speed and the current in each phase. When substituting equation (4.14) into equation (4.17) and rearranging:

$$\frac{d\omega_m}{dt} = \frac{1}{J}\left[\frac{E_a * I_a + E_b * I_b + E_c * I_c}{\omega_m} - T_l(t) - B_f\omega_m(t)\right] \tag{4.17}$$

However from equation (4.14), the back EMFs E_a, E_b and E_c are functions of time and ω_m. This reduces equation (4.17) to:

$$\frac{d\omega_m}{dt} = \frac{1}{J}\left[\left[K_v * f(\theta_e) * I_a + K_v * f\left(\theta_e + \frac{2\pi}{3}\right) * I_b + K_v * f\left(\theta_e - \frac{2\pi}{3}\right) * I_c\right]\frac{\omega_m}{\omega_m} - T_l - B_f\omega_m\right] \tag{4.18}$$

To simplify the motor equation, $F_A(\theta_e)$, $F_B(\theta_e)$ and $F_C(\theta_e)$ are used to represent the product of the motor speed constant and the linear piecewise functions in the back EMF equations. It is important to note that the $2\pi/3$ phase shifts are accommodated for in $F_B(\theta_e)$ and $F_C(\theta_e)$.

$$\frac{d\omega_m}{dt} = \frac{1}{J}[F_a(\theta_e) * I_a + F_b(\theta_e) * I_b + F_c(\theta_e) * I_c - T_l(t) - B\omega_m(t)] \tag{4.19}$$

From equation (4.19), the electrical torque in equation (4.15) can be reduced to a point where it is solely reliant on the phase current and not the rotational speed. This implies that current control in the BLDC motor provides an accurate torque control. Intuitively from equation (4.15), to obtain

maximum constant torque at any speed, the three phase currents must be rectangular and in phase with their respective back EMF signals [4].

It is not physically possible to have a perfectly rectangular current due to the inductance in the phases, thus resulting in cogging torque. As documented in Chapter 2, various methods have been investigated to reduce the cogging effect. This includes a 180 degree commutation scheme. Experimental data and final selection for the controller design is documented in Chapter 5.

Finally the mechanical position of the motor is defined by:

$$\frac{d\theta_m}{dt} = (P) * \omega_e \tag{4.20}$$

$$\theta_e = (P) * \theta_m \tag{4.21}$$

To conclude, the final state space equation (4.22) below, for a three-phase, star-wound, trapezoidal back EMF, BLDCHM is obtained directly from equations (4.12), (4.19) and (4.20), in the form: **x' = Ax + Bu**.

$$\frac{d}{dt}\begin{bmatrix} I_a \\ I_b \\ I_c \\ \omega_m \\ \theta_e \end{bmatrix} = \begin{bmatrix} -R/L1 & 0 & 0 & -F_a(\theta_e)/L1 & 0 \\ 0 & -R/L1 & 0 & -F_b(\theta_e)/L1 & 0 \\ 0 & 0 & -R/L1 & -F_c(\theta_e)/L1 & 0 \\ F_a(\theta_e)/J & F_b(\theta_e)/J & F_c(\theta_e)/J & -B/J & 0 \\ 0 & 0 & 0 & P & 0 \end{bmatrix} \begin{bmatrix} I_a \\ I_b \\ I_c \\ \omega_m \\ \theta_e \end{bmatrix} + \begin{bmatrix} 1/L1 & 0 & 0 & 0 \\ 0 & 1/L1 & 0 & 0 \\ 0 & 0 & 1/L1 & 0 \\ 0 & 0 & 0 & -1/J \\ 0 & 0 & 0 & 0 \end{bmatrix} \begin{bmatrix} V_a \\ V_b \\ V_c \\ T_l \end{bmatrix} \tag{4.22}$$

The state variables are I_a, I_b, I_c, ω_m and θ_m. The input variables are V_a, V_b, V_c and T_l.

4.3   **Mathematical model for the inverter**

Unlike other motors which can run from a utility mains or a DC source, the BLDCHM commutation relies on the electrical position of the rotor to control the current waveforms. This makes the inverter a critical part for motion control, and often in the literature such as Wishart [4], the entire motor and inverter are viewed as one unit, referred to as the BLDC machine.

For the modeling of the inverter the assumption is made that all six switches which are controlled by the computation algorithm, are ideal switches. This implies:

a) The individual switch's electrical characteristics are not modeled.

b) Control signals are all independent and complementary switching is not used on the inverter.

c) It is assumed that the DC supply to the inverter is constant.

d) To determine a generic model for the inverter the positive DC rail is referred to as +Vcc and the negative rail –Vcc.

e) A zero reference potential, V_0 is defined as the potential midway between the DC rail voltages. The voltages imposed onto the BLDCHM phases are referenced to V_0.
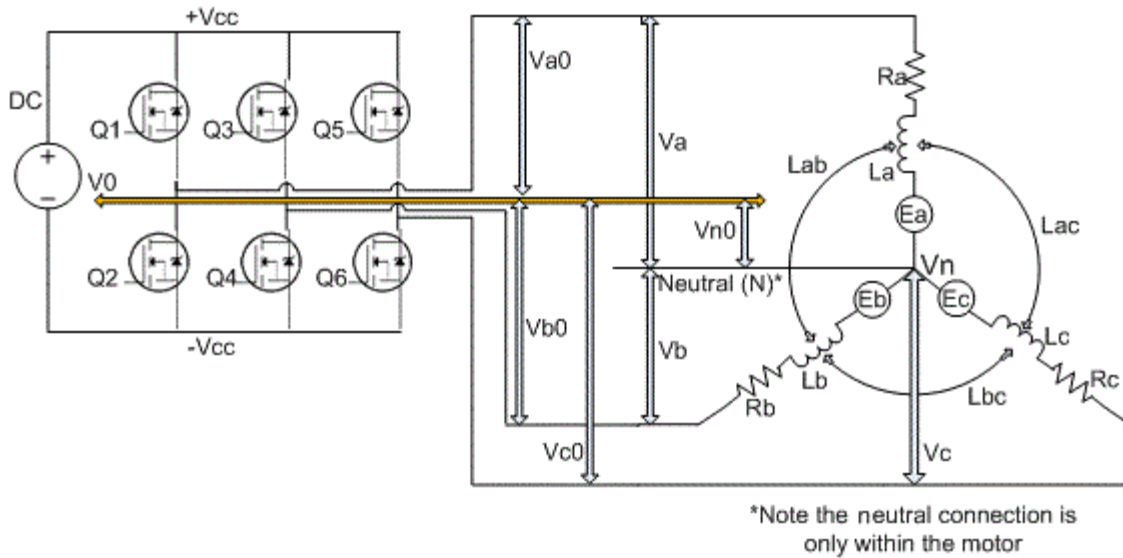
Figure 4.4 Voltage potentials between the inverter and BLDCHM [4]

The voltages V_a, V_b and V_c (the phase potentials in equation (4.22) are relative to the neutral point (V_n) within the motor. The current within each phase is dependent on its phase voltage, however the inverter cannot supply a potential directly referenced to V_n as it is a connection only within the motor. Pillay [7] makes the assumption that V_n is always at the same potential as V_0 which makes the model simplistic. However this is not actually the case and the neutral point (referenced to V_0) follows the back EMF of the phases (presuming 120 degree commutation) as appears in Figure 4.5.
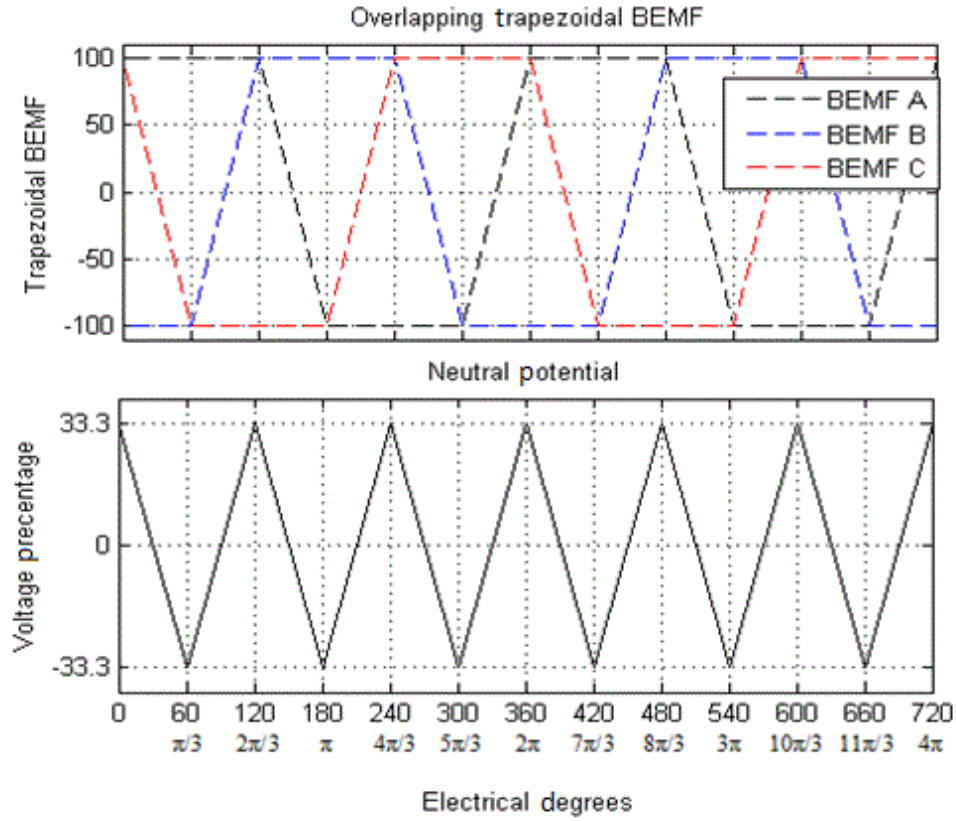
Figure 4.5 BLDC motor neutral point potential [4]

Figure 4.5 thus demonstrates that the potential between V_n and V_0 (V_{n0}) is crucial to the BLDCHM and inverter model. Whilst equation (4.22) holds true, a model of the BLDC machine requires the phase currents to be relative to the voltage supplied by the inverter. To accomplish this, equation (4.10) is expanded into equation (4.23).

$$\begin{bmatrix} V_{a0} - V_{n0} \\ V_{b0} - V_{n0} \\ V_{c0} - V_{n0} \end{bmatrix} = \begin{bmatrix} R & 0 & 0 \\ 0 & R & 0 \\ 0 & 0 & R \end{bmatrix} \begin{bmatrix} I_a \\ I_b \\ I_c \end{bmatrix} + \frac{d}{dt} \begin{bmatrix} L-M & 0 & 0 \\ 0 & L-M & 0 \\ 0 & 0 & L-M \end{bmatrix} \begin{bmatrix} I_a \\ I_b \\ I_c \end{bmatrix} + \begin{bmatrix} E_a \\ E_b \\ E_c \end{bmatrix} \qquad (4.23)$$

Where V_{a0}, V_{b0}, V_{c0} are the voltages imposed onto each respective phase by the inverter, relative to V_0. V_{n0} is the voltage difference between the V_{n0} and V_0.

To determine the potential of V_{n0} at any point in time, all terms of equation (4.23) are added.

$$V_{a0} + V_{b0} + V_{c0} - 3V_{n0} = R(I_a + I_b + I_c) + 3(L - M)\frac{d}{dt}(I_a + I_b + I_c) + (E_a + E_b + E_c) \quad (4.24)$$

Because of the floating neutral point inside the motor, the three motor currents must add up to zero.

$$I_a + I_b + I_c = 0 = \frac{d}{dt}(I_a + I_b + I_c) \tag{4.25}$$

This simplifies the summation of equation (4.23) to:

$$V_{a0} + V_{b0} + V_{c0} - 3V_{n0} = E_a + E_b + E_c \tag{4.26}$$

thus:

$$V_{n0} = \frac{(E_a + E_b + E_c) - (V_{a0} + V_{b0} + V_{c0})}{-3}$$

$$V_{n0} = \frac{1}{3}(V_{a0} + V_{b0} + V_{c0} - E_a - E_b - E_c) \tag{4.27}$$

The phase-voltage potentials from equation (4.23) are repeated below, and can be simulated because V_{n0} can be calculated from equation (4.27).

$$\begin{bmatrix} V_a \\ V_b \\ V_c \end{bmatrix} = \begin{bmatrix} V_{a0} - V_{n0} \\ V_{b0} - V_{n0} \\ V_{c0} - V_{n0} \end{bmatrix} \tag{4.28}$$

4.4 **Summary**

In this chapter the equivalent electrical circuit for the BLDC motor is used to derive the state space equations, with the presumption that the back EMF is perfectly trapezoidal, thus allowing it to be described as a piecewise linear function dependent on position and rotational speed. The inverter is modeled under the assumption of six ideal switches, and an expression for the neutral point potential is derived. This allows for the simulation of the BLDCHM and inverter, which follows in Chapter 5.

Chapter 5   -   BLDCHM Simulation and Controller Design

5.1   **Introduction**

In Chapter 4, the state space equations (SSEs) for the electrical and mechanical operation of a three-phase brushless DC hub motor (BLDCHM) are derived. This chapter makes use of VisSim v6.0, an embedded control developer from Texas Instruments® (TI), to simulate the BLDCHM based on the models in Chapter 4. Control loops for the BLDCHM are then designed and implemented on the TI F2812 DSP. VisSim is also the programming tool for the DSP and acts as an interface between the user and the DSP during testing, allowing data logging, capturing and adjustment of controller inputs.

5.2   **Motor parameter identification**

To simulate the BDCHM, the following motor parameters are required for the state space model:

- the phase resistances R_a, R_b, R_c (Ohms).

- the phase self inductances L_a, L_b, L_c (milli Henry).

- the mutual inductance between phases L_{ab}, L_{ac}, L_{bc} (milli Henry).

- the piecewise linear functions for the instantaneous back EMFs E_a, E_b, E_c (volts).

- the motor speed constant K_v (rad/V.s).

- the rotor inertia J (kg.m^2).

- number of pole pairs (no unit).

The state variables in the motor model are:

- the instantaneous phase currents I_a, I_b, I_c (amps) .

- the instantaneous mechanical rotor position θ_m (rad).

- the instantaneous mechanical rotational velocity ω_m (rad/sec).

The input variables are:

- the instantaneous phase voltage with respect to the zero reference potential V_{a0}, V_{b0}, V_{c0} (volts).

- the instantaneous external load torque T_l (N-m).

The motor parameter testing is documented in Appendix A. Despite the manufacturer stipulating that the BLDCHM has a trapezoidal back EMF, it is noted that the measured back EMFs are not ideal trapezoidal waves as assumed in the mathematical derivation in Chapter 4. The back EMF has rounded corners and thus has sinusoidal-like characteristics so to more accurately simulate the BLDCHM, a weighted average between the ideal trapezoidal and sinusoidal waveforms is calculated and used in the simulation. Equation (5.1) shows the calculation of the simulated back EMF waves.

$$E = 0.75 * E_{Trapezoidal} + 0.25 * E_{Sinusoidal}$$

$$(5.1)$$

Figure 5.1 below shows the difference between the measured back EMF waveforms and ideal trapezoidal and sinusoidal waveforms. It then shows that the weighted average waveforms represent the measured back EMF more accurately. This concept is proposed by the author, as all reference documentation for the theory of a BLDCHM is based on an ideal trapezoidal BEMF.
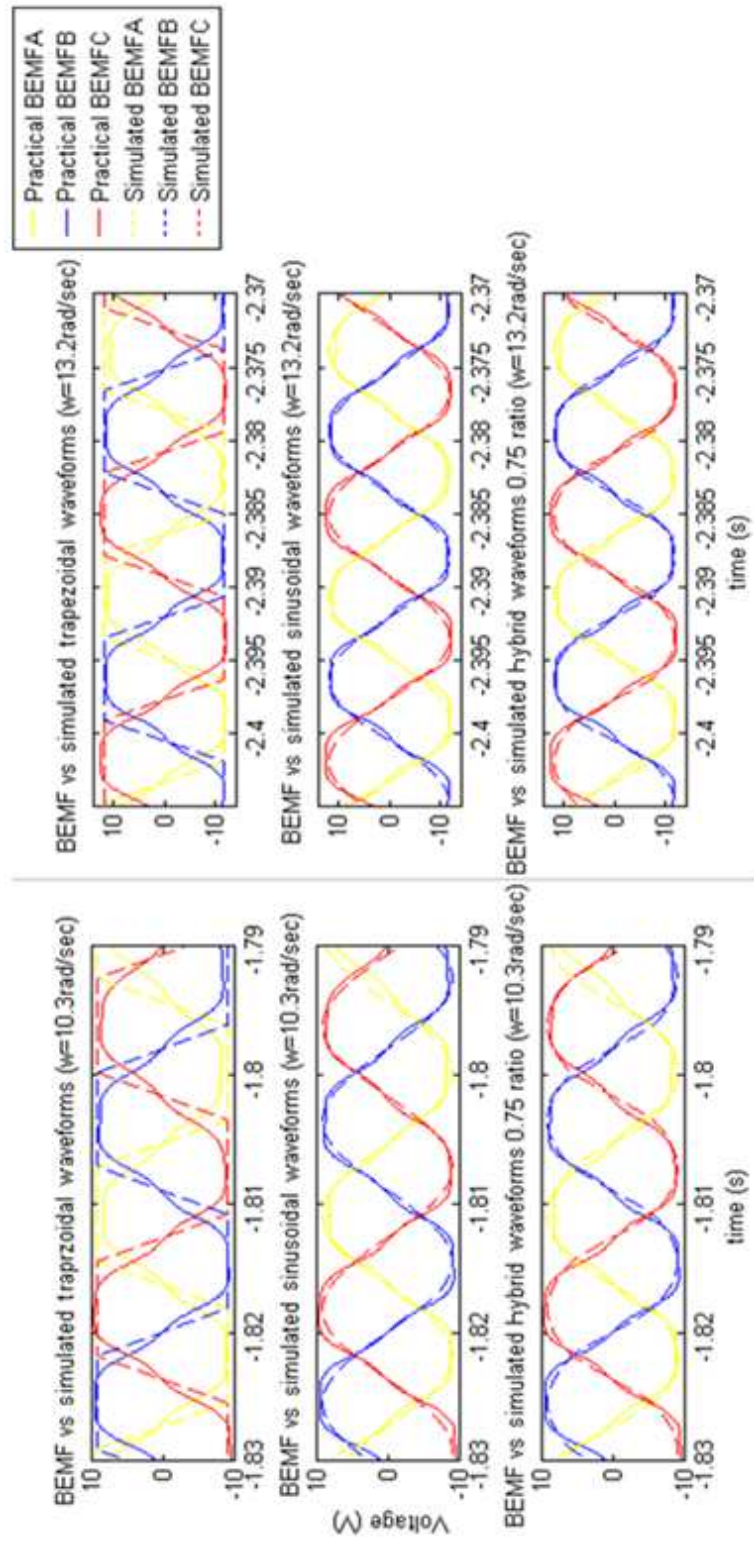
Figure 5.1 Back EMF waveform estimation

5.3   **Simulation of a BLDCHM under 120-degree commutation principle**

The state space equation derived in Chapter 4, provides a continuous mathematical model for the BLDCHM. However when operating with 120 degree commutation periods (explained in Chapter 3), one of the motor phases is disconnected from the supply-rails at any point in time (referred to as the floating phase and documented in section 3.3.3. This makes the simulation more complex than the state space equation.

When a motor phase is floating, it has the following characteristics:

- the phase current of the floating phase is equal to zero, and the currents in the two conducting phases are equal in magnitude, but opposite in direction.

- The floating phase voltage is equal to the neutral point potential as no current flows in this floating phase.

To take into account the characteristics of a floating phase in a BLDCHM, controlled by a 120-degree commutation principle, a six-step commutation matrix is developed in the simulation, based on the instantaneous electrical position. This matrix is used to control the currents and voltages in the two conducting phase. The model for the 120-degree commutation strategy appears in Figure 5.2 below.

During rotation, the floating phase current is zero and this is achieved in the simulation by resetting the current integrator for that phase. This integrator reset is physically implemented with fly-back diodes in the inverter, which allow the floating phase inductance to discharge.

Figure 5.2 below shows the VisSim simulation of the BLDCHM state space equation developed in Chapter 4. The simulated shaft load is a constant torque load which is set by means of a slide bar, but can also be implemented by means of a function block. The simulation makes use of a plot window which is configured to display various simulated waveforms compared to experimental data from the BLDCHM. The experimental data is sampled by the DSP and imported by VisSim. Section 5.3.1 displays simulated results and practical data for a series of experiments.
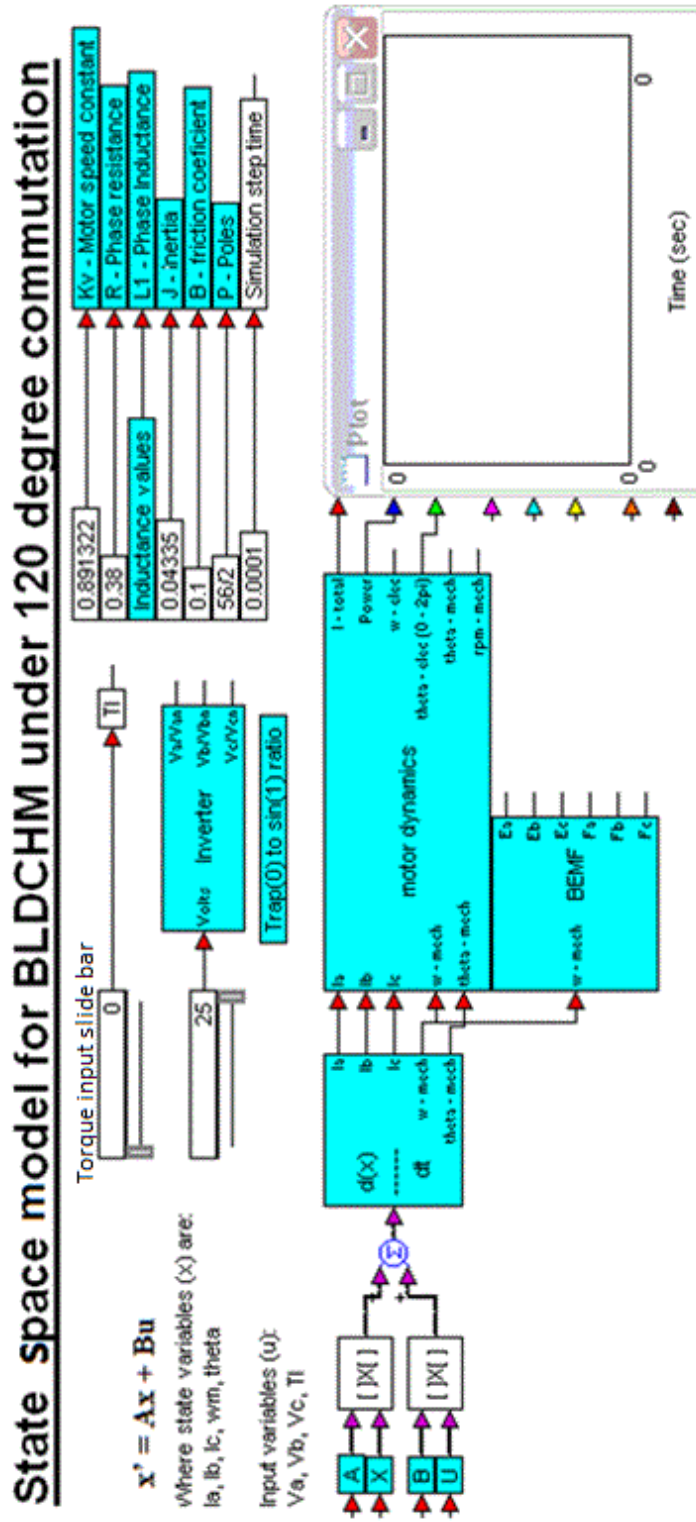
Figure 5.2 VisSim model of a BLDCHM with 120-degree commutation strategy

5.3.1   Comparison of simulated and practical results

The theme of this thesis is motion control with particular reference to torque control. A BLDCHM output torque is proportional to the current in the motor phases. For the simulation to model the BLDCHM phase currents, the motor and inverter phase voltages are required. The following measured data is recorded, and is based on a 120-degree commutation principle:

- The instantaneous phase voltages supplied by the inverter, referenced to the inverter zero potential (V_{ao}, V_{bo}, V_{co}).

- The instantaneous potential between the BLDCHM neutral point and the inverter zero potential (V_{no}).

- The subsequent instantaneous phase voltages with respect to the neutral point (V_{an}, V_{bn}, V_{cn}).

- The instantaneous current (I_t) supplied from the inverter to the BLDCHM which is equal to the sum of the absolute value of the individual phase currents.

5.3.1.1   Inverter output phase voltages

Each phase winding of the stator is connected by the inverter to either $+Vcc$, $-Vcc$ or allowed to float as described in Chapter 3. The simulated and practical results of the three phases when the motor shaft is rotating freely under no load are shown in Figure 5.3, Figure 5.4 and Figure 5.5, with the simulation results closely resembling the practical result.
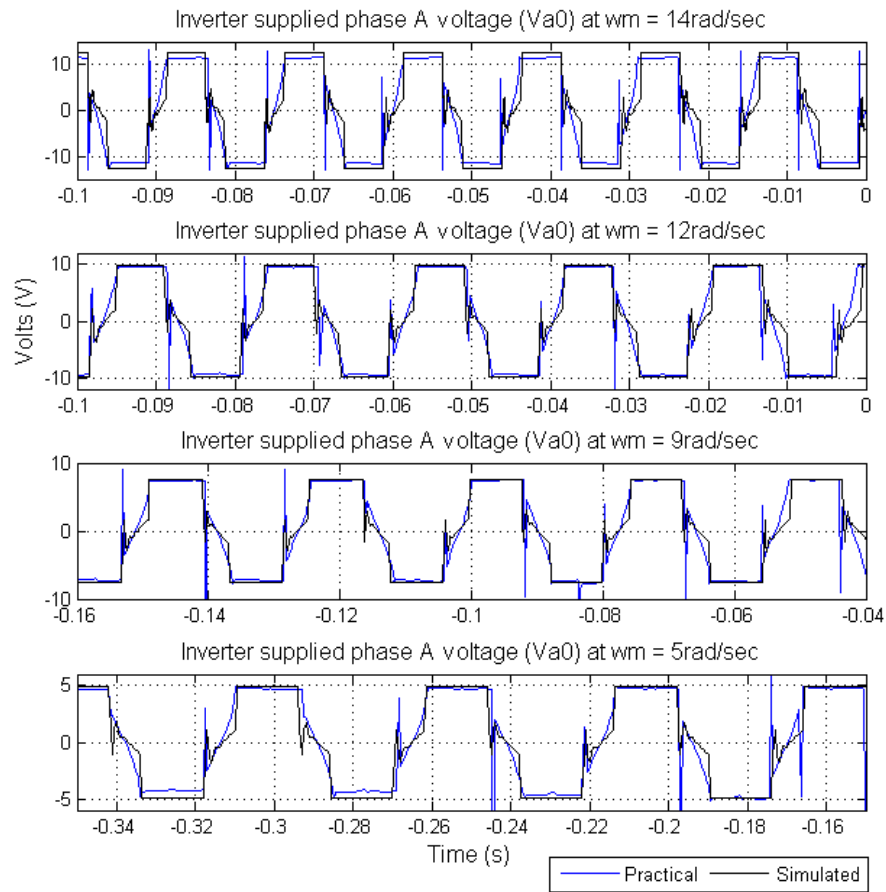
Figure 5.3 Inverter supplied phase A voltages (V_{a0})
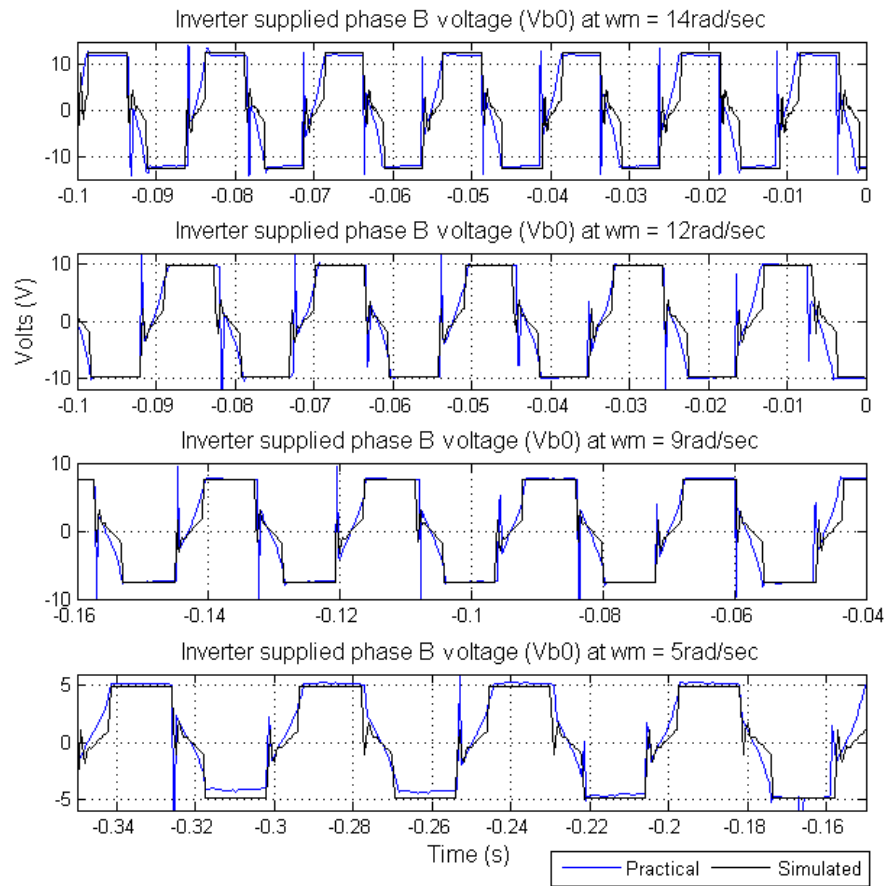
Figure 5.4 Inverter supplied phase B voltages (V_{b0})
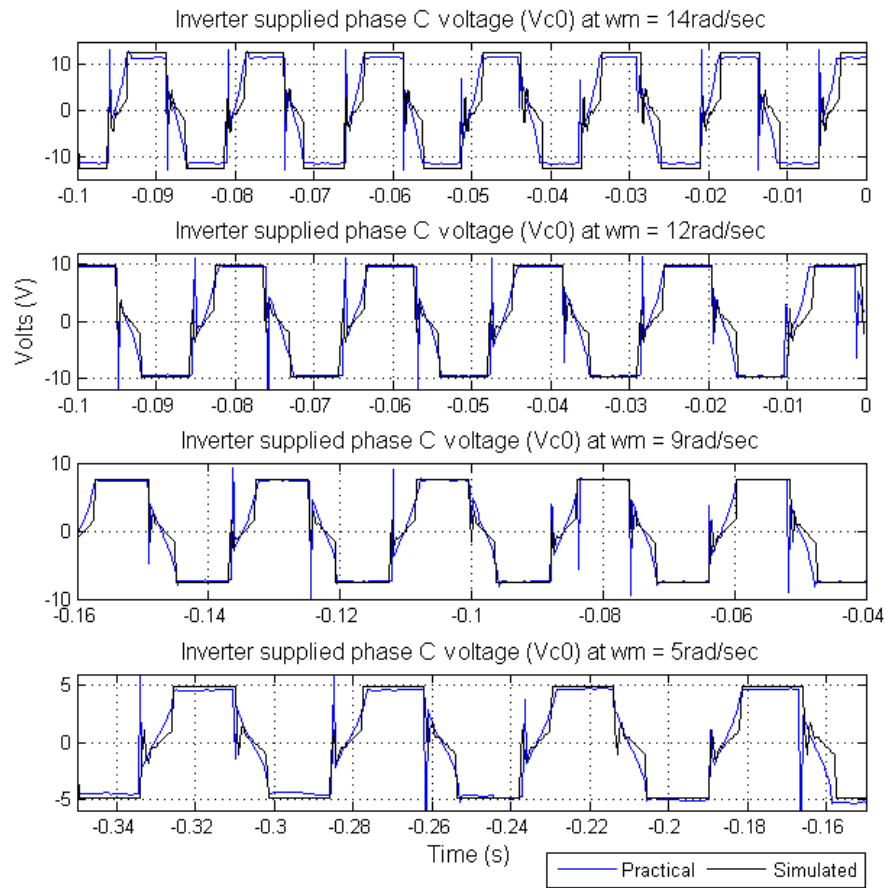
Figure 5.5 Inverter supplied phase C voltages (V_{c0})

5.3.1.2   Neutral point potential

The neutral point potential (V_n) within the motor is not equal to the inverter reference point (V_0), as shown in Figure 5.6. The potential (V_{no}) between the neutral point and the inverter reference point is required to accurately simulate the BLDCHM phase currents.

Figure 5.7 shows the simulated results compared to the practical results for V_{n0} and the noise spikes occur when a phase goes into a floating state by being disconnected from the inverter's supply rails. These spikes are clearly seen and accurately simulated.
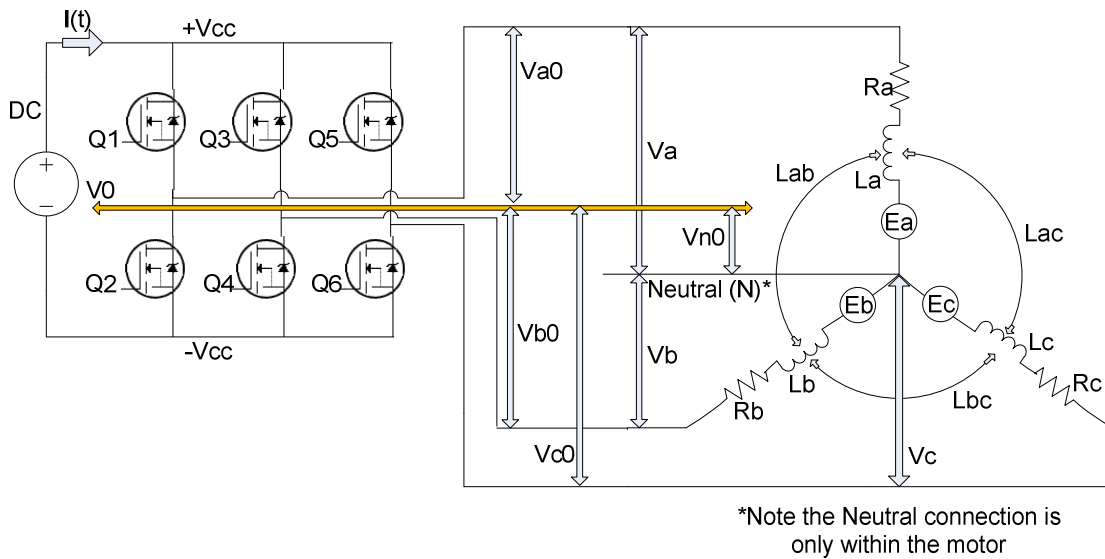
Figure 5.6 Voltage potential difference between the inverter reference and the BLDCHM neutral [4]
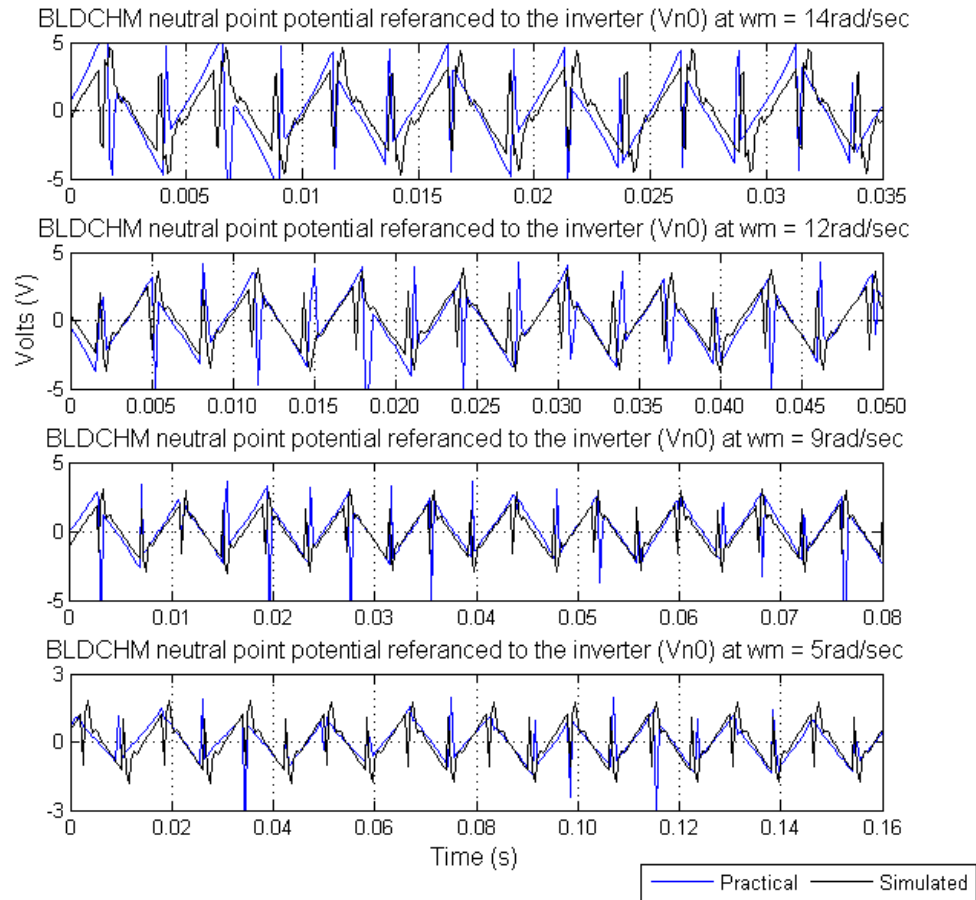
Figure 5.7 Stator neutral point potential difference with respect to the inverter reference point (V_{n0})

5.3.1.3   Phase potentials with respect to the BLDCHM neutral point

The current flowing through each phase depends on the voltage across the respective phase. This voltage is the difference between the inverter-supplied-voltage and the BLDCHM neutral point voltage. Hence

$$\begin{bmatrix} V_{an} \\ V_{bn} \\ V_{cn} \end{bmatrix} = \begin{bmatrix} V_{a0} - V_{n0} \\ V_{b0} - V_{n0} \\ V_{c0} - V_{n0} \end{bmatrix} \tag{5.2}$$

Equation (5.2) is derived in Chapter 4 and is used to simulate the phase voltages taking into account the 120-degree commutation strategy. The simulated results are compared to practical waveforms below.
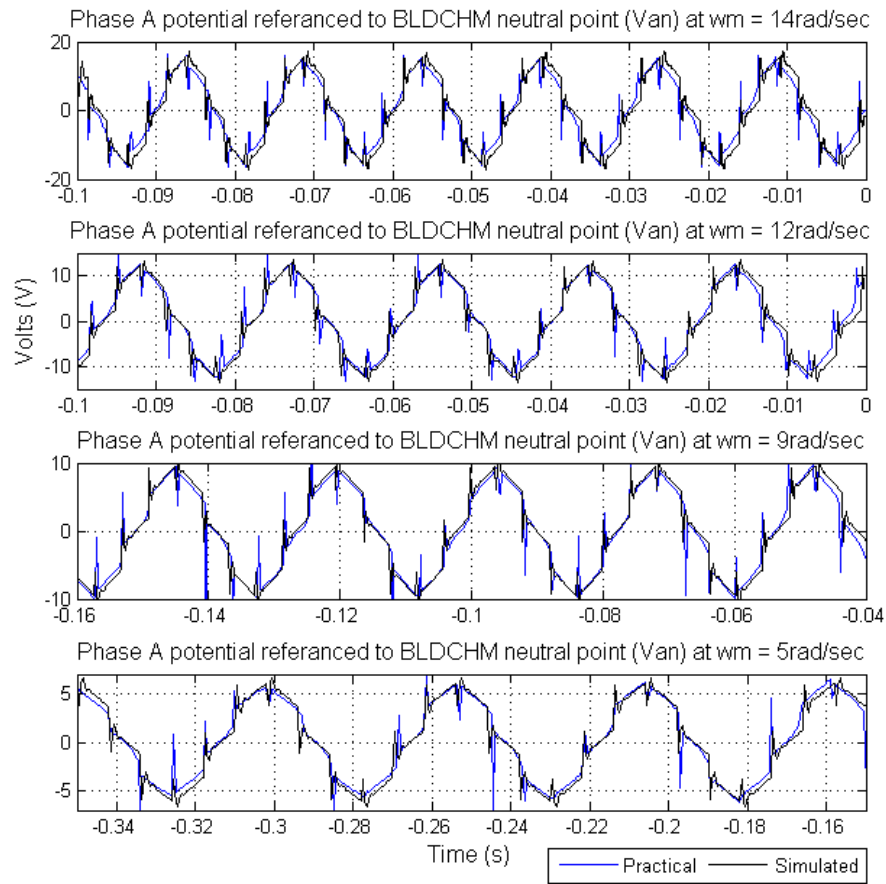
Figure 5.8 Phase A potential (V_{an})
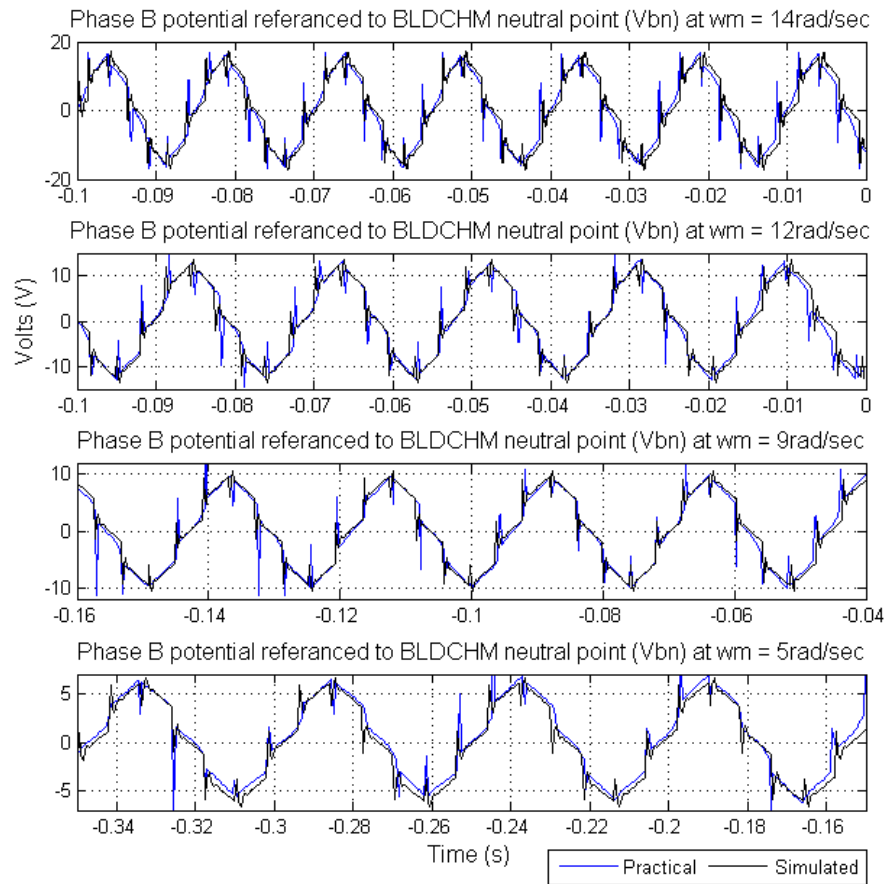
Figure 5.9 Phase B potential (V_{bn})
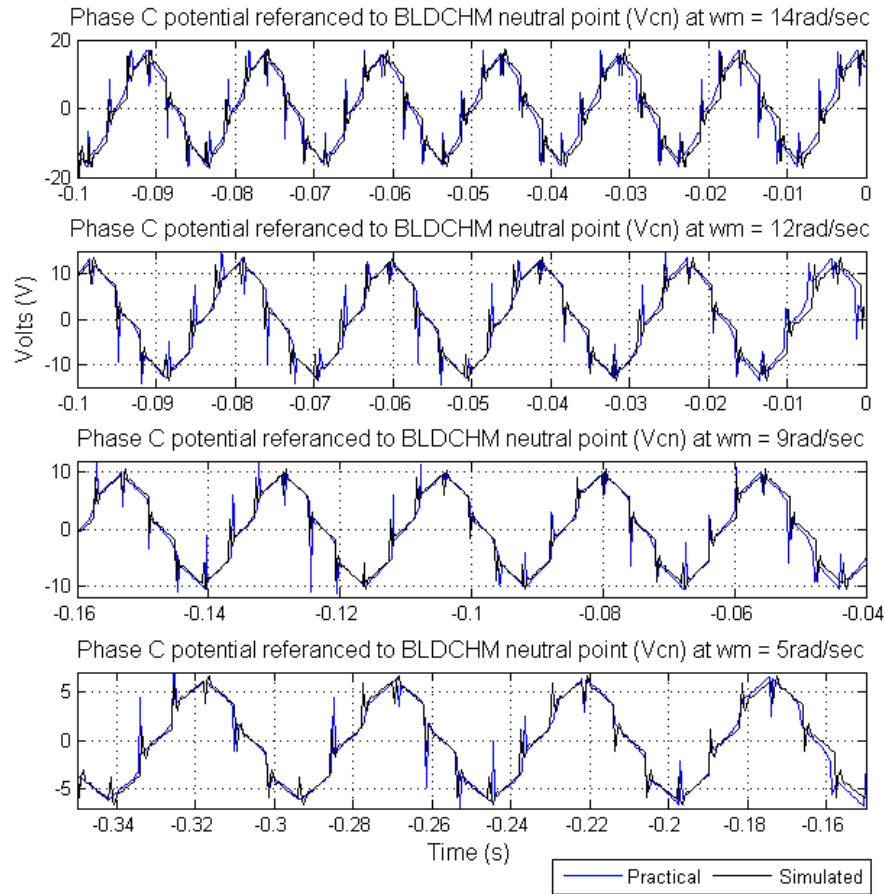
Figure 5.10 Phase C potential (V_{cn})

5.3.1.4   BLDCHM current

The theme of this thesis is torque control. In a BLDCHM the output torque is proportional to the current by a factor K_t, known as the torque constant. Controlling the current therefore controls the torque.

Figure 5.11 shows the accuracy with which the BLDCHM current is simulated, comparing the simulated and practical waveforms at various values of constant speed and under no load.

In order to compare the simulated values of current, speed and torque to the practical results, a ramp down load test is performed using the test rig described in Appendix A. Figure 5.12 and Figure 5.13 show the accuracy of the BLDCHM simulation over the entire speed range. During testing the BLDCHM is supplied with rated DC voltage and no closed loop control for current or speed is implemented. The induction machine (IM) acts as a generator and thus as a load to the

BLDCHM. The IM is operated in vector control mode by a Siemens drive which increases its loading of the BLDCHM in order to follow the required speed ramp-down programmed into the Siemens drive. Initially the BLDCHM torque is approximately zero as the induction generator is not yet applying a load. As the induction generator speed is ramped down (shown in Figure 5.12), effectively applying an increasing load, the values for the BLDCHM current, torque and speed are monitored and compared to the simulated results (shown in Figure 5.13). For the simulation the T_l of BLDCHM input variable is programmed to ramp up from zero to a maximum value over the same time interval as the practical IM ramp-down test. In both the simulation and in the measured results current spikes appear throughout the speed range. These current spikes occur when one phase is switched off, and another is switched on. In the phase which is being switched on, the impedance due to the phase inductance causes the current dip momentarily. The discrepancies between the results shown in Figure 5.12 and Figure 5.13, are because the practical system is loaded by the induction generator which follows a speed profile due to its inability to provide a linear load profile as simulated. Despite this, the results indicate that the model for the BLDCHM is accurate.
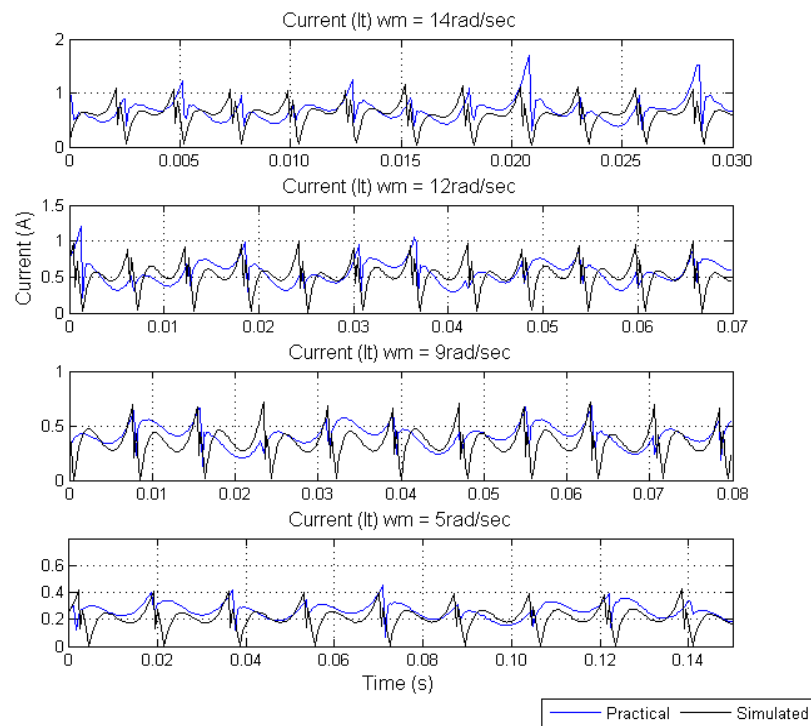
Figure 5.11 Current (I_t) from the DC source in Figure 5.6
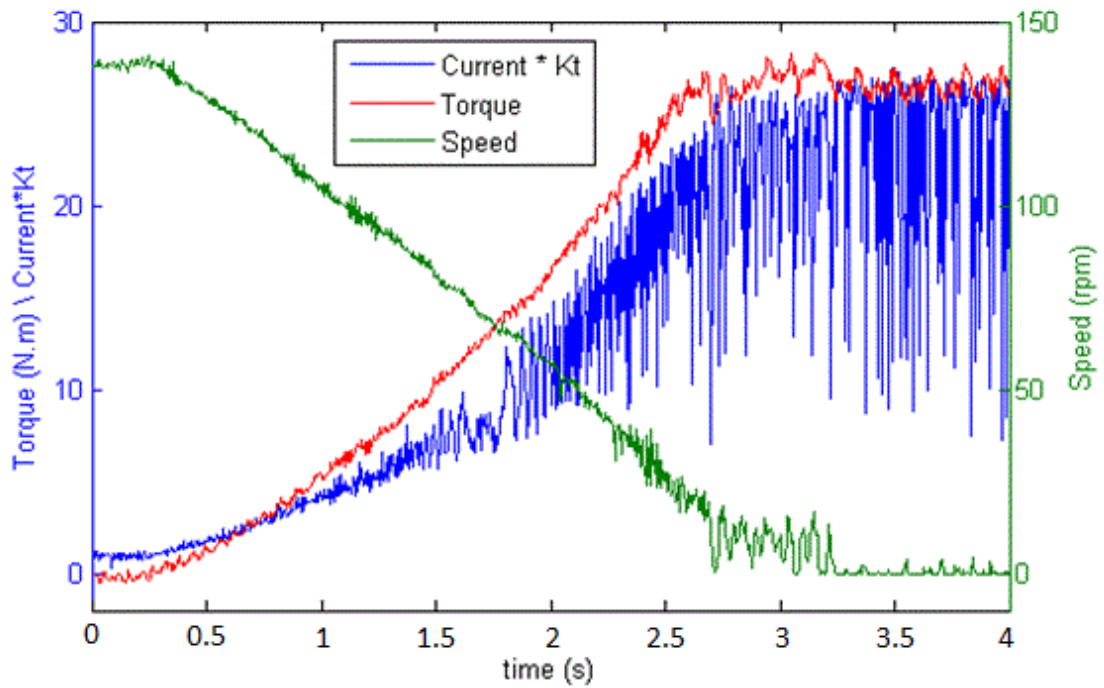
Figure 5.12 Practical results of torque, speed and current during run down load test
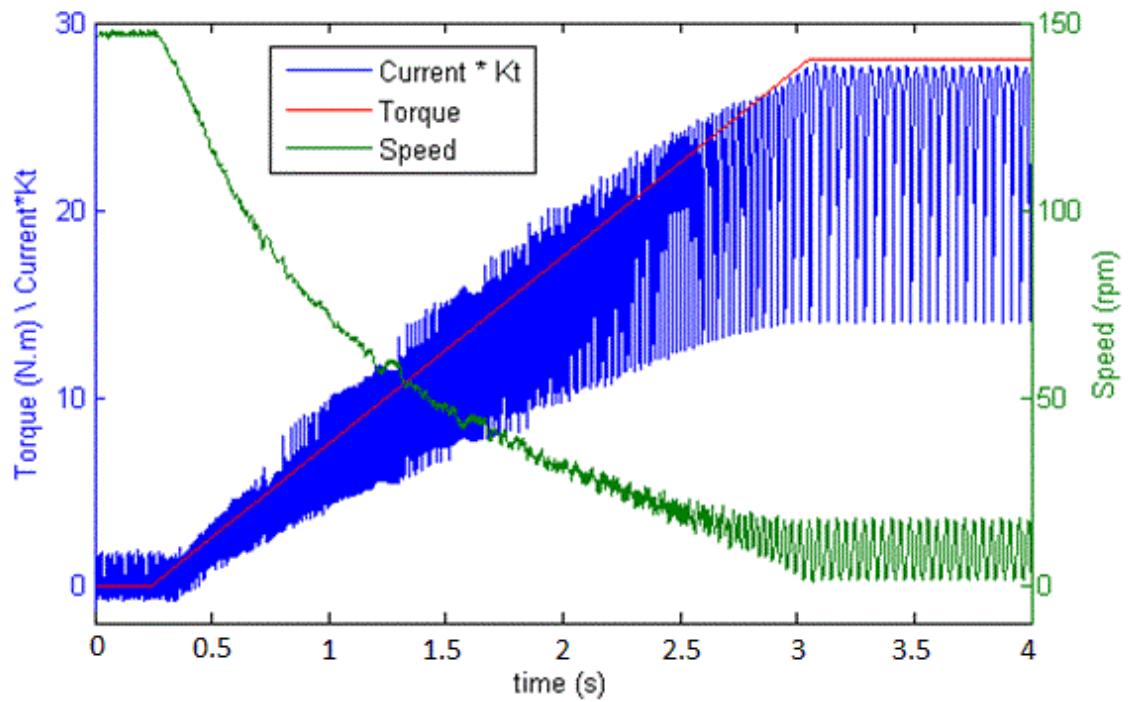
Figure 5.13 Simulated results of torque, speed and current during run down load test

5.4   **Torque controller design**

To achieve torque control in the BLDCHM, a proportional and integral controller (PI controller) is
designed and implemented for the motor current control loop, as shown in Figure 5.14 where:

- I_{ref} is the reference value of the current.

- e_i is the instantaneous error between the reference and current feedback from the motor.

- $Gc(s)$ is the transfer function for the PI controller.

- $Gi(s)$ is the transfer function for the position-dependent inverter.

- $Gp(s)$ is the transfer function for the plant, which is the BLDCHM.
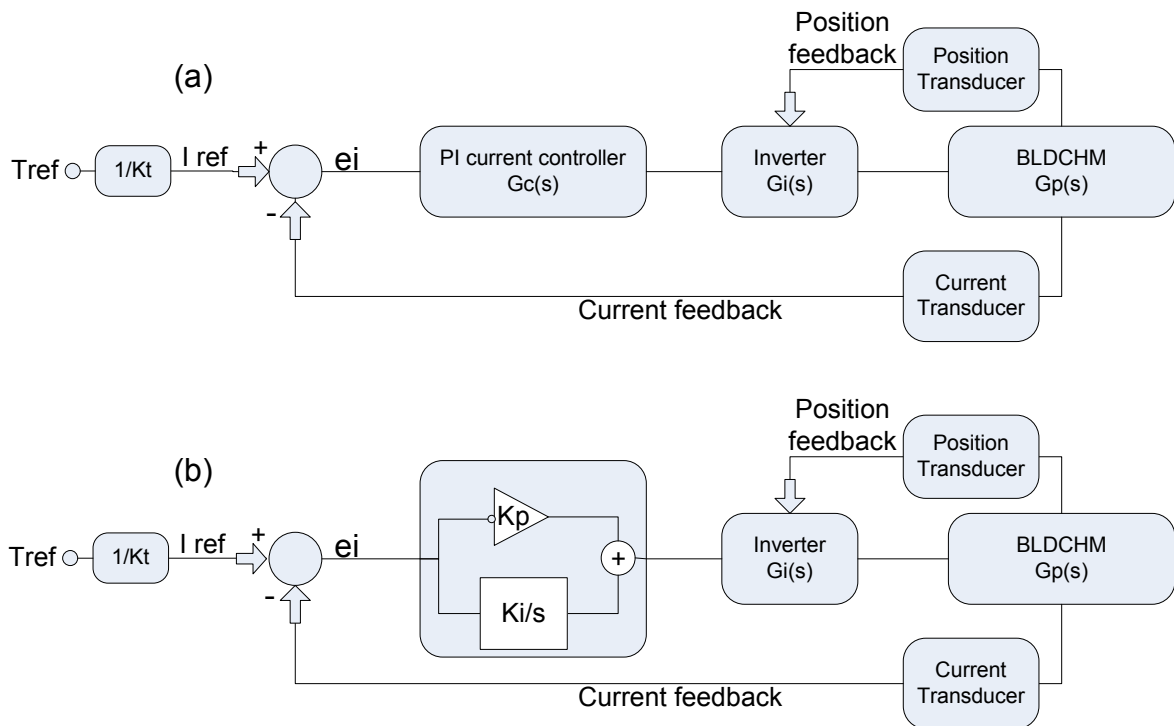
Figure 5.14 Torque controller configuration [32]

5.4.1   Torque Controller transfer function

In order to accurately control the output torque, the mathematical model for each of the blocks in
Figure 5.14 (a) are required. The values for the proportional and integral gains (K_p and K_i
respectively) are then evaluated. The processing of the feedback signals for the BLDCHM position,
current and inverter control signals is documented in section 3.4 and section 3.5.

5.4.1.1   BLDCHM transfer function

In Chapter 4 the SSE for the BLDCHM is determined in the time domain. Section 5.3 shows the simulation of the BLDCHM which is to be controlled. This section therefore does not strictly require another model for *Gp(s)* (from Figure 5.14), but an approximation is derived nonetheless.

From Chapter 4, equations (4.16) below represents the mechanical behavior for a BLDCHM, and are rearranged to have the derivative with respect to time as the subject of the formula.

$$J\left[\frac{d\omega_m}{dt}\right] + B_f\omega_m = T_e(t) - T_l(t) \tag{4.16}$$

$$J\left[\frac{d\omega_m}{dt}\right] = \frac{E*I}{\omega_m} - T_l(t) - B_f\omega_m$$

$$\frac{d\omega_m}{dt} = \frac{1}{J}\left[\frac{E*I}{\omega_m} - T_l - B_f*\omega_m\right] \tag{5.3}$$

Equation (4.11) below represents the electrical behavior for a BLDCHM, developed in Chapter 4 in the ABC reference frame. The three phase BLDCHM is assumed to be balanced and is now analyzed further on a per-phase basis. The per-phase derivation is found as follows:

$$\frac{d}{dt}\begin{bmatrix}I_a\\I_b\\I_c\end{bmatrix} = \frac{\begin{bmatrix}V_a\\V_b\\V_c\end{bmatrix} - \begin{bmatrix}R&0&0\\0&R&0\\0&0&R\end{bmatrix}\begin{bmatrix}I_a\\I_b\\I_c\end{bmatrix} - \begin{bmatrix}E_a\\E_b\\E_c\end{bmatrix}}{L-M} \tag{4.11}$$

$$\frac{d}{dt}I = \frac{V - RI - E}{L}$$

$$\frac{d}{dt}I = \frac{V - RI - K_v*\omega_m}{L}$$

$$\frac{dI}{dt} = \frac{V}{L} - \frac{R*I}{L} - \frac{K_v*\omega_m}{L} \tag{5.4}$$

where:

- V is the DC supply voltage (V).

- ω_m is the instantaneous motor rotational speed (mechanical rad/sec).

- J is the motor inertia (kg.m^2).

- E is the instantaneous back EMF (V).

- I is the instantaneous current (amps).

- B_f is the friction coefficient (N-m per radian per second).

- T_l is the instantaneous load torque (N-m).

- K_v is the motor speed constant (V.s/rad).

- L is the motor inductance (henry).

- R is the motor resistance (ohm).

Placing equations (5.3) and (5.4) into a single equation results in:

$$\frac{d}{dt}\begin{bmatrix} I \\ \omega_m \end{bmatrix} = \begin{bmatrix} -R/L & -Kv/L \\ K_v/J & -B/J \end{bmatrix}\begin{bmatrix} I \\ \omega_m \end{bmatrix} + \begin{bmatrix} 1/L & 0 \\ 0 & -1/J \end{bmatrix}\begin{bmatrix} V \\ T_l \end{bmatrix} \qquad (5.5)$$

In order to obtain the transfer functions, a Matlab® script is used [39]. The coding script is shown in Appendix B and uses Matlab's "statespace to transfer function" (ss2tf) which determines the transfer functions below:

- tf $\left(\frac{I}{V}\right)$ - current response to the motor supply voltage.

- tf $\left(\frac{\omega_m}{V}\right)$ - speed response to the motor supply voltage.

- tf $\left(\frac{I}{T_l}\right)$ - current response to the load torque.

- tf $\left(\frac{\omega_m}{T_l}\right)$ - speed response to the load torque.

Because the focus of this thesis is torque control, and the only input variable which can be controlled by the user is the motor supply voltage, the step-response for the tf $\left(\frac{I}{V}\right)$ and the simulated model are compared and shown in Figure 5.15 for a voltage step input of 20 V. The simulated waveform shows the current transients for a step input of 20V (over two motor phases in Figure 5.6) and 120 degree commutation strategy as described in section 5.3.1.4. The transfer

function waveform however, is a smooth curve because it is purely the output response to a step input and does not take into account the 120 degree commutation by the inverter.

$$Gp(s) = tf\left(\frac{I}{V}\right) = \frac{220\,s\ +\ 384.5}{s^2\ +\ 301.2\,s\ +\ 10761} \qquad (5.6\,)$$
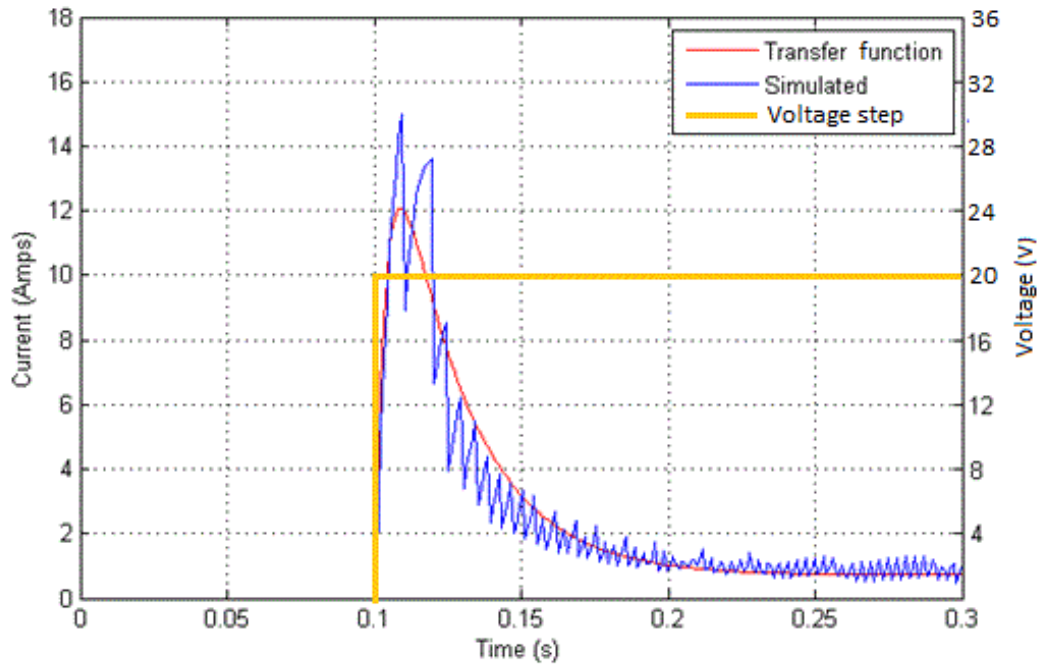
Figure 5.15 BLDCHM simulation vs transfer function response to a 20 V step input

5.4.1.2 Inverter transfer function

The inverter (with transfer function *Gi(s)* in Figure 5.14) is considered to be an ideal source. This implies that the rail voltage is constant and invariant, with the capability of providing any current which the BLDCHM requires. The MOSFETs within the inverter are considered to be ideal switches and thus have zero resistance and transient times. Under these conditions the inverter will have no effect on the control configuration in Figure 5.14, and thus:

$$Gi(s) = \ 1 \qquad (5.7\,)$$

5.4.1.3   PI controller transfer function

The PI controller in Figure 5.14 (b) is comprised of two elements into which the error e_i between the reference current and the BLDCHM actual current is applied. The contribution from the proportional gain of the controller is a fast response. However, the disadvantage of the proportional gain occurs when the motor current is equal to the reference, in which case the proportional output is zero, effectively turning off the inverter. This is the inherent disadvantage of a stand-alone proportional controller.

When integrating the error signal, the typical response time is greater than that of a proportional controller. However once the actual current equals the reference value, the integrator will continue to output the necessary value in order to maintain a zero-steady-state error.

A combination of the proportional and integral gains into a single controller thus utilizes the advantages of both proportional and integral paths.
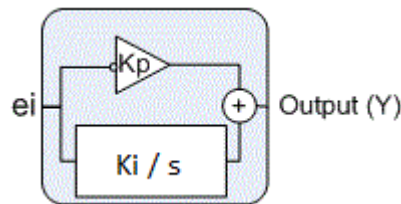
Figure 5.16 PI controller [32]

$$Gc(s) = \frac{Y}{e_i} = K_p + \frac{K_i}{s} = \frac{K_i\left(1 + \frac{K_p}{K_i}s\right)}{s} \tag{5.8}$$

5.4.1.4   PI controller testing

The test rig described in Appendix A is used to evaluate the controller response. The IM is run as a generator in vector-speed-control mode at 6 % speed to provide a test load for the BLDCHM. As the torque reference is stepped up, the BLDCHM attempts to accelerate, however the IM increases its load torque to maintain its speed set point. The torque control for the BLDCHM is implemented on a Texas Instruments development board (TMS 320F2812) and the reference is stepped using the graphical user interface (GUI) developed in VisSim programming software. The BLDCM current (*I(t)* in Figure 5.6) resulting from a five-step reference to the BLDCHM torque controller input, appears in Figure 5.17, with a zoomed-in view of each step shown in Figure 5.18 to Figure 5.22.

The waveforms represent the current supplied by the inverter to the BLDCHM, with a summary of each set of results documented in Table 5.1.
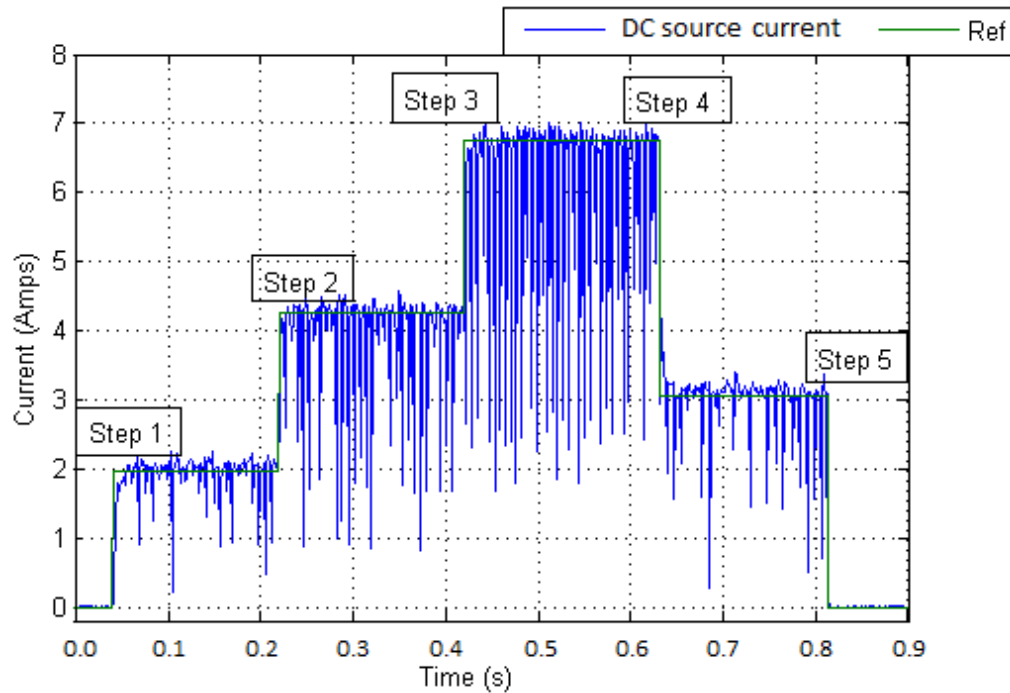
Figure 5.17 Response of the current controller to a five step change of the BLDCHM current reference
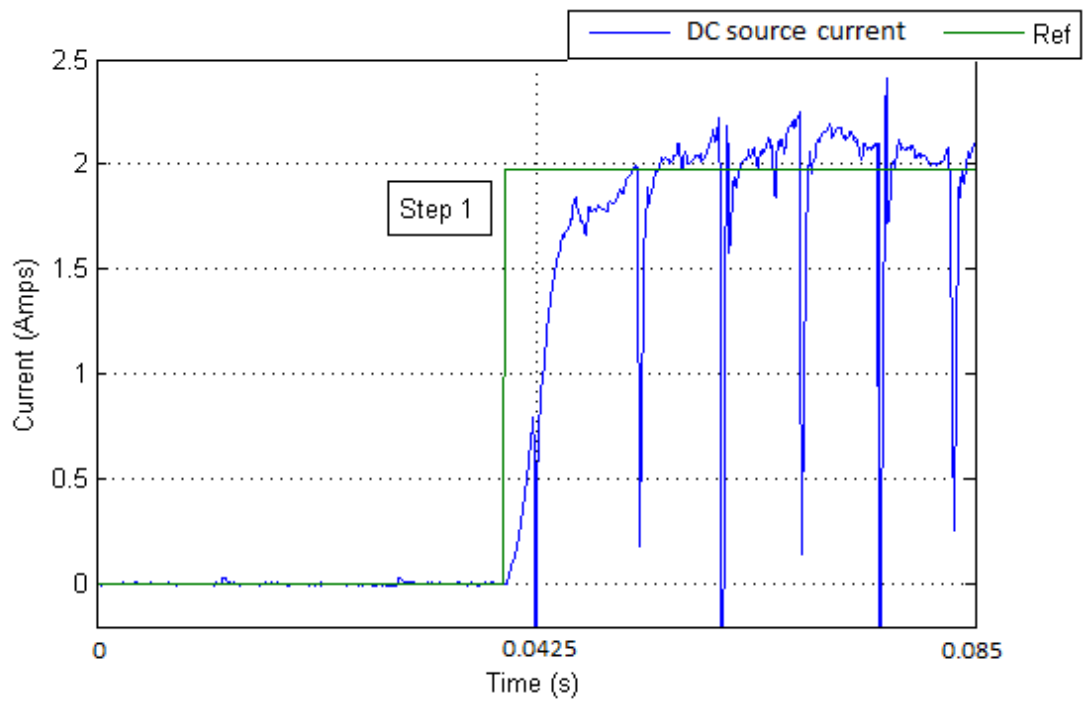
Figure 5.18 Zoomed-in view of step 1 response
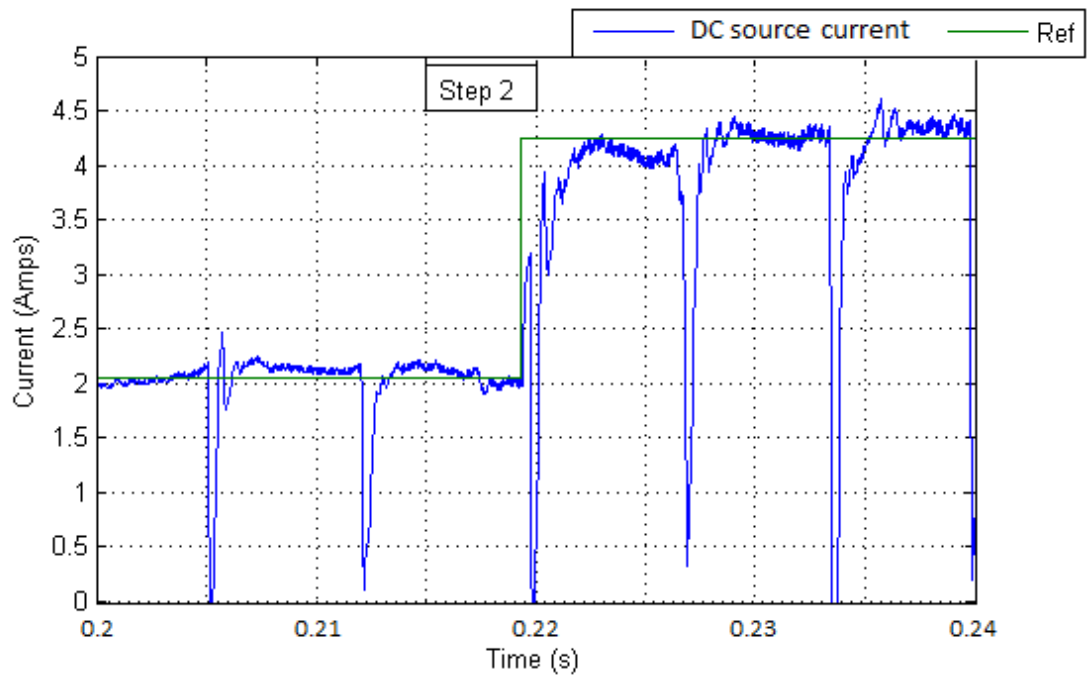
Figure 5.19 Zoomed-in view of step 2 response
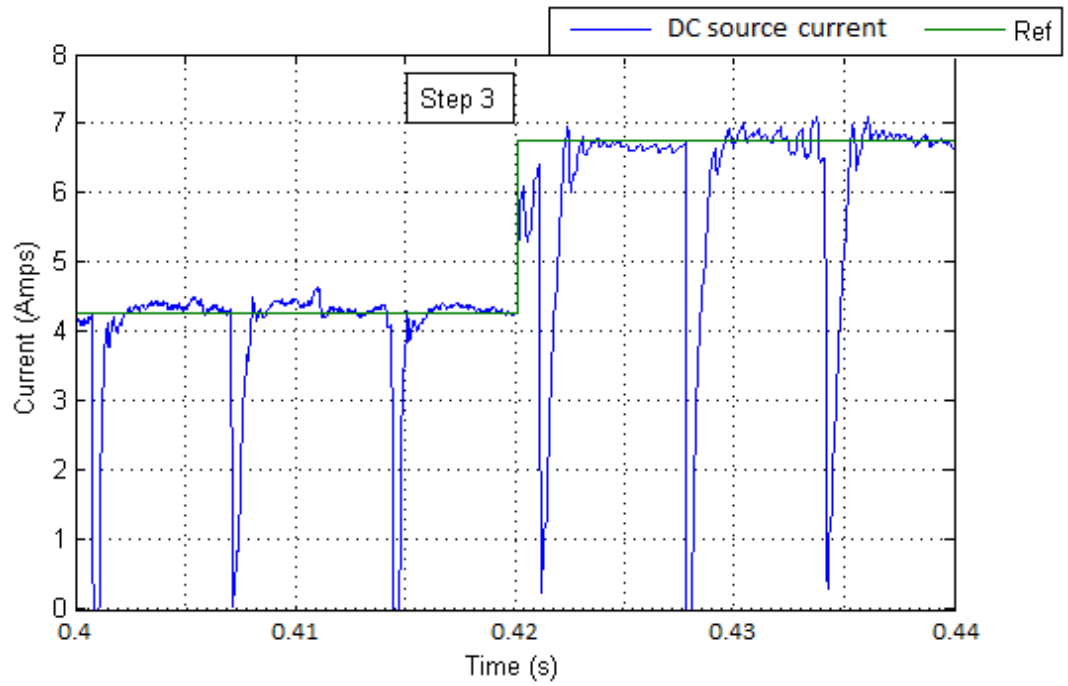
Figure 5.20 Zoomed-in view of step 3 response
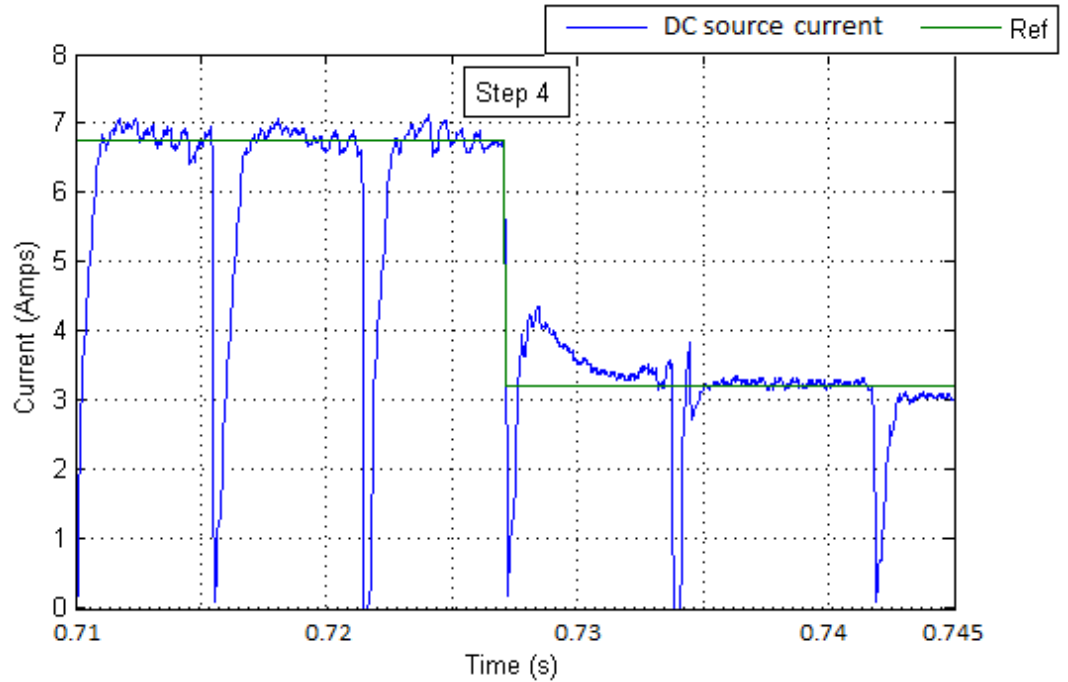
Figure 5.21 Zoomed-in view of step 4 response
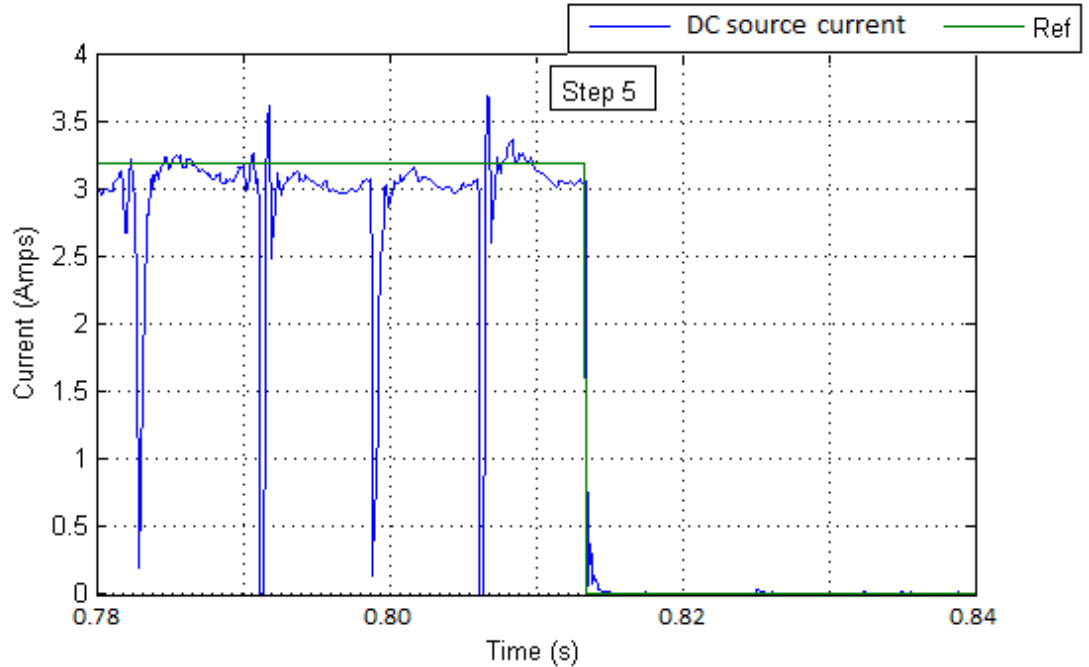
Figure 5.22 Zoomed-in view of step 5 response

In Figure 5.18 to Figure 5.22, the current repeatedly dips to zero amps. These dips are due to the commutation strategy switching from one phase to another and the phase inductance impeding current flow. The shape of the current waveforms is similar in both the practical and simulated currents shown in Figure 5.11 which has no current control. The important difference is that Figure 5.11 also has current spike toward the tail end of the phase commutation, which the current controller has removed in Figure 5.18 to Figure 5.22. Below is a summary of the five step current response.

Table 5.1 Summary of five step current response

Step 1	The DC source current takes 10 ms to reach the reference input. An overshoot of 10% is observed with a settling time of 25 ms, which is due to the response time of the IM increasing torque, in order to load the BLDCHM.
Step 2	The step response has a rise time of less than 5 ms and no overshoot.
Step 3	The step response has a rise time of less than 5 ms with no overshoot, however the current waveform at steady-state, has 5% oscillations (peak-to-peak). This is caused by a combination of the proportional gain and controller sampling time.
Step 4	The first step down of the reference shows no overshoot and a response time of 5 ms

Step 5	The current prior to step 5 shows typical integral action error due to the phase commutation. As the phase inductance limits the current after a commutation, the controller increases the voltage over the phase, which may cause current spikes. This can be compensated for by using feed forward control based on the inverter commutation pattern, however this is not investigated in this thesis. The current step to zero takes less than 2 ms. This quick response is due to the controller resetting the integrator when the reference equals zero.

5.4.2   BLDCHM regeneration

The current controller developed in section 5.4.1, provides an acceleration torque-control for both directions of rotation. Electric vehicle (EV) applications require both acceleration and deceleration. For deceleration, the generator properties of the BLDCHM are utilized [30]. Chapter 3 explains the implementation of regeneration.

During regeneration, only the bottom three MOSFETs of the inverter are utilized. To investigate different regeneration commutation-patterns, the test rig described in Appendix A is used. The BLDCHM receives a PWM ratio in generator mode and is connected via a torque transducer to the IM. The IM is operated under speed control mode by a Siemens drive. The following tests are performed with a constant inverter PWM mark-to-space-ratio of 0.25, 0.5, 0.75 and 1 respectively. At the start of the test, the IM speed is ramped down from the BLDCHM rated speed to standstill. The BLDCHM is in regeneration mode and the values for current, torque and speed are shown below for various regeneration strategies. The torque is negative because it is a deceleration torque. The current is negative because it flows from the BLDCHM to the batteries.

- 120-degree commutation: This is the minimum angle under which regeneration is implemented. For a three phase machine, a commutation strategy below 120 degrees will not efficiently utilize the fully 360 degree electrical rotation. Figure 5.23 shows the results for 120-degree commutation.
- 180 degree commutation: This provides a 60 degree overlap between phases during regeneration in order to investigate the effects of dynamic braking within the BLDCHM phases, on the deceleration torque. Figure 5.24 shows the results for 180-degree commutation

- 360 degree commutation: This commutation pattern allows all three phases to conduct at the same time. Regeneration still occurs due to the PWM switching. However, as the PWM get closer to a value of 1, the deceleration torque is no longer due to regeneration of energy returning to the batteries, but from dynamic braking within the BLDCHM phases. In this strategy the majority of energy is converted to heat. Figure 5.25 shows the results for 360-degree commutation.
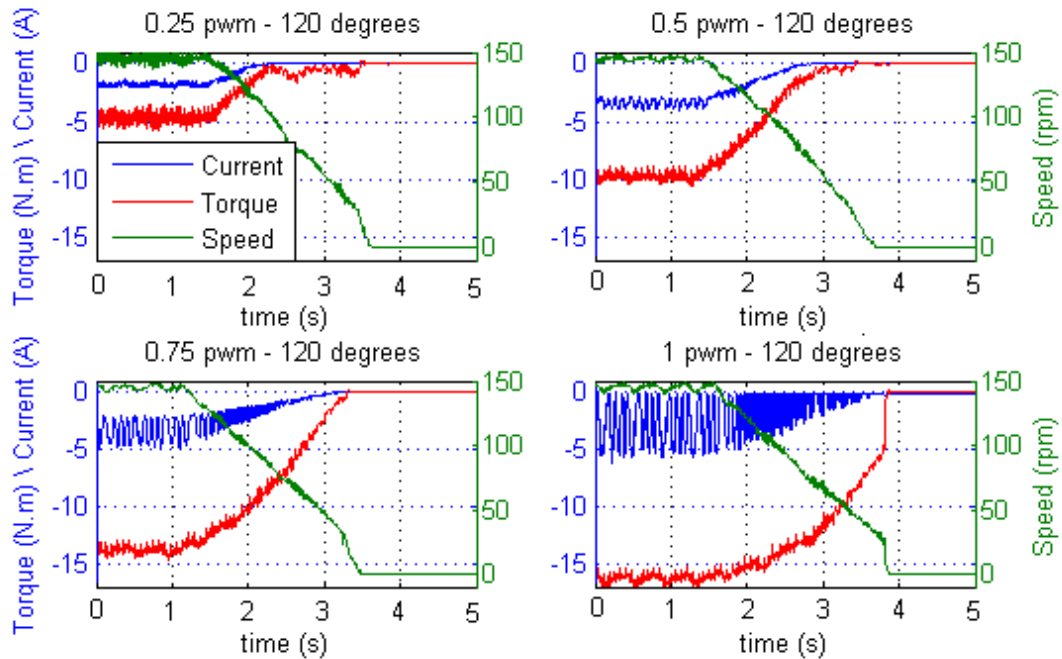
Figure 5.23 Regeneration properties with 120 electrical degree commutation
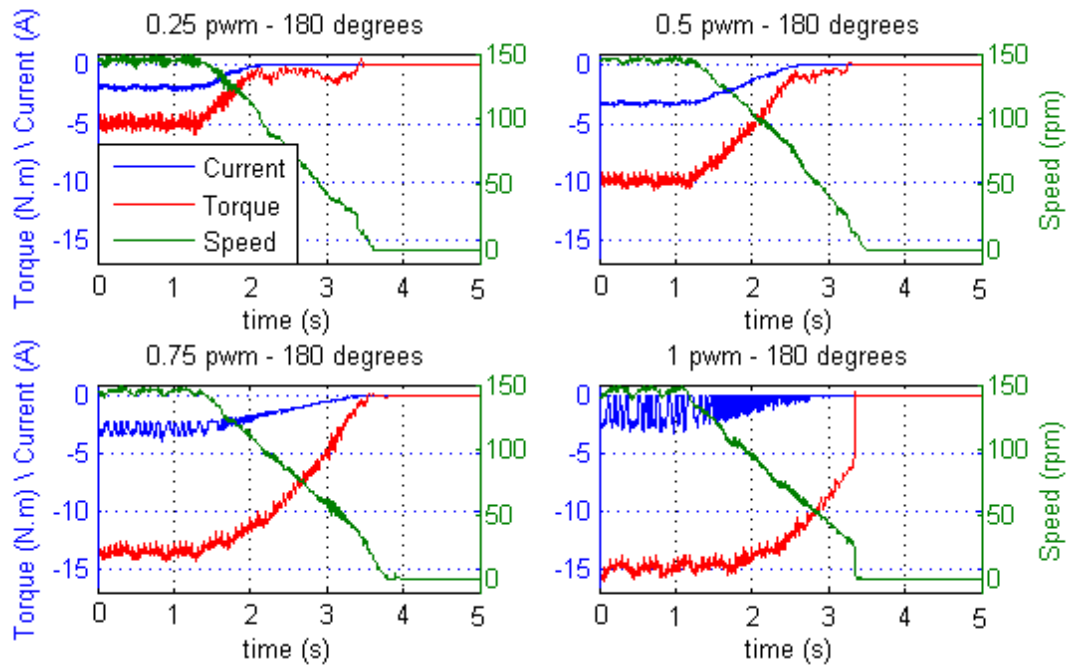
Figure 5.24 Regeneration properties with 180 electrical degree commutation
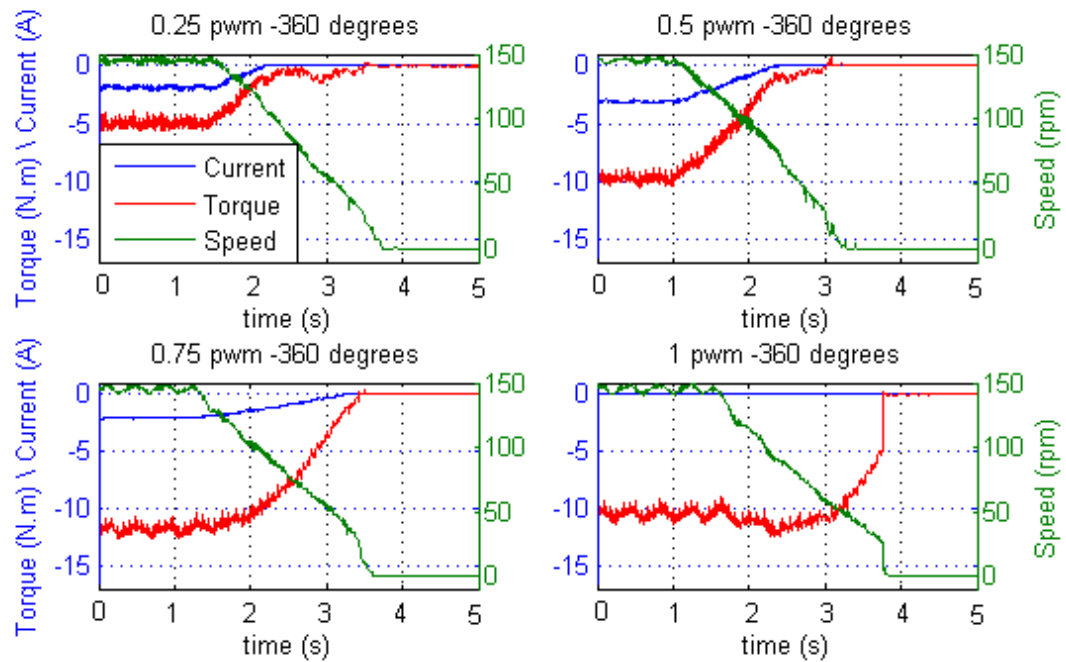
Figure 5.25 Regeneration properties with 360 electrical degree commutation

The desired commutation strategy for an EV must produce the highest ratio of regeneration current (current returning to the batteries from the EV motors in generator mode) to deceleration torque, but under control by the EV user. This allows for the user to control the deceleration of the EV, whilst recovering the maximum energy from the motors and storing it in the batteries, thereby increasing vehicle efficiency and driving range. For the purpose of this thesis, the ratio of average regeneration current to torque is referred to as the regeneration ratio (RR). The RR for each test is documented in Table 5.2 below and the regeneration waveforms are described in Table 5.3. In Figure 5.23 to Figure 5.25 it is shown that the higher the PWM-ratio the more noise appears on the current waveform. The cause for this noise is unavoidable. The energy accumulates in the motor phases whilst the inverter MOSFETs are on, and then the energy returns to the batteries when the MOSFETSs are switched off. When the MOSFET off-duration is too short an interval for full energy discharge, the energy accumulates in the motor phases until the commutation strategy allows for discharge. At this point all the accumulated energy returns to the battery all at once, creating the current spike.

Table 5.2 below shows the filtered values for regenerative current and deceleration torque, during the constant speed operation (time < 1second), from Figure 5.23 to Figure 5.25. The respective RRs are calculated and displayed in Table 5.2 and a summary of each strategy is documented below in Table 5.3.

Table 5.2 Ratio of regeneration current (A) to deceleration torque (N-m)

	Current (A)			Torque (N-m)			RR (A/N-m)		
PWM-ratio	120°	180°	360°	120°	180°	360°	120°	180°	360°
0.25	1.8	1.8	1.8	5	5	5	0.36	0.36	0.36
0.5	3.5	3.5	3.5	10	10	10	0.35	0.35	0.35
0.75	3	2.5	2	13.9	13.5	12.9	0.22	0.19	0.16
1.0	3	1	0	16.1	15.5	11	0.19	0.06	0

Table 5.3 BLDCHM regeneration waveform description for Figure 5.23 to Figure 5.25

Strategy	Description of the regeneration waveforms
120 degree	As the PWM-ratio increases, both the torque and regenerative current increase, however the RR decreases from 0.36 to 0.19 which indicates a loss of energy in the form of heat as the accumulated energy circulates in the phases before the commutation strategy allows complete discharge back to the batteries.
180 degree	This commutation strategy responds in the same manner as the 120 degree commutation strategy However the RR decreases to a value of 0.06 as the PWM increases to a value of 1, meaning that for the same deceleration torque, the batteries receive less regenerative current when compared to the 120 degree strategy.
360 degree	As the PWM-ratio increases to a value of 0.5, both the torque and regenerative current increase, however as the PWM-ratio tends towards a value of 1, the regeneration current tends towards zero. The reason for this is because the regenerative energy in the motor phases does not have enough time to discharge whilst the MOSFETs are switched off, and the commutation strategy offers no opportunity for discharge. Thus all the regenerative energy is converted to heat in the motor phases.

To implement efficient regeneration when decelerating an EV, the 120 degree commutation strategy is elected as it has the highest RR over the entire operational range.

5.4.3   Torque control during regeneration

The torque controller in Figure 5.14 is for the BLDCHM in motor-mode and is based on current control, but due to the spiking current feedback waveforms during regeneration in generator-mode (shown in Figure 5.23, Figure 5.24and Figure 5.25) the torque controller will not work.

This section proposes a torque controller for the BLDCHM in generator-mode. Section 5.4.2 focused on a BLDCHM in generator mode and compares the deceleration torque and regenerative current, versus the PWM-ratio for various commutation strategies. The results from Section 5.4.2 are used to implement sensorless torque control (meaning no current feedback) for BLDCHM in generator-mode, using the 120-degree commutation strategy. Based the data from Figure 5.23, if the BLDCHM speed is known, an estimation of the deceleration torque reference can be achieved by applying the required PWM-ratio. This requires programming the controller with the BLDCHM

specific responses. The final controller using a PI current controller in motor-mode and a sensorless regeneration controller in generator-mode, is shown below in Figure 5.26.
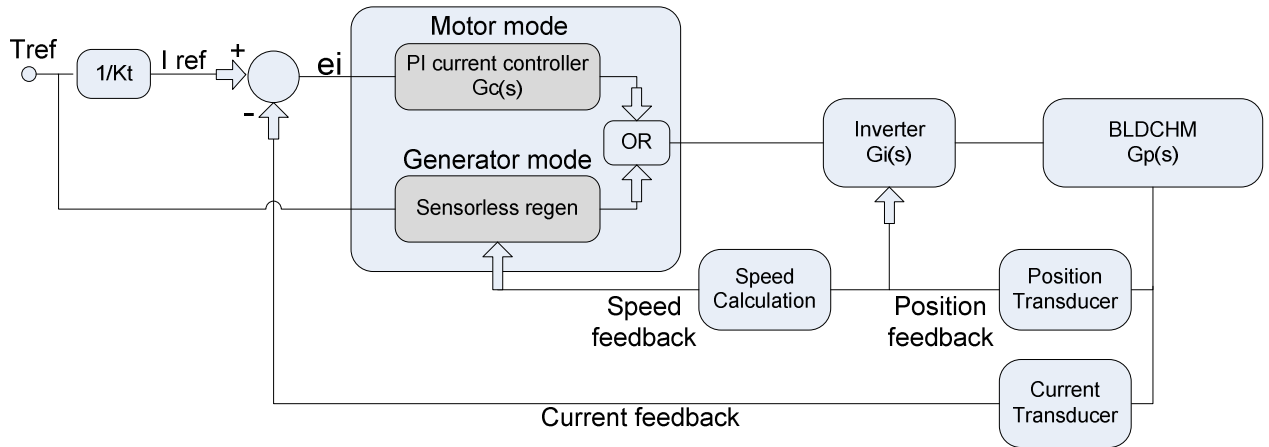
Figure 5.26 Torque controller configuration with sensorless regeneration

The data points from Figure 5.23 are used to determine the entire range for the BLDCHM torque responses in generator mode. To achieve this, the data from all four individual graphs in Figure 5.23 for speed, torque and PWM-ratio are plotted in 3D as blue data points, and appear in Figure 5.27 and Figure 5.28. An ideal surface fit for the data is known as a linear interpolation fit shown in Figure 5.27. Based on the surface fit, the controller can determine the required PWM-ration for any deceleration torque reference. The input variables for the controller are the regeneration torque reference and motor speed with the output being the PWM-ratio [33]. Figure 5.27 shows five different polynomial surface fits (first to fifth order estimations) which can be programmed into the DSP with more ease than the linear interpolation look-up table option. The R-square value (defined by Matlab) represents the accuracy of the estimation surface and is shown in each graph in Figure 5.27. As the order of the polynomial increases, the R-square value tends towards a value of one, thereby implying that a fifth (or higher) order estimation should be used.
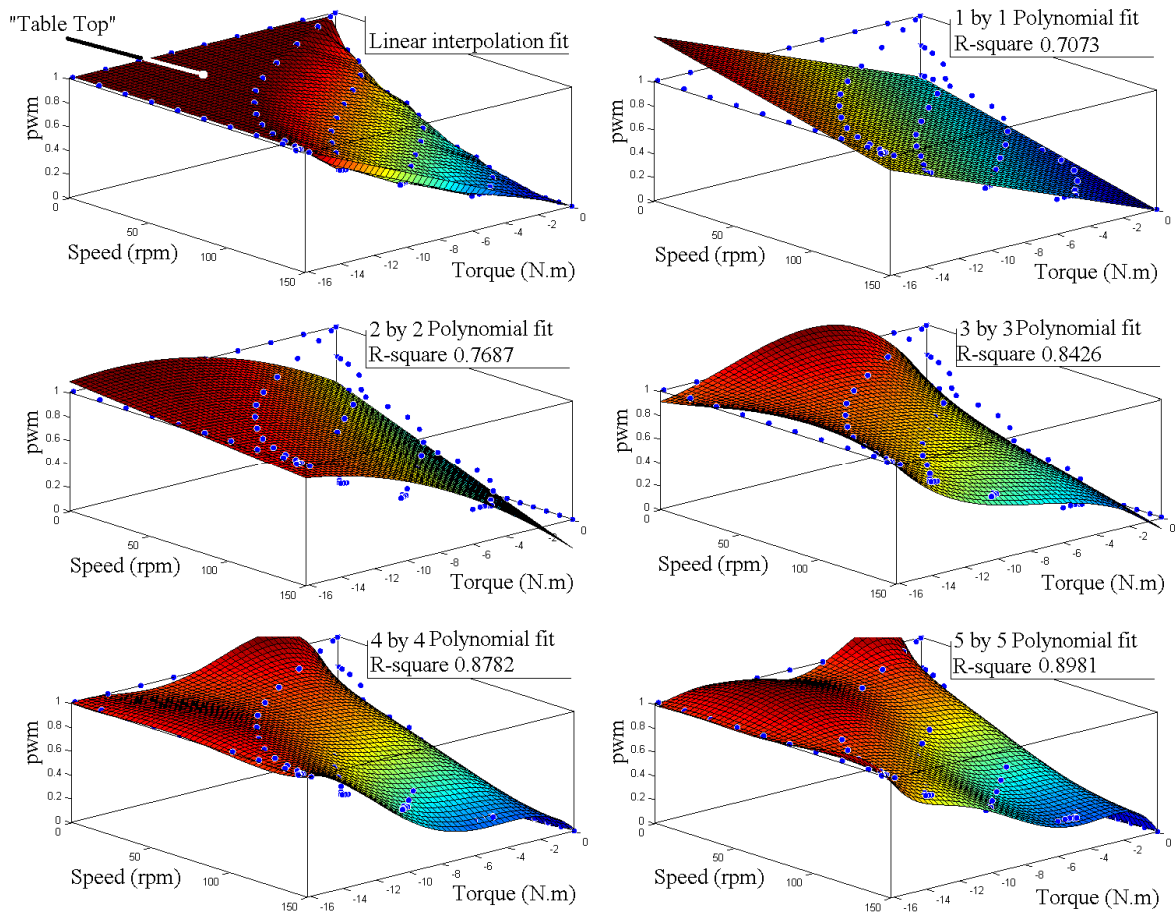
Figure 5.27 Polynomial estimations of the ideal regeneration properties

For all the estimates in Figure 5.27, the polynomial is required to follow the data points as well as create the unity PWM "table top" as appears in the linear interpolation fit. A simpler solution is to limit the output of the polynomial to unity, then the "table top" is automatically generated, provided that the polynomial tends to positive infinity as the speed tends towards zero. This is documented in Figure 5.28 and is referred to as the modified regeneration properties. The modified polynomial is limited to fourth order as a fifth order polynomial fit tends to negative infinity.

Comparing the data from the fifth order ideal regeneration properties (Figure 5.27) and the data for the fourth order modified regeneration properties (Figure 5.28), it is noted that the fifth order polynomial fit has a greater RR value; however in the "table top" region the polynomial estimation varies below the required unit PWM value. This variation at maximum torque (at the respective speed) results in a more prominent torque error during vehicle operation. As a result, the fourth order modified polynomial provides a more efficient solution. The equation for the implemented fourth order modified polynomial and is documented in Appendix C.
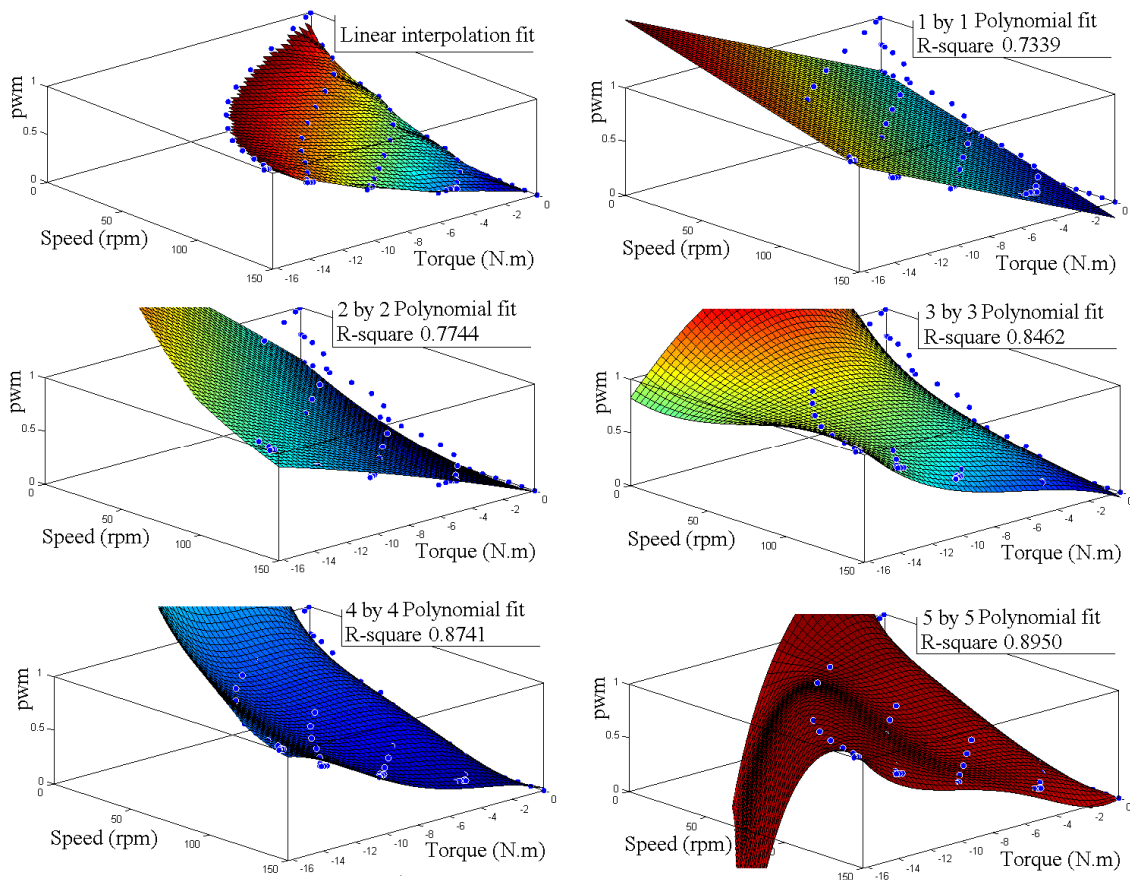
Figure 5.28 Polynomial estimations of the modified regeneration properties

5.5   **Summary**

In this chapter equation (4.23) (developed in Chapter 4), is used to simulate the electrical and mechanical response of a BLDCHM based on the parameters described in Appendix A. It is shown that the back EMF equations for the BLDCHM do not describe ideal trapezoidal waveforms as assumed in Chapter 4 and this is taken into account in the simulation. The implementation of a 120-degree commutation strategy is described and evaluated in this chapter as it requires the state space equation to be modeled for a six step commutation strategy, reliant on motor position as opposed to being a continuous equation. The simulation results are compared to practical results.

The output torque from a BLDCHM is shown to be directly proportional to the current in the motor. Based on this, a current controller is implemented on a Texas Instruments® DSP and results are documented. For deceleration torque, the motor is used in generator mode and regeneration is implemented. The torque produced during regeneration is compared to the charging current fed

back to the batteries, to determine the most efficient inverter-commutation pattern for an EV application. The recorded data is used to determine a fourth order polynomial for the output PWM to the inverter, based on the reference torque and instantaneous speed.

With torque control for both acceleration and deceleration of the BLDCHM, Chapter 6 will develop a control algorithm which uses two BLDCHMs for propulsion and steering of a wheelchair.

Chapter 6   -   Electric Vehicle Steering Algorithm

_____

6.1   Introduction

With the improvement of drive systems and motor designs in recent years, more efficient solutions to wheelchair traction and steering problems are possible. This chapter describes the simulation of the left and right side motor controllers respectively for driving an electric wheelchair (EW) with two hub motors using a joystick interface. Careful attention is paid to ensure that the left and right side controllers track the direction reference provided by the user, even when the two wheels experience a difference in contact friction or in the evenness of floor or road surface. This relieves the user from the task of having to continuously adjust the joystick's direction command to compensate for the EW directional drift whilst ensuring an ergonomic feel for the user.

6.2   Wheelchair configurations

In Chapter 2, the mechanical configuration for an electric vehicle (EV) is described. For the application of a wheel chair, the traditional configuration comprises two electric motors (EM), each one coupled individually through a fixed gearbox (FG) to independent wheels, as appears in Figure 6.1(a). The use of hub motors to drive an EW reduces the weight, cost, mechanical noise, servicing cost and overcomes the poor efficiency related to gearboxes. The two control methods typically used for EWs are torque and speed control. These are investigated and additional control topologies are proposed and evaluated.
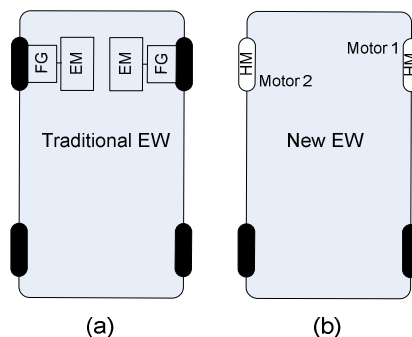
Figure 6.1 Mechanical configurations for EWs

6.2.1   Wheelchair operation under torque control

Torque control is the traditional implementation for a vehicle which uses a mechanical steering wheel and is intuitive for the user. When driving an EW, the user provides an input via a joystick, and based on its position, two torque signals are derived, one for each of the BLDC hub motors. However, when the user wishes to move in a straight line, equal torque produced by each of the hub motors, does not ensure straight line motion due to differences in surface-to-wheel friction (referred to as load torques) and the user is required to continuously adjust the joystick to compensate for directional drift.

6.2.2   Wheelchairs operating under speed control

To improve user direction tracking, wheelchairs can be equipped with speed control [19, 34, 35]. In the control algorithm, the user input is translated into two speed references, one for each hub motor. A speed control loop for each wheel is implemented and by doing so, the directional vector input from the user is tracked. The disadvantage of speed control is that it is not intuitive to the user because a change in load torque does not result in a change of EW speed [1] and slow maneuvers are difficult.

6.3   EW direction tracking utilizing both torque and speed control

This section describes two methods of direction tracking utilizing both torque and speed control algorithms and the user input. By combining the two control algorithms, the result is an intuitive response for the user as well as direction tracking of the EW.

6.3.1   Torque vector input from user

The user applies a torque vector input to control the EW motion. This input is in a two axis Cartesian form (x and y components) and can be from a joystick, sip and puff or ultrasonic sensor. A joystick is considered for the purpose of this thesis. The required response of the left hub motor (indicated in red) and right hub motor (indicated in blue), based on the user input, is shown in Figure 6.2 and described in Table 6.1.

The joystick has eight distinct positions, labeled from 1 to 8 in Figure 6.2. It can also be moved to positions anywhere in between any two of the eight positions, for example shown by $\bar{U}$. The x and y components of the joystick position vector $\bar{U}$ define the specific motion desired by the user and are translated into commands for the left and right motors by the DSP.
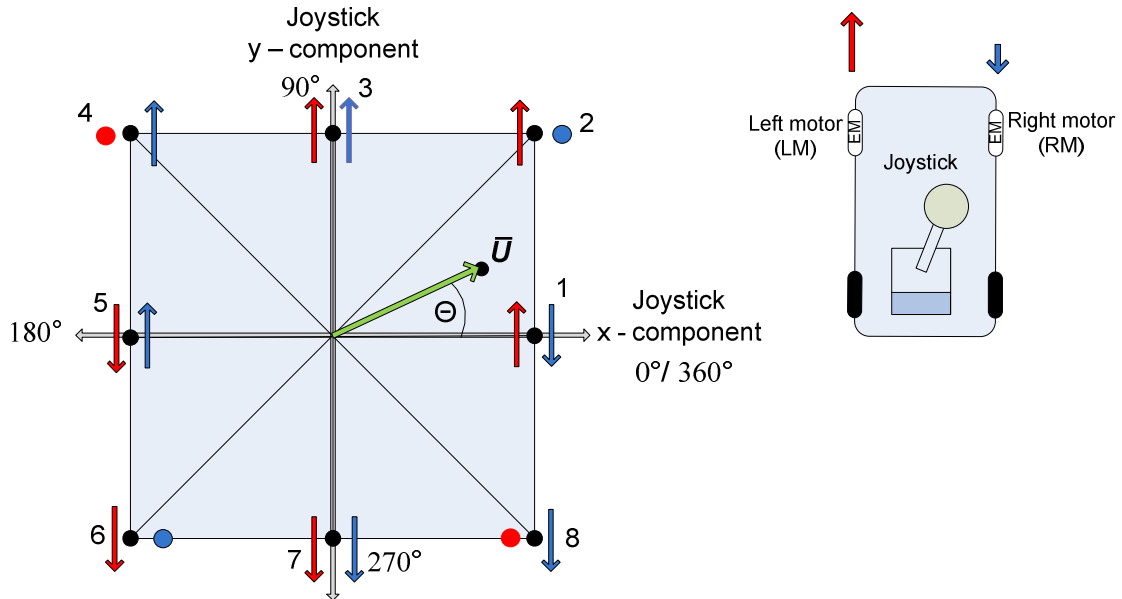
Figure 6.2 Joystick square indicating the desired left and right hub motor responses to the joystick output

Table 6.1 Desired response of BLDC hub motors to joystick output

Discrete joystick position	Left hub motor response	Right hub motor response	Wheel chair response
1 $\Theta j=0°$	Forward rotation	Reverse rotation	Turns on a single point in a clockwise direction with the center of the EW as the rotating axis.
2 $\Theta j=45°$	Forward rotation	Standstill	Rotation in a clockwise direction with the right wheel acting as a pivot axis.
3 $\Theta j=90°$	Forward rotation	Forward rotation	Straight line tracking in forward direction.

4 $\Theta j=135°$	Standstill	Forward rotation	Rotation in a counterclockwise direction with the left wheel acting as a pivot axis.
5 $\Theta j=180°$	Reverse rotation	Forward rotation	Turns on a single point in a counterclockwise direction with the center of the EW as the rotating axis.
6 $\Theta j=225°$	Reverse rotation	Standstill	Rotation in a counterclockwise direction with the right wheel acting as a pivot point.
7 $\Theta j=270°$	Reverse rotation	Reverse rotation	Straight line tracking in reverse direction.
8 $\Theta j=315°$	Standstill	Reverse rotation	Rotation in a clockwise direction with the left wheel acting as a pivot axis.

The user input vector $\bar{U}$ for the desired torque is calculated from the joystick's x and y component reference values. Because the perimeter of the joystick motion is square in shape, the greatest magnitude for $\bar{U}$ is at 45°, 135°, 225° and 315°. For wheelchair operation, a circular profile is required so that the same magnitude of torque command is obtained irrespective of the angle of the joystick. Figure 6.3 (A) shows the ideal x and y values and are trapezoidal in shape when the joystick is rotated though 360 degrees along the perimeter of the joystick square in Figure 6.2. To achieve the required circular profile, the magnitude of $\bar{U}$ is limited to that achieved at a position of 90°. To determine the left and right motor torque references, a lookup table can be used. However to simplify the coding of the DSP, another option is to use the inputs from the joystick and estimate the desired torque commands. Due to the shape of the ideal torque commands as the joystick is rotated through 360°, a sinusoidal estimation is chosen and shown in Figure 6.3 (B). With a 45° offset of the angle Θj, a sine wave estimation for the magnitude of the left (T_L_ref) and right (T_R_ref) hub motors' controller torque references is made. The magnitude and the direction of the EW are calculated from the x and y components as appears below.

$$|\bar{U}| = \sqrt[2]{x^2 + y^2}$$

(6.1)

$$\Theta j = tan^{-1}\left[\frac{y}{x}\right]$$

(6.2)

where:

- $|\bar{U}|$ is the instantaneous vector magnitude from the joystick.
- Θj is the instantaneous vector angle from the joystick.
- x is the horizontal component from the joystick.
- y is the vertical component from the joystick.

The equations to calculate T_{R_ref} and T_{L_ref}, within the DSP, are given below. A gain of (1/0.7) is necessary to ensure that the sinusoidal estimation fits the required trapezoidal response, with the output magnitude limited to ±1 representing ±100% of the user input, as shown in Figure 6.3 (B).

$$T_{R\_ref} = \begin{cases} -1 & \text{where} & \left[\dfrac{|\bar{U}|}{0.7}\right] * sin(\Theta j - 45°) < -1 \\[3em] \left[\dfrac{|\bar{U}|}{0.7}\right] * sin(\Theta j - 45°) & \text{where} & -1 \leq \left[\dfrac{|\bar{U}|}{0.7}\right] * sin(\Theta j - 45°) \leq 1 \\[3em] 1 & \text{where} & \left[\dfrac{|\bar{U}|}{0.7}\right] * sin(\Theta j - 45°) > 1 \end{cases} \quad (6.3)$$

The DSP uses the function in equation (6.3) (with the output magnitude limited to 1) to determine the right motor torque reference, without requiring a large lookup table.

T_{L_ref} is calculated in the same manner as T_{R_ref} but with a 90° offset.

$$T_{L\_ref} = \begin{cases} -1 & \text{where} & \left[\dfrac{|\bar{U}|}{0.7}\right] * sin(\Theta j + 45°) < -1 \\[3em] \left[\dfrac{|\bar{U}|}{0.7}\right] * sin(\Theta j + 45°) & \text{where} & -1 \leq \left[\dfrac{|\bar{U}|}{0.7}\right] * sin(\Theta j + 45°) \leq 1 \\[3em] 1 & \text{where} & \left[\dfrac{|\bar{U}|}{0.7}\right] * sin(\Theta j + 45°) > 1 \end{cases} \quad (6.4)$$
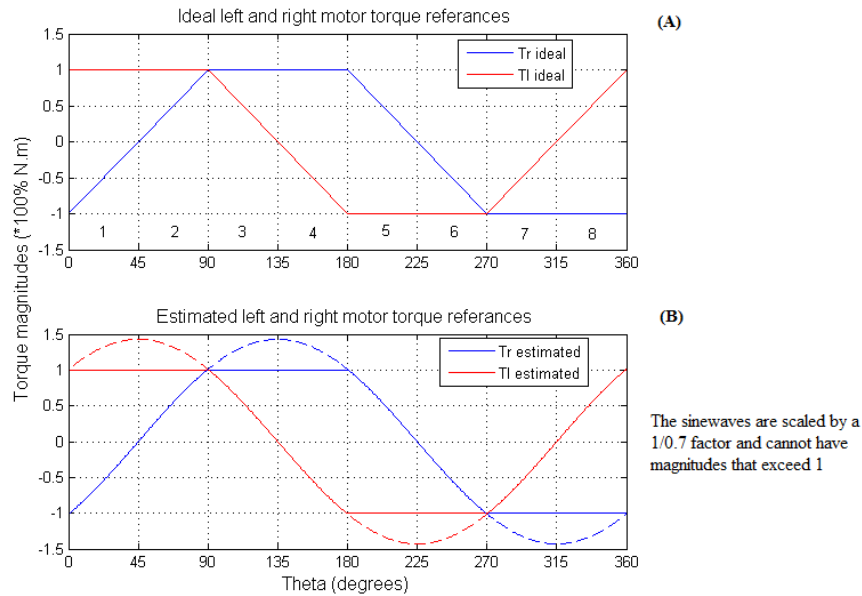
Figure 6.3 Ideal vs estimated left and right motor torque references

As the joystick is moved around, the x and y coordinates are converted into torque commands for the right and left motors. For example when $\Theta j=0°$, the right motor (blue curve) gets a torque command of -1 which means it will produce torque in the reverse direction of rotation, while the left motor (red curve) gets a torque command of +1 which means it will produce torque in the forward direction of rotation, as summarized by the first line of information in Table 6.1.

6.3.2   Control strategies for the left and right hub motors

This section proposes two algorithms which utilize both torque and speed control to achieve the user-desired response from the EW. The proposed control strategies are better understood when considering human expectations. The majority of day-to-day activities which a person might undertake are subject to a torque input from the user.

Consider the following:

- When opening a screw lid container, a torque difference between the lid and the container is required.
- When playing golf, an increase in hitting distance is achieved by applying more torque whilst swinging the club before impacting the ball.
- When riding a bicycle, an increase in speed is achieved by applying more torque to the pedals and in turn the rear wheel.

- When kayaking, an increase in speed is achieved by apply more torque to the paddle when paddling through the water.

- When driving a motor vehicle, an increase in speed is achieved by pressing the accelerator pedal harder. This in turn increases the amount of fuel injected into the engine, increasing output torque on the driving wheels.

With this realization, the user input into the controller of the EW motors needs to be a torque reference and the speed of the vehicle should be a consequence of the output torque from the motors and the surrounding surface conditions and gradient. However, the right and left motors cannot both be under torque control. Any difference in surface condition would then cause the EW to drift off course which would require a correction by the user via the joystick. This problem is solved by putting torque control onto say the right motor, and speed control onto the left motor, forcing the left motor to run at a defined speed as some ratio of the right motor speed, thus keeping the EW on the desired trajectory.

6.3.2.1   Proposed control strategy 1

For this control strategy the right motor is under torque control and the control algorithm is shown in Figure 6.4 below. T_{R_ref} is derived directly from the joystick position according to equation (6.3).
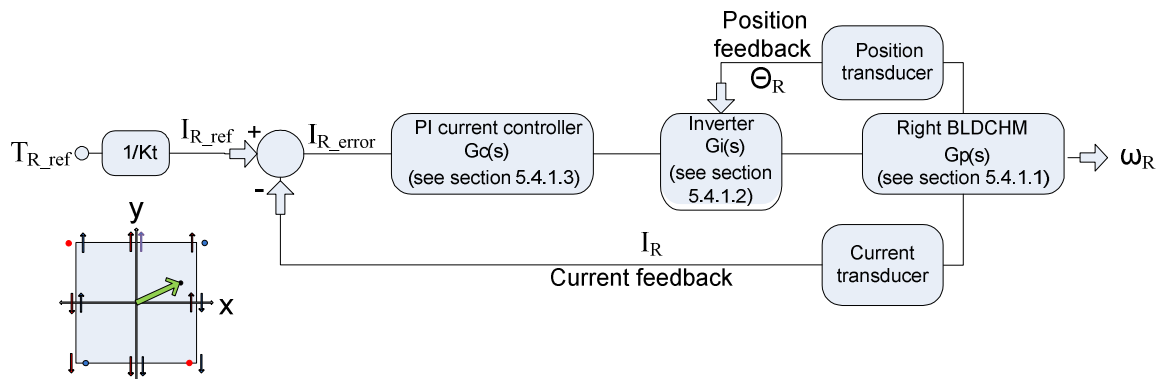
Figure 6.4 Strategy 1 - Right motor under torque control

If the EW is to track the direction command by the user, the ideal response of the left motor should be predictable and based on the output speed of the right motor as mentioned above. To accurately control the left motor a speed control algorithm is implemented, with the input reference based on the speed of the right motor and the position of the joystick. The equation to calculate the left motor speed reference (ω_{L_ref}) is shown below and the speed control algorithm for the left motor

is shown in Figure 6.5. For example, if the user desires to move strait forward, then the two torque commands form the joystick would be equal, and in equation (6.5) the left and right motor speeds would be equal, no matter what the difference in surface conditions or wheel slip.

However, there is an exception. For the left motor controller to be effective, a check is implemented for $T_R\_ref = 0$ or $\omega_R\_ref = 0$, and if either of the conditions are met, T_L_ref from the joystick becomes the torque controller reference and the left motor operates under torque control.

$$\omega_{L}\_ref = \omega_R * \left[\frac{T_L\_ref}{T_R\_ref}\right]$$

(6.5)

where:

- ω_{L}_ref is the left hub motor speed reference (rad/sec).
- ω_R is instantaneous right hub motor speed (rad/sec).
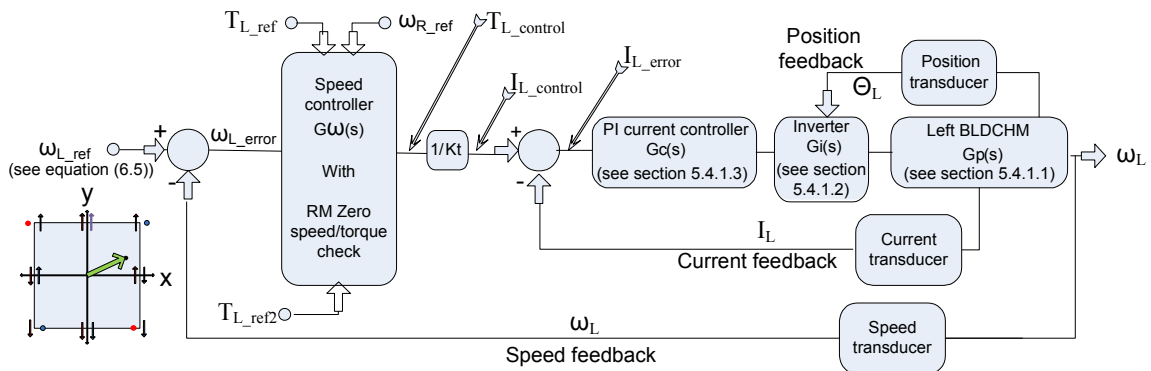
Figure 6.5 Strategy 1 - Left motor under speed control

The EW response from this control strategy has disadvantages. A load change on either of the wheels should ideally result in a change in speed of the EW without a directional change whilst the algorithm tracks the joystick torque references. A load change on the right motor will affect the speed of the right motor and thus also the left motor and therefore the EW (this is an ideal response). However with the left motor under speed control, any load change on the left motor will maintain directional tracking but have no affect on the speed of the EW (this is not an ideal response). Section 6.4 simulates this control strategy and better illustrates the disadvantage.

6.3.2.2   Proposed control strategy 2

The second control strategy is similar to the first strategy, with an additional feature. With the right motor under torque control and the left motor under speed control, the EW did not experience a speed change dependent on the left motor load.

In this second control strategy the additional feature is a low pass limiter which is implemented on the left motor torque reference. The addition of this limiter allows for feedback from the left motor controller to be used in the right motor torque control loop, allowing the effect of a load on the left motor to be transferred to the right motor controller. When the left motor torque reference reaches the low pass limiter limit whilst it is trying to maintain tracking, the limiter feedback to the right motor torque controller causes the right motor torque reference to be adjusted to allow for the tracking. With this low pass limiter feedback, the required left motor speed response to a load input is referred to the right motor which is under torque control and the EW speed will respond accordingly to an increased load. This controller is shown in

Figure **6.6** and is referred to as the final control strategy (FCS).
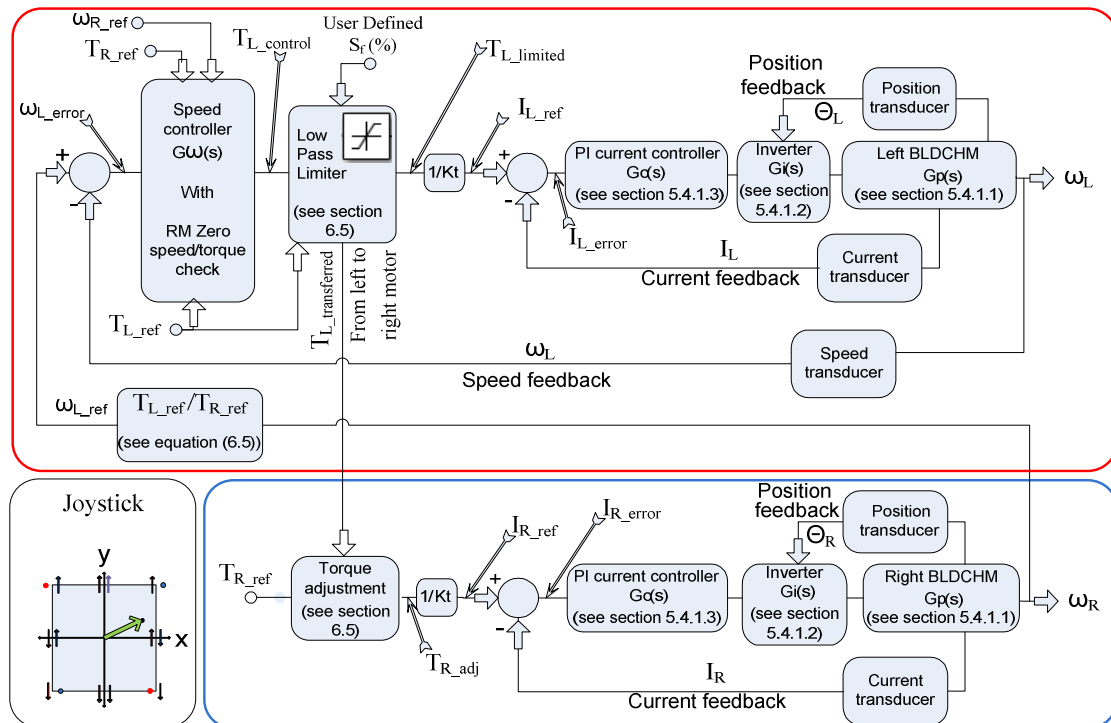
Figure 6.6 Control strategy 2

It is important to note that the configuration of the low pass limiter will affect the response of the EW and is described in more details in section 6.5.

6.4 **EW control algorithm simulations**

This section describes the simulation of an EW using Matlab®. The EW mechanical configuration in Figure 6.2 is used, with the output responses plotted for each of the four control strategies listed below.

Table 6.2 Simulated control strategy configurations

EW configuration 1	The left and right hub motors are both under torque control as described in section 6.2.1.
EW configuration 2	The left and right hub motors are both under speed control as described in section 6.2.2.
EW configuration 3	The right hub motor is under torque control and the left hub motor is under speed control. The left hub motor speed set point is based on the user input and the right hub motor speed as described in section 6.3.2.1.
EW configuration 4	The right hub motor is under torque control and the left hub motor is under speed control. Feedback from the right hub motor speed is used in the left hub motor control whilst feedback from the left hub motor torque limiter is used in the right hub motor torque control as described in section 6.3.2.2.

The aim for the EW control is to achieve an intuitive response for the user irrespective of external load increases on either of the two hub motors, whilst achieving direction tracking. The following criteria are required for the controller to meet this aim:

- EW direction tracking: The direction of the EW tracks the user input, irrespective of the load torque for either of the hub motors.
- EW speed response: The speed of the EW depends on the load torque experienced by each of the motors independently. When the load torque is increased the EW speed should decrease and vice versa. This speed response occurs irrespective of which hub motor experiences the change in load torque.

6.4.1   Simulation results

In order to determine which of the control strategies listed in Table 6.2 meets both criteria listed above, the responses to four different joystick positions are simulated, with each one in turn evaluated for three different load torque configurations. The four joystick positions are selected in order to evaluate the motors in different operational states:

- Position 1: 90° - Both the left motor and the right motor are required to have forward rotation at the same speed, resulting in the EW moving forward in a straight line.
- Position 2: 45° - The left motor is required to have a forward rotation and the right motor is at standstill, resulting in the EW rotating in a clockwise with the right motor as the pivot axis.
- Position 3: 0° - The left motor is required to have a forward rotation and the right motor a reverse rotation, resulting in the EW rotating clockwise with the centre of the EW as the pivot axis.
- Position 4: 60° - Both the left motor and the right motor are required to have forward rotation, but with the left motor at a higher speed, resulting in the EW gradually cornering to the right.

The load torque is selected to illustrate the controller response to different operating states:

- State 1: Constant and equal load torque – This represents ideal surface conditions and shows the expected motion of the EW to a joystick command.
- States 2 and 3: Step load on the left motor or right motor – A step load identifies errors in tracking, but by doing this test individually for the left motor (state 2) and right motor (state 3) any potential errors in speed tracking due to speed control are identified.

Figure 6.7 describes how the label of a simulation result relates to the input variables for Figure 6.8 to Figure 6.18.

```
┌──────────────────────────────────────────────────────────────────┐
│  Figure _._ Simulation xx                                          │
│                          ⇨a,b or c – representing the applied load │
│                                                                    │
│                          ⇨1,2,3 or 4 – representing the joystick position │
│    1x – joystick position = 90°                                    │
│    2x – joystick position = 45°    xa – left and right load torque constant │
│    3x – joystick position = 0°     xb – left load torque step increase at t=5sec │
│    4x – joystick position = 60°    xc – right load torque step increase at t=5sec │
└──────────────────────────────────────────────────────────────────┘
```

Figure 6.7 Simulation input variable description

6.4.1.1 Simulation 1a: Joystick position of 90° with left and right load torques equal and constant

Simulation 1a shows the EW response to a joystick position of 90° with left and right load torques equal and constant which represents ideal surface conditions. The results in Figure 6.8, 1a, 2a, 3a and 4a, show the 2D motion of the EW as would appear from the top view. The left wheel (represented in red) and right wheel (represented in blue) have an equal but opposite offset from the zero point in the x direction. This offset represents the wheel base (distance between wheels) of the EW. The left and right wheels proceed in parallel lines along the y-axis showing that the motion of the EW tracks the joystick position of 90°.

Figure 6.8, 1b, 2b, 3b and 4b show the individual distance traveled for the left wheel (represented in red) and right wheel (represented in blue). There is no load torque deviation throughout the simulation and thus the speeds are constant, resulting in both motors having identical linear distance plots.

The simulated response (forward motion in a straight line) is identical for each of the four EW configurations listed in Table 6.2, which is expected for ideal surface conditions.
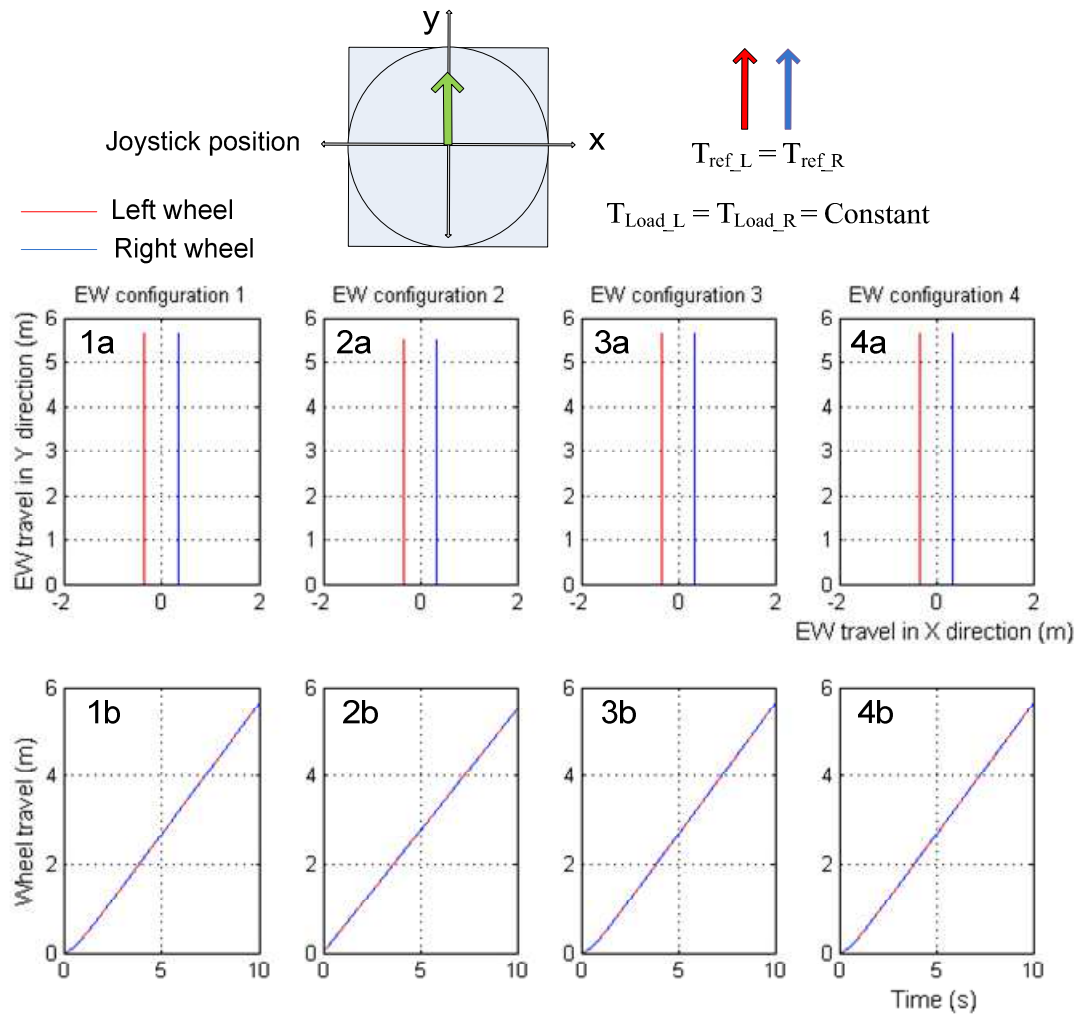
Figure 6.8 EW response - Simulation 1a, showing the EW response to a joystick position of 90° with left and right load torques equal and constant.

6.4.1.2   Simulation 1b: Joystick position of 90° with a step load torque increase on the left wheel

Simulation 1b shows the EW response to a joystick position of 90° with a step load torque increase on the left wheel at 5 seconds. Figure 6.9, 1b, 2b, 3b and 4b show the individual distance traveled by the left wheel (represented in red) and right wheel (represented in blue). The results in Figure 6.9, 1a, 2a, 3a and 4a, show the 2D motion of the EW as would appear from the top view. The left wheel (represented in red) and right wheel (represented in blue) have an equal but opposite offset from the zero point in the x direction. This offset represents the wheel base (distance between wheels) of the EW. The left and right wheels proceed in parallel lines along the y-axis showing that the motion of the EW tracks the joystick position of 90° until a load torque increase on the left wheel at 5 seconds.

- For configuration 1, consider Figure 6.9, 1a and 1b. The speed of the left motor decreases as the load torque is applied. Figure 6.9, 1b shows that the left motor speed decrease because the distance traveled decreases, but the right motor speed in unaffected. The result on the EW motion is that it veers to the left drastically and this is shown in Figure 6.9, 1a. The criterion for EW directional tracking of the joystick irrespective of the load torque on either of the hub motors is thus not satisfied.

- For configuration 2 and 3, consider Figure 6.9, 2a, 2b, 3a and 3b. Both configurations have the left motor under speed control, so when the load torque is applied there is no change to motor speed and thus no decrease to the distance traveled in Figure 6.9, 2b and 3b. The criterion that the EW speed response is dependent on the load torque applied to either of the hub motors is thus not satisfied.

- For configuration 4 consider Figure 6.9, 4a and 4b. The speed of both the left and right motors decrease as the load torque is applied to the left motor. This is shown by the equal gradient reduction of the left and right motors distance graphs in Figure 6.9, 4b. The result on EW motion is that the joystick direction is accurately tracked (shown in Figure 6.9, 4a), and the speed decreases as a load is applied. This is an ideal response.
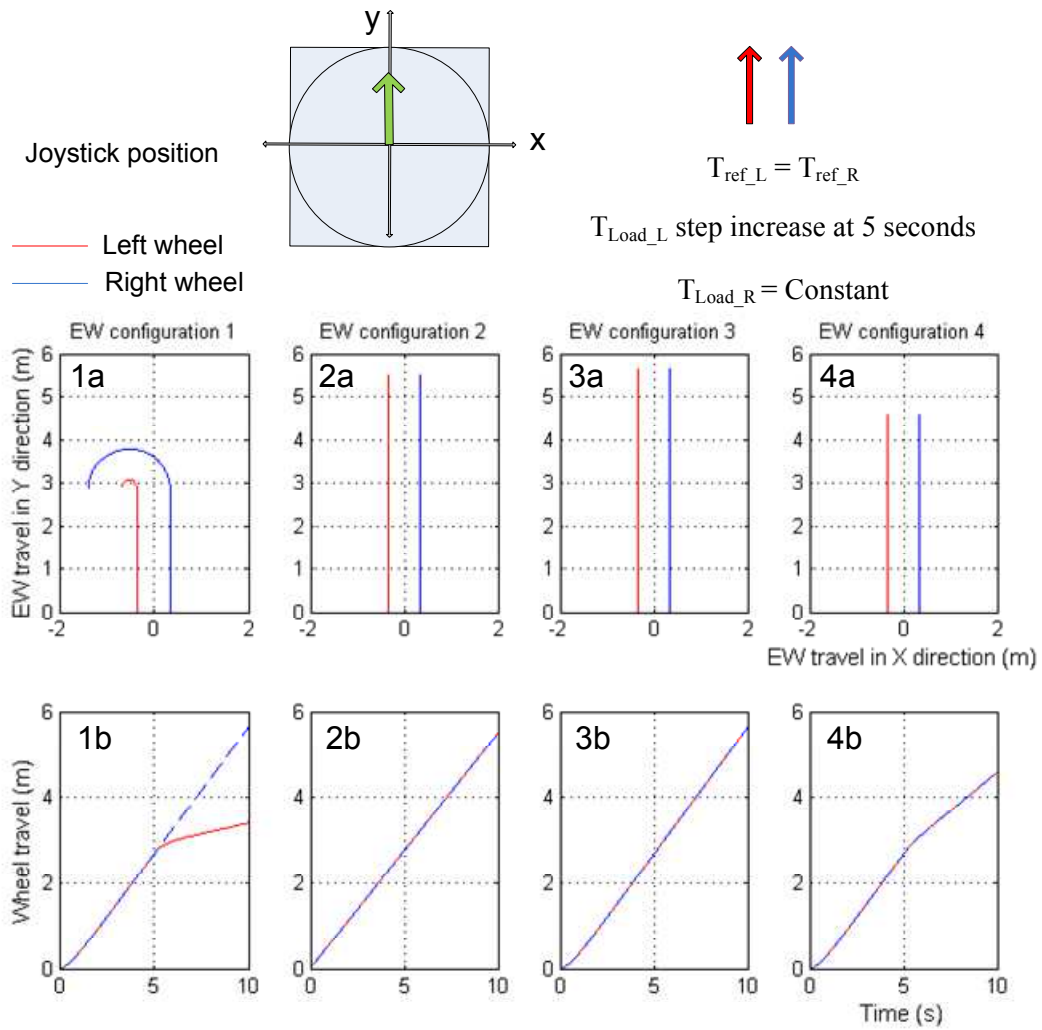
Figure 6.9 EW response - Simulation 1b, showing the EW response to a joystick position of 90° with a step load torque increase on the left wheel at 5 seconds.

6.4.1.3   Simulation 1c: Joystick position of 90° with a step load torque increase on the right wheel

Simulation 1c shows the EW response to a joystick position of 90° with a step load torque increase on the right wheel at 5 seconds. Figure 6.10, 1b, 2b, 3b and 4b show the individual distances traveled by the left wheel (represented in red) and right wheel (represented in blue). The results in Figure 6.10, 1a, 2a, 3a and 4a, show the 2D motion of the EW as would appear from the top view. The left wheel (represented in red) and right wheel (represented in blue) have an equal but opposite offset from the zero point in the x direction. This offset represents the wheel base (distance between wheels) of the EW. The left and right wheels proceed in parallel lines along the y-axis showing that the motion of the EW tracks the joystick position of 90° until a load torque increase on the right wheel at 5 seconds.

- For configuration 1, consider Figure 6.10, 1a and 1b. The speed of the right motor decreases as the load torque is applied. Figure 6.10, 1b shows that the right motor speed decrease because the distance traveled decreases, but the left motor speed in unaffected. The result on the EW motion is that it veers to the right drastically and this is shown in Figure 6.10, 1a. The criterion for EW directional tracking of the joystick irrespective of the load torque on either of the hub motors is thus not satisfied.

- For configuration 2, consider Figure 6.10, 2a and 2b. The right motor is under speed control, so when the load torque is applied there is no change to motor speed and thus no decrease to the distance traveled in Figure 6.10, 2b. The criterion that the EW speed response is dependent on the load torque applied to either of the hub motors is thus not satisfied.

- For configuration 3 and 4 consider Figure 6.10, 3a, 3b, 4a and 4b. The speed of both the left and right motors decrease as the load torque is applied to the right motor. This is shown by the equal gradient reduction of the left and right motors distance graphs in Figure 6.10 3b and 4b. The result on EW motion is that the joystick direction is accurately tracked (shown in Figure 6.10, 3a and 4a), and the speed deceases as a load is applied. This is an ideal response.
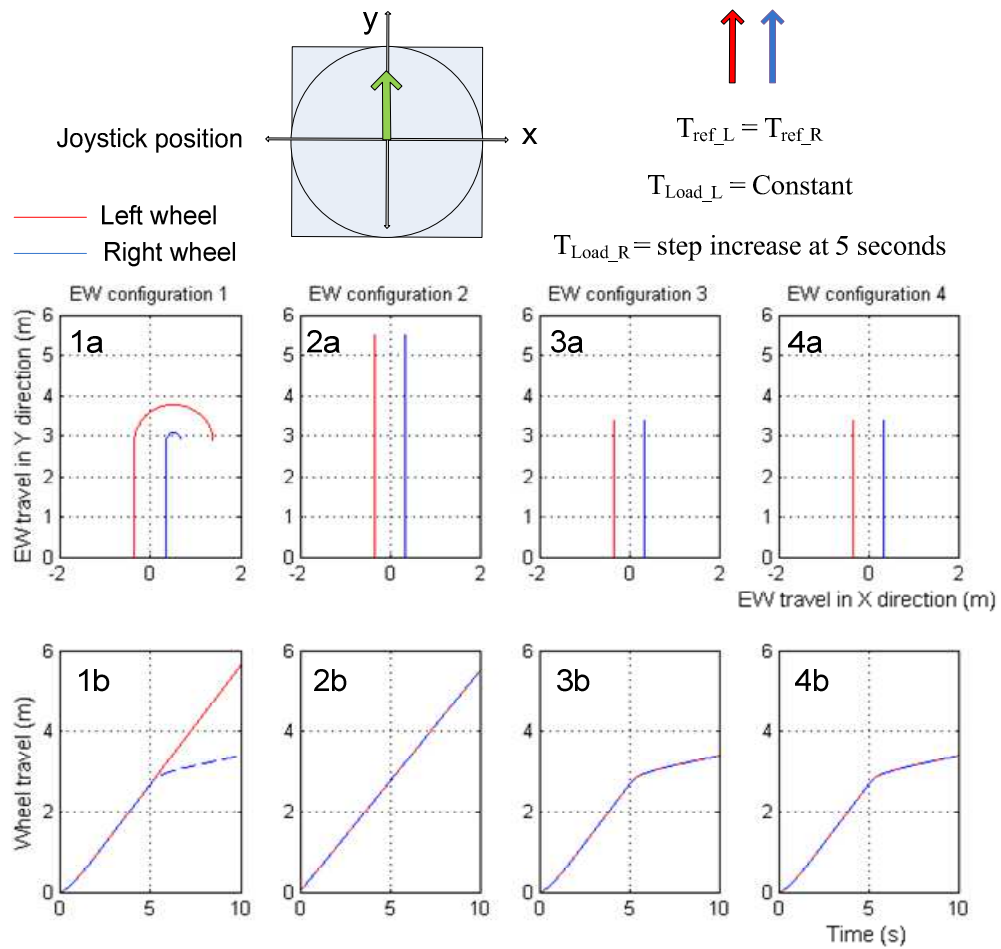
Figure 6.10 EW response - Simulation 1c, showing the EW response to a joystick position of 90° with a step load torque increase on the right wheel at 5 seconds.

6.4.1.4   Simulation 2a: Joystick position of 45° with left and right load torques equal and constant

Simulation 2a shows the EW response to a joystick position of 45° with left and right load torques equal and constant which represents ideal surface conditions. The results in Figure 6.11, 1a, 2a, 3a and 4a, show the 2D motion of the EW as would appear from the top view. The left wheel (represented in red) has a forward motion and right wheel (represented in blue) is at standstill. The two wheels have an equal but opposite offset from the zero point in the x direction. This offset represents the wheel base (distance between wheels) of the EW. With the right wheel stationary, the left wheel causes the EW to move in a clockwise circle, with the right wheel as the pivot point.

Figure 6.11, 1b, 2b, 3b and 4b show the distance traveled by the left wheel (represented in red) and right wheel (represented in blue). There is no load torque deviation throughout the simulation and thus the speed of the left wheel is constant, resulting in the left motor having a linear distance plot. The right wheel remains at standstill.

The simulated response (EW clockwise rotation pivoting around the right motor) is identical for each of the four EW configurations listed in Table 6.2, which is expected for ideal surface conditions.
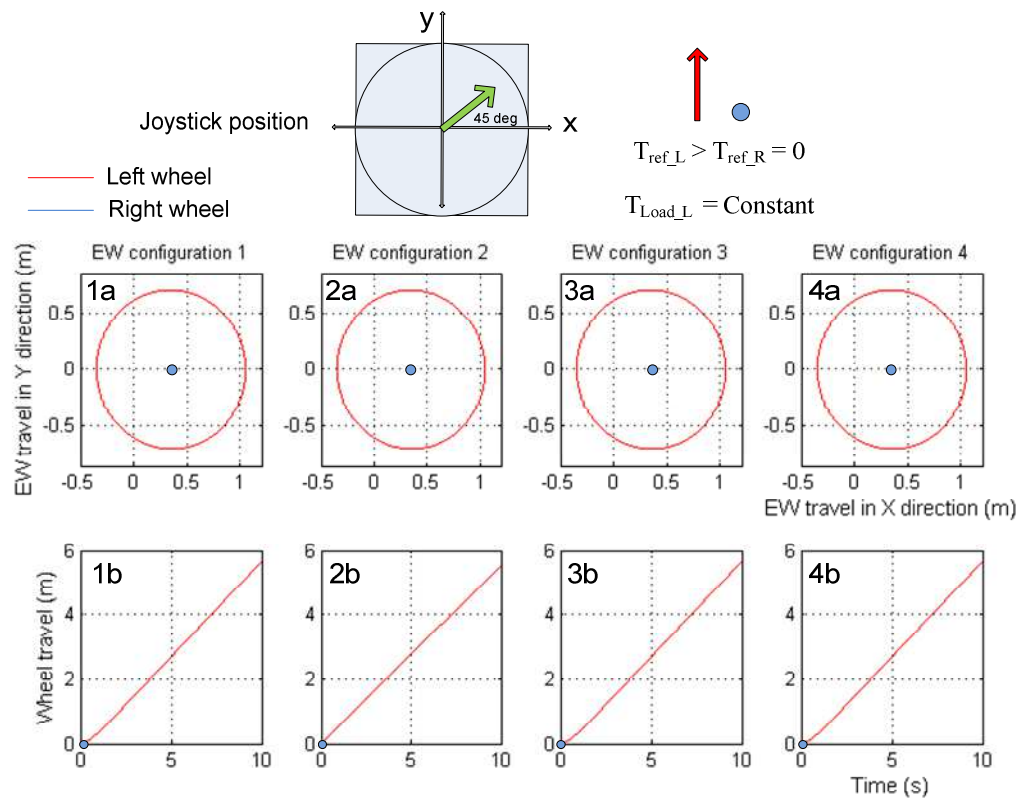
Figure 6.11 EW response - Simulation 2a, showing the EW response to a joystick position of 45° with left and right load torques equal and constant.

6.4.1.5   Simulation 2b: Joystick position of 45° with a step load torque increase on the left wheel

Simulation 2b shows the EW response to a joystick position of 45° with a step load torque increase on the left wheel at 5 seconds. With the right motor at standstill for this simulation, direction tracking is inherently achieved.

Figure 6.12, 1b, 2b, 3b and 4b show the distance traveled by the left wheel (represented in red) whilst the right wheel (represented in blue) is at standstill. The results in Figure 6.12, 1a, 2a, 3a and 4a, show the 2D motion of the EW as would appear from the top view. The left wheel (represented in red) and right wheel (represented in blue) have an equal but opposite offset from the zero point in the x direction. This offset represents the wheel base (distance between wheels) of the EW. With the right wheel stationary, the left wheel causes the EW to move in a clockwise circle, with the right wheel as the pivot point.

- For configuration 2, consider Figure 6.12, 2a and 2b. The left motor under speed control, so when the load torque is applied there is no change to motor speed and thus no decrease to the distance traveled in Figure 6.12, 2b. The criterion that the EW speed response is dependent on the load torque applied to either of the hub motors is thus not satisfied. This is also shown in Figure 6.12, 2a because the EW achieves a full rotation.

- For configuration 1, 3 and 4 consider Figure 6.12, 1a, 1b, 3a, 3b, 4a and 4b. The speed of the left motor decrease as the load torque is applied. This is shown by the gradient reduction of the left motor distance graphs in Figure 6.12, 1b, 3b and 4b. The result on EW motion is that the joystick direction is accurately tracked (shown in Figure 6.12, 1a, 3a and 4a), but only ¾ of a clockwise rotation is achieved. This is an ideal response.
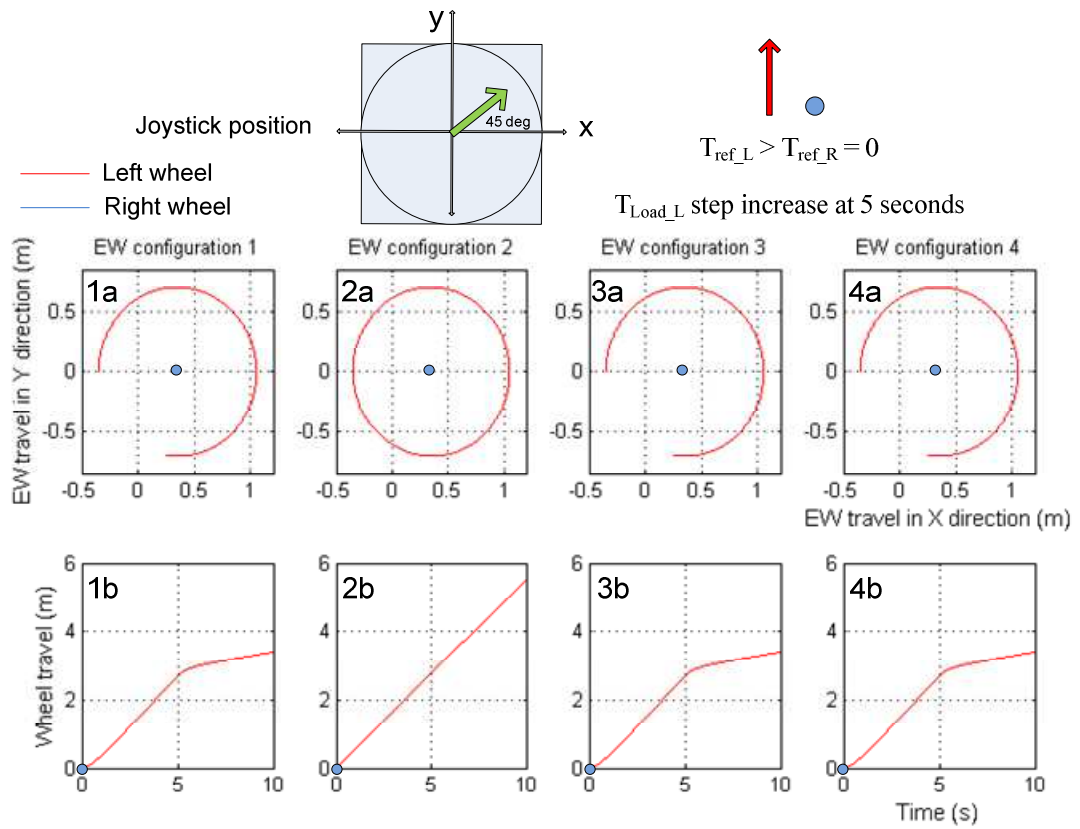
Figure 6.12 EW response - Simulation 2b, showing the EW response to a joystick position of 45° with a step load torque increase on the left wheel at 5 seconds.

6.4.1.6 Simulation 3a: Joystick position of 0° with left and right load torques equal and constant

Simulation 3a shows the EW response to a joystick position of 0° with left and right load torques equal and constant which represents ideal surface conditions.

The results in Figure 6.13, 1a, 2a, 3a and 4a, show the 2D motion of the EW as would appear from the top view. The left wheel (represented in red) has a forward speed and right wheel (represented in blue) has a reverse speed. The two wheels have an equal but opposite offset from the zero point in the x direction. This offset represents the wheel base (distance between wheels) of the EW. The resulting effect on the EW due to the left and right wheels having equal but opposite speeds, is a clockwise rotation with the centre of the EW as the pivot reference.

Figure 6.13, 1b, 2b, 3b and 4b show the distance traveled by the left wheel (represented in red) and right wheel (represented in blue). There is no load torque deviation throughout the simulation and thus the speed of the left and right wheels are constant and opposite in directions. The resulting displacement plots for the left and right wheels are linear and equal but in opposite directions.

The simulated response (EW clockwise rotation with the centre of the EW as the pivot reference) is identical for each of the four EW configurations listed in Table 6.2, which is expected for ideal surface conditions.
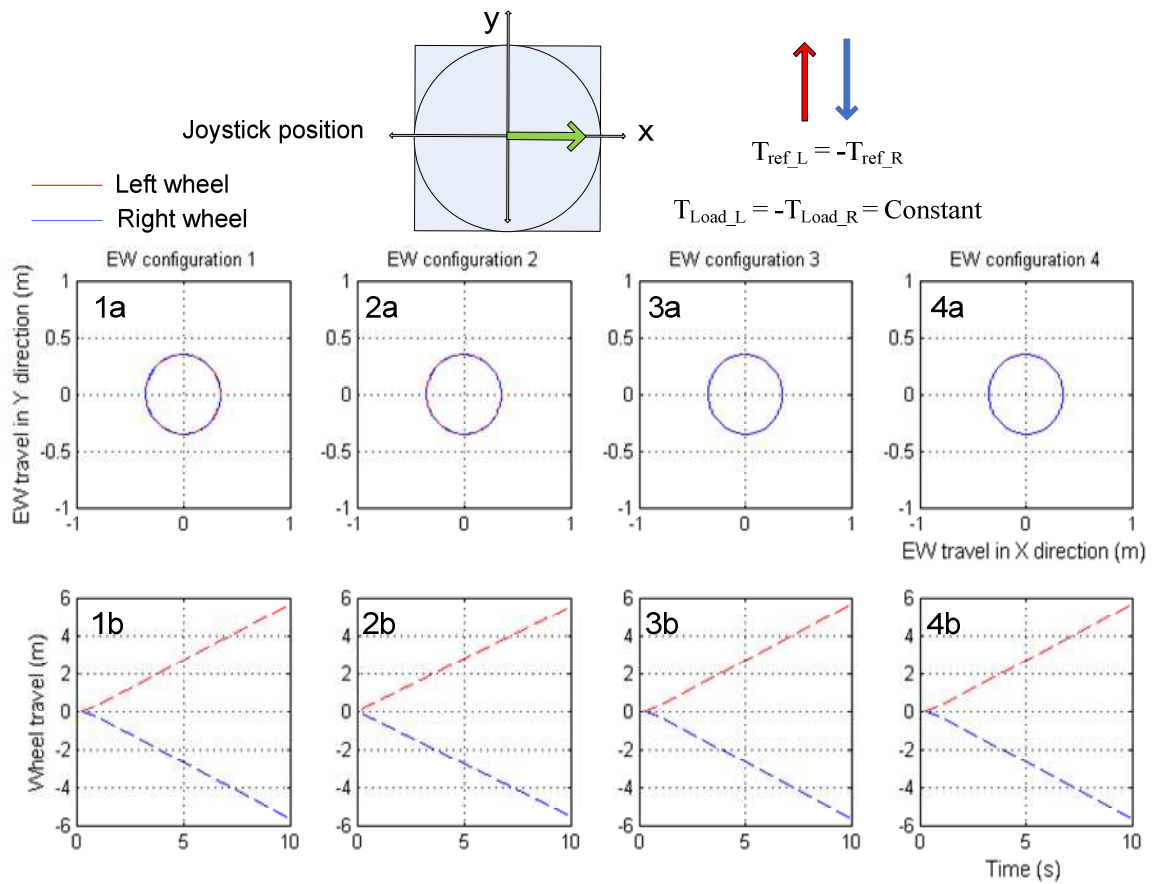
Figure 6.13 EW response - Simulation 3a, showing the EW response to a joystick position of 0° with left and right load torques equal and constant.

6.4.1.7   Simulation 3b: Joystick position of 0° with a step load torque increase on the left wheel

Simulation 3b shows the EW response to a joystick position of 0° with a step load torque increase on the left wheel at 5 seconds.

Figure 6.14, 1b, 2b, 3b and 4b show the individual distances traveled by the left wheel (represented in red) and right wheel (represented in blue). The results in Figure 6.14, 1a, 2a, 3a and 4a, show the 2D motion of the EW as would appear from the top view. The left wheel (represented in red) and right wheel (represented in blue) have an equal but opposite offset from the zero point in the x direction, representing the wheel base (distance between wheels) of the EW. The equal and opposite speeds of the left and right wheels cause the EW to rotate in a clockwise circle (with the center of the EW as the pivot reference) showing that the motion of the EW tracks the joystick position of 0° until a load torque increase on the left wheel at 5 seconds.

- For configuration 1, consider Figure 6.14, 1a and 1b. The speed of the left motor decreases as the load torque is applied. Figure 6.14, 1b shows that the left motor speed decreases because the distance traveled decreases, but the right motor speed is unaffected. The result on the EW motion is that the diameter of the clockwise rotation increases and the pivot axis moves from the center of the EW towards the left wheel as shown in Figure 6.14, 1a. The criterion for EW directional tracking of the joystick irrespective of the load torque on either of the hub motors is thus not satisfied.

- For configuration 2 and 3, consider Figure 6.14, 2a, 2b, 3a and 3b. The left motor is under speed control, so when the load torque is applied there is no change the motor speed and thus no decrease to the distance traveled in Figure 6.14, 2b and 3b. The criterion that the EW speed response is dependent on the load torque applied to either of the hub motors is thus not satisfied.

- For configuration 4 consider Figure 6.14 4a and 4b. The speed of both the left and right motors decrease as the load torque is applied to the left motor. This is shown by the equal gradient reduction of the left and right motors distance graphs in Figure 6.14, 4b. The result on EW motion is that the joystick direction is accurately tracked (shown in Figure 6.14, 4a), and the speed deceases as a load is applied. This is an ideal response.
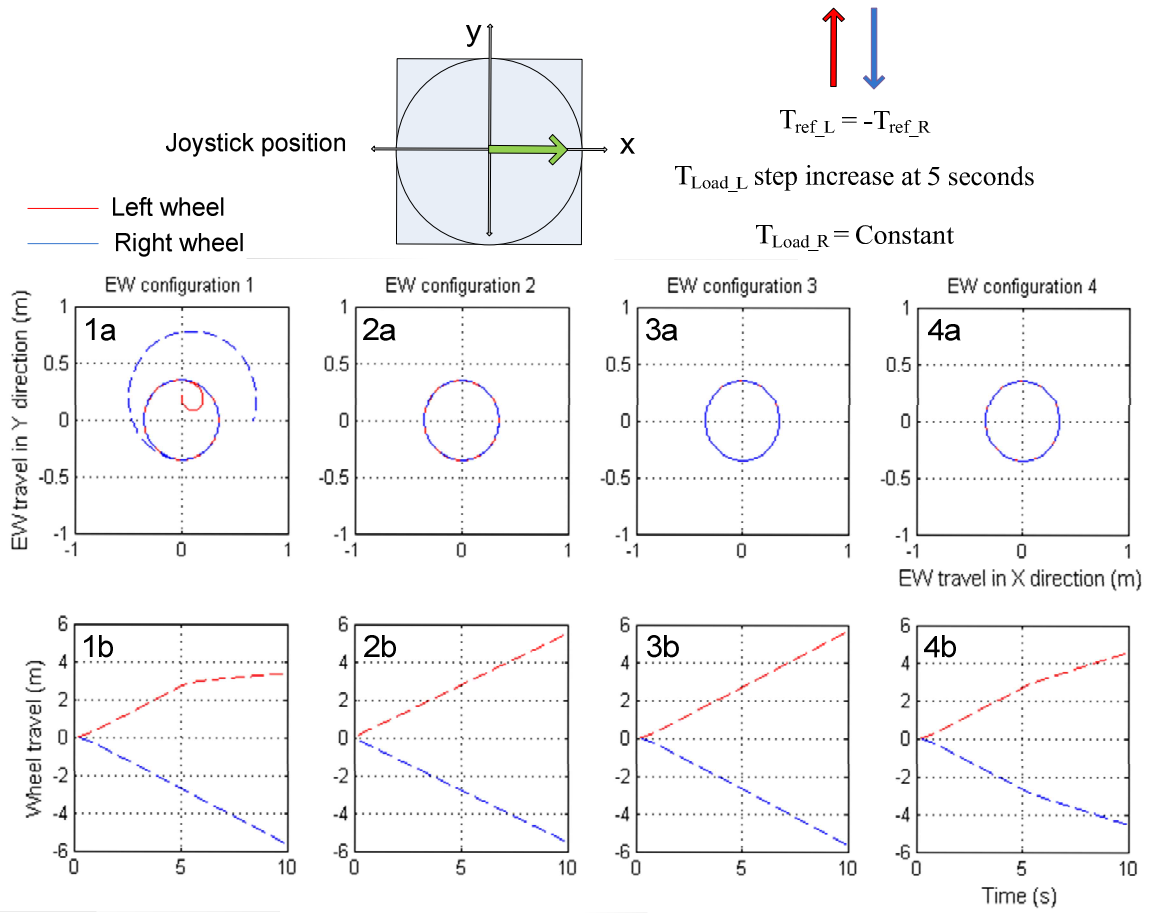
Figure 6.14 EW response - Simulation 3b, showing the EW response to a joystick position of 0° with a step load torque increase on the left wheel at 5 seconds.

6.4.1.8   Simulation 3c: Joystick position of 0° with a step load torque increase on the right wheel

Simulation 3c shows the EW response to a joystick position of 0° with a step load torque increase on the right wheel at 5 seconds.

Figure 6.15, 1b, 2b, 3b and 4b show the individual distance traveled by the left wheel (represented in red) and right wheel (represented in blue). The results in Figure 6.15, 1a, 2a, 3a and 4a, show the 2D motion of the EW as would appear from the top view. The left wheel (represented in red) and right wheel (represented in blue) have an equal but opposite offset from the zero point in the x direction, representing the wheel base (distance between wheels) of the EW. The equal and opposite speeds of the left and right wheels cause the EW to rotate in a clockwise circle (with the center of the EW as the pivot reference) showing that the motion of the EW tracks the joystick position of 0° until a load torque increase on the right wheel at 5 seconds.

- For configuration 1, consider Figure 6.15, 1a and 1b. The speed of the right motor decreases as the load torque is applied. Figure 6.15, 1b shows that the right motor speed decrease because the distance traveled decreases, but the left motor speed is unaffected. The result on the EW motion is that the diameter of the clockwise rotation increases and the pivot axis moves from the center of the EW towards the right wheel as shown in Figure 6.15, 1a. The criterion for EW directional tracking of the joystick irrespective of the load torque on either of the hub motors is thus not satisfied.

- For configuration 2 consider Figure 6.15, 2a and 2b. The right motor is under speed control, so when the load torque is applied there is no change to the motor speed and thus no decrease to the distance traveled in Figure 6.15, 2b. The criterion that the EW speed response is dependent on the load torque applied to either of the hub motors is thus not satisfied.

- For configuration 3 and 4 consider Figure 6.15, 3a, 3b, 4a and 4b. The speed of both the left and right motors decrease as the load torque is applied to the right motor. This is shown by the equal gradient reduction of the left and right motors distance graphs in Figure 6.15, 3b and 4b. The result on EW motion is that the joystick direction is accurately tracked (shown in Figure 6.15, 3a and 4a), and the speed deceases as a load is applied. This is an ideal response.
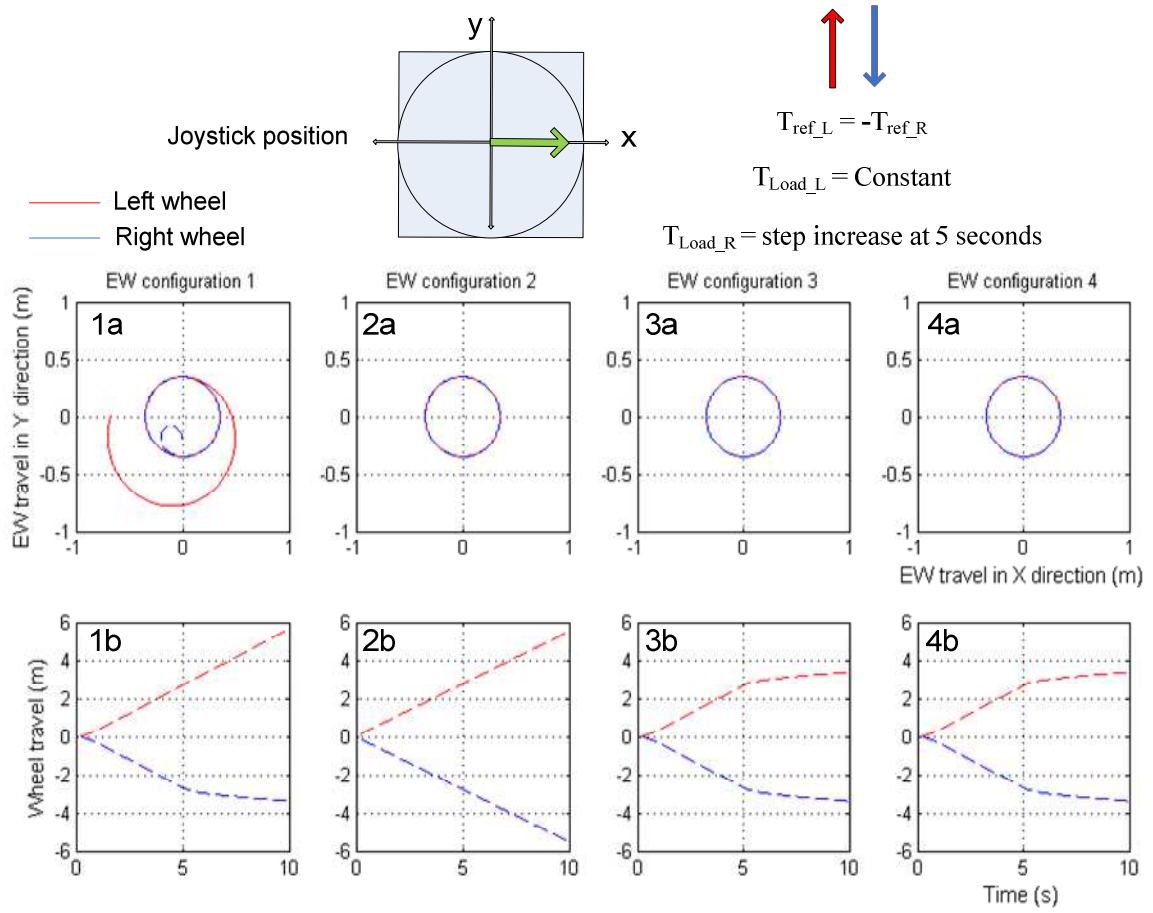
Figure 6.15 EW response - Simulation 3c, showing the EW response to a joystick position of 0° with a step load torque increase on the right wheel at 5 seconds.

6.4.1.9 Simulation 4a: Joystick position of 60° with left and right load torques equal and constant

Simulation 4a shows the EW response to a joystick position of 60° with left and right load torques equal and constant which represents ideal surface conditions.

The results in Figure 6.16, 1a, 2a, 3a and 4a, show the 2D motion of the EW as would appear from the top view. Both the left wheel (represented in red) and right wheel (represented in blue) have a forward speed, but the speed of the right wheel is less than the left wheel speed. The two wheels have an equal but opposite offset from the zero point in the x direction. This represents the wheel base (distance between wheels) of the EW. The resulting effect on the EW due to the right wheel speed being less than the left wheel speed is a gentle right hand cornering.

Figure 6.16, 1b, 2b, 3b and 4b show the distance traveled by the left wheel (represented in red) and right wheel (represented in blue). There is no load torque deviation throughout the simulation and thus the speed of the left and right wheels are constant. The resulting displacement plots for the left and right wheels are linear but with the gradient of the left wheel displacement being greater than that of the right wheel displacement.

The simulated response (gentle right hand cornering of the EW) is identical for each of the four EW configurations listed in Table 6.2, which is expected for ideal surface conditions.
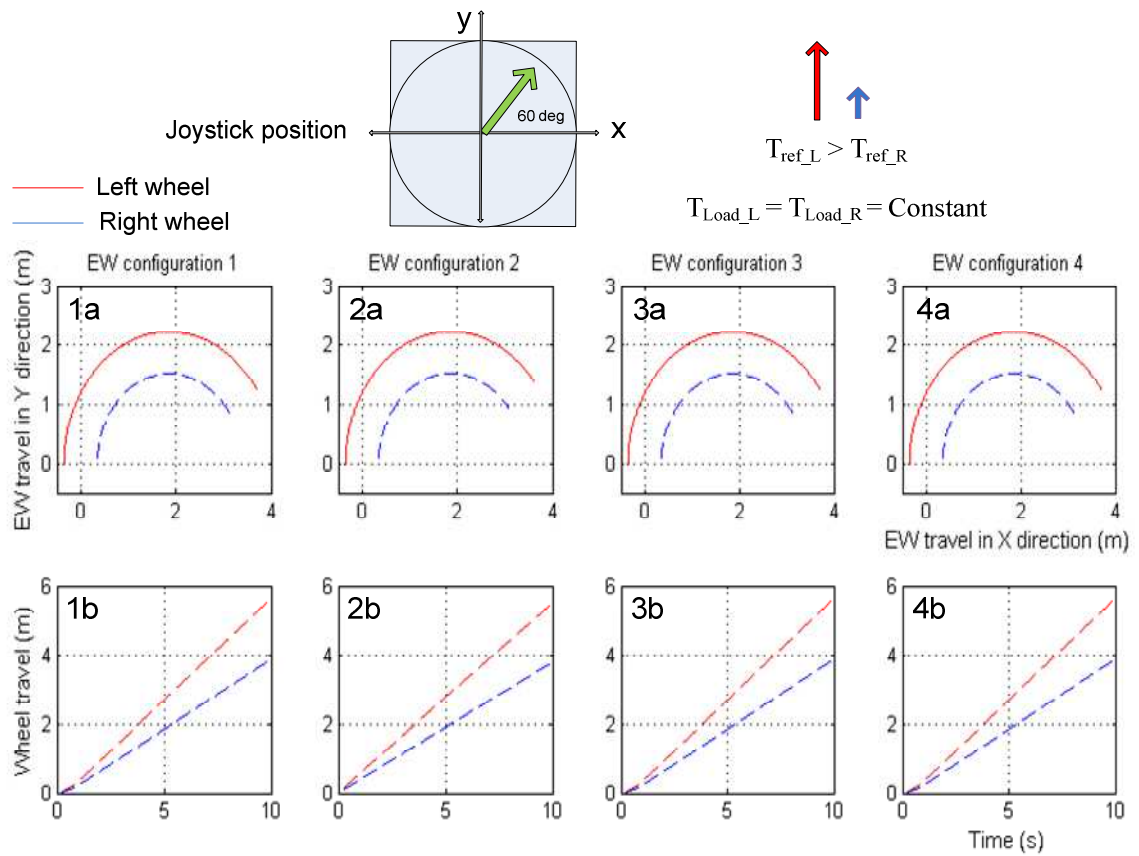
Figure 6.16 EW response - Simulation 4a, showing the EW response to a joystick position of 60° with left and right load torques equal and constant.

6.4.1.10 Simulation 4b: Joystick position of 60° with a step load torque increase on the left wheel

Simulation 4b shows the EW response to a joystick position of 60° with a step load torque increase on the left wheel at 5 seconds.

Figure 6.17, 1b, 2b, 3b and 4b show the individual distance traveled by the left wheel (represented in red) and right wheel (represented in blue). The results in Figure 6.17, 1a, 2a, 3a and 4a, show the 2D motion of the EW as would appear from the top view. The left wheel (represented in red) and right wheel (represented in blue) have an equal but opposite offset from the zero point in the x direction, representing the wheel base (distance between wheels) of the EW. The EW moves in a gentle right cornering motion because the right wheel speed is less than the left wheel speed. The 2D motion plot shows that the EW tracks the joystick position of 60° until a load torque increase on the left wheel at 5 seconds.

- For configuration 1, consider Figure 6.17, 1a and 1b. The speed of the left motor decreases as the load torque is applied. Figure 6.17, 1b shows that the left motor speed decreases because the distance traveled decreases, but the right motor speed is unaffected. The result on the EW motion is a sudden change from a right cornering motion to a left cornering motion as shown in Figure 6.17, 1a. The criterion for EW directional tracking of the joystick irrespective of the load torque on either of the hub motors is thus not satisfied.

- For configuration 2 and 3, consider Figure 6.17, 2a, 2b, 3a and 3b. The left motor is under speed control, so when the load torque is applied there is no change the motor speed and thus no decrease to the distance traveled in Figure 6.17, 2b and 3b. The criterion that the EW speed response is dependent on the load torque applied to either of the hub motors is thus not satisfied.

- For configuration 4 consider Figure 6.17, 4a and 4b. The speed of both the left and right motors decrease as the load torque is applied to the left motor. This is shown by the proportionally equal gradient reduction of the left and right motors distance graphs in Figure 6.17, 4b. The result on EW motion is that the joystick direction is accurately tracked (shown in Figure 6.17, 4a), and the speed deceases as a load is applied. This is an ideal response.
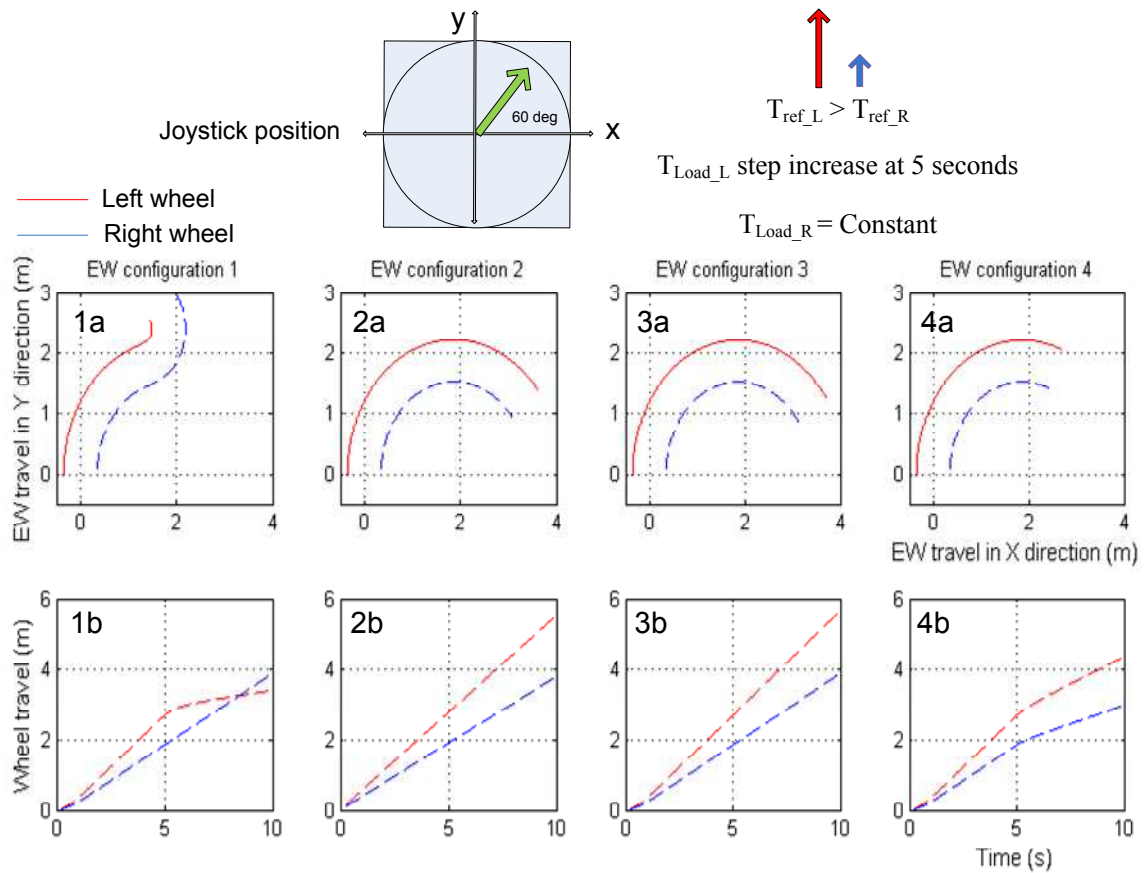
Figure 6.17 EW response - Simulation 4b, showing the EW response to a joystick position of 60° with a step load torque increase on the left wheel at 5 seconds.

6.4.1.11 Simulation 4c: Joystick position of 60° with a step load torque increase on the right wheel

Simulation 4c shows the EW response to a joystick position of 60° with a step load torque increase on the right wheel at 5 seconds.

Figure 6.18, 1b, 2b, 3b and 4b show the individual distances traveled by the left wheel (represented in red) and right wheel (represented in blue). The results in Figure 6.18, 1a, 2a, 3a and 4a, show the 2D motion of the EW as would appear from the top view. The left wheel (represented in red) and right wheel (represented in blue) have an equal but opposite offset from the zero point in the x direction, representing the wheel base (distance between wheels) of the EW. The EW moves in a gentle right cornering motion because the right wheel speed is less than the left wheel speed. The 2D motion plot shows that the EW tracks the joystick position of 60° until a load torque increase on the right wheel at 5 seconds.

- For configuration 1, consider Figure 6.18, 1a and 1b. The speed of the right motor decreases as the load torque is applied. Figure 6.18, 1b shows that the right motor speed decreases because the distance traveled decreases, but the left motor speed is unaffected. The result on the EW motion is a sudden change from a gentle right cornering motion to a hard right cornering motion as shown in Figure 6.18, 1a. The criterion for EW directional tracking of the joystick irrespective of the load torque on either of the hub motors is thus not satisfied.

- For configuration 2, consider Figure 6.18, 2a and 2b. The right motor is under speed control, so when the load torque is applied there is no change the motor speed and thus no decrease to the distance traveled in Figure 6.18, 2b. The criterion that the EW speed response is dependent on the load torque applied to either of the hub motors is thus not satisfied.

- For configuration 3 and 4 consider Figure 6.18, 3a, 3b, 4a and 4b. The speed of both the left and right motors decrease as the load torque is applied to the right motor. This is shown by the proportionally equal gradient reduction of the left and right motors distance graphs in Figure 6.18, 3b and 4b. The result on EW motion is that the joystick direction is accurately tracked (shown in Figure 6.18, 4a), and the speed deceases as a load is applied. This is an ideal response.
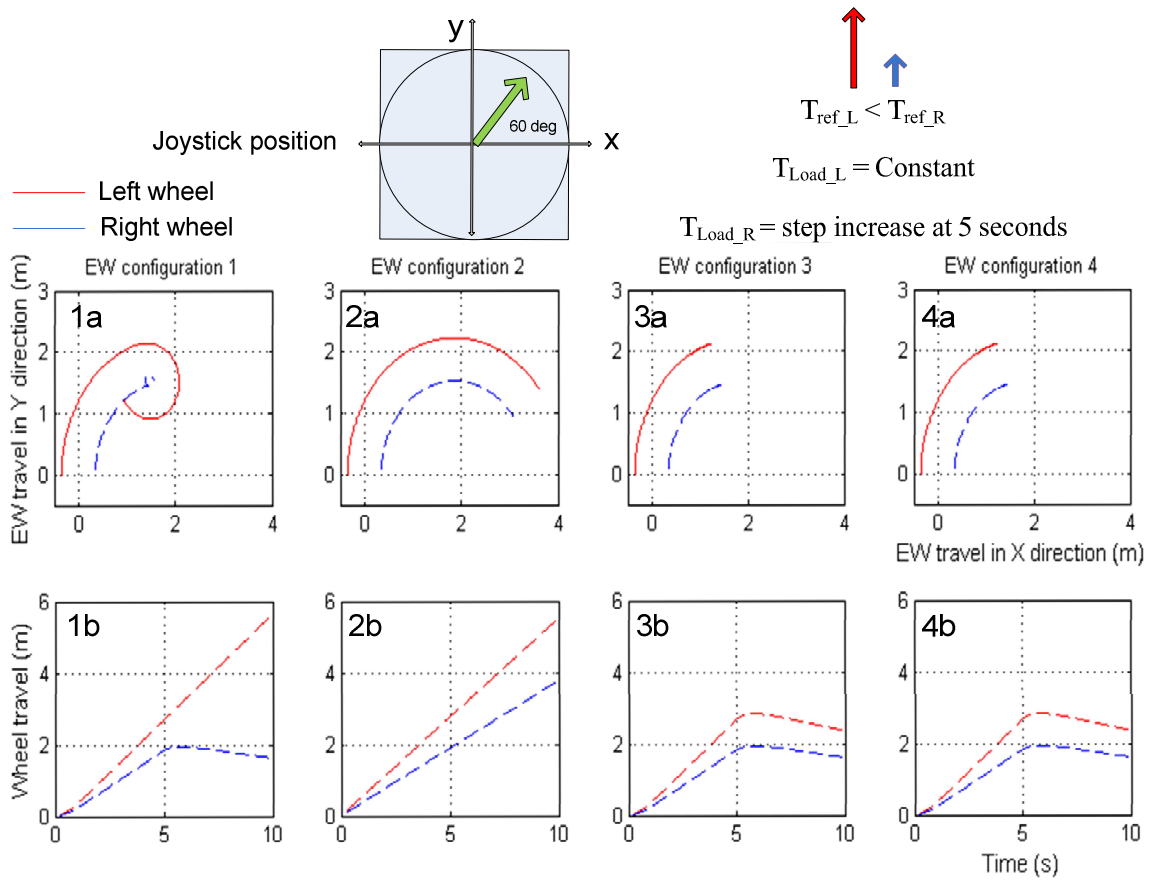
**Figure 6.18 EW response - Simulation 4c, showing the EW response to a joystick position of 60° with a step load torque increase on the right wheel at 5 seconds.**

6.4.2 Comparing different EW configurations for both direction tracking and speed response

To easily identify the benefits and shortfalls for each of the four EW configurations a summary of the simulation results is presented in Table 6.3. EW tracking is assessed based on the 2D plots in Figure 6.8 to Figure 6.18 1a, 2a, 3a, 4a. To assess the EW speed response, the distance plots for each wheel are used (Figure 6.8 to Figure 6.18 1b, 2b, 3b, 4b), this is possible because speed is the first integral of distance, so a change in speed is seen as a change in the gradient of the distance plot.

Table 6.3 EW configuration results summary for direction tracking and speed response

EW configuration summary	EW tracking	EW speed response
EW configuration 1 – This configuration has both left motor and right motor in independent torque control mode. Only in an equal T_l environment (such as smooth flat surfaces) does this control strategy meet both the EW controller criteria. When the load torque on either of the wheels experiences a disturbance, the EW direction changes and thus does not track the joystick. The criterion for the EW tracking however is met as the EW speed response depends on either of the hub motor load torques.	✖	✔
EW configuration 2 – This configuration has both left motor and right motor in independent speed control mode. The fundamental purpose for an EW having speed control on both hub motors is to achieve direction tracking. The EW speed response however is insensitive to any load increase (up to the EM peak electrical output torque capability). The criterion that the EW speed response is dependent on the load torque applied to either of the hub motors is thus not satisfied.	✔	✖

EW configuration 3 – This configuration has the right motor under torque control and the left motor under speed control, which is based on the joystick position and right motor speed. This configuration represents the first iteration of combining speed and torque control with the aim of meeting both criteria for an EW. If a load disturbance is experienced by the right hub motor, both criteria are always met. However when the disturbance occurs on the left hub motor, the disadvantage of speed control is present and the EW will not reduce speed as expected by the user. The criterion that the EW speed response is dependent on the load torque applied to either of the hub motors is thus not satisfied	✔	✘
EW configuration 4 – This configuration has the right motor under torque control and the left motor under speed control, which is based on the joystick position and right motor speed. This configuration represents the second iteration of combining speed and torque control and includes the implementation of a configurable low pass limiter which effectively transfers T_l changes from the left motor to the right motor. All the simulation results show good EW tracking. The EW response criterion is also met.	✔	✔

Table 6.3 above details the responses for each of the four EW configurations. Each utilizes a different control strategy. Only the fourth control strategy meets both criteria of EW direction tracking and EW speed response (provided that the peak motor output torque is not exceeded), as a result of transferring T_l changes from the left motor to the right motor by means of a user configurable limiter. The next section documents the effect the on the EW due to the limiter settings.

6.5   **Effect of the low pass limiter**

In Figure 6.6 low pass limiter is used to define the feedback from the left motor controller, to the right motor controller. The torque cut-off value for the low pass limiter is determined as follows.

$$T_{L\_limit_{MAX}} = (S_f + 100) * T_{L\_ref} \qquad (6.6)$$

When the left motor torque is limited, the magnitude for the adjusted right motor torque is determined as follows.

$$|T_{R\_adj}| = |T_{R\_ref}| - |(T_{L_{ref}} - T_{L\_limit_{MAX}})| \qquad (6.7)$$

where:

- $T_{L\_limit_{MAX}}$ is the maximum torque implemented by the low pass limiter (N-m).
- S_f is a user defined sensitivity factor for the left motor (-100% to + 100%).
- T_{R_adj} is the adjusted torque reference for the right motor (N-m).
- T_{R_ref} is the torque reference for the right motor from the joystick (N-m).
- T_{L_ref} is the torque reference for the left motor from the joystick (N-m).

Changing the value of S_f changes the EW speed response to a load torque on the left motor. The S_f value has no effect on the tracking of the joystick reference. Simulation 4b (response to a joystick position of 60° with a step load torque increase on the left wheel at 5 seconds) is repeated for EW configuration 4, but with different S_f values to show the effect on the EW speed response.

- For $S_f = 0\%$, consider Figure 6.19, 1a and 1b. This is the standard configuration for the limiter feedback. Any load on the left motor is directly transferred to the right motor. The EW will be equally responsive to a load on either left or right wheels. This simulation is used as a reference for comparing the change in EW response as the value for S_f is changed.
- For $S_f = 20\%$, consider Figure 6.19, 2a and 2b. The limiter setting allows an additional 20% in the left motor torque over the right motor and as a result speed control is prominent at all times. The EW will be less responsive to a load increase on the left motor. The distance plot in Figure 6.19, 2b shows a smaller gradient variation when compared to Figure 6.19, 1b resulting in the EW cornering for a further distance as seen when comparing the 2D plots for Figure 6.19, 2a and Figure 6.19, 1a.

- For $S_f = 5\%$, consider Figure 6.19, 3a and 3b. This limiter setting only allows an additional 5% in the left motor torque over the right motor and as a result speed control is only slightly prominent. The EW will be less responsive to a load increase on the left motor. The distance plot in Figure 6.19, 3b shows a smaller gradient variation when compared to Figure 6.19, 1b resulting in the EW cornering for a slightly further a distance as seen when comparing the 2D plots for Figure 6.19, 3a and Figure 6.19, 1a.

- For $S_f = -5\%$, consider Figure 6.19, 4a and 4b. The limiter setting reduces the left motor torque limit by 5% and as a results, the load torque transferred to the right motor is amplified. The EW will be more responsive to a load increase on the left motor. The distance plot in Figure 6.19, 4b shows a small gradient reduction when compared to Figure 6.19, 1b resulting in the EW cornering for less of a distance as seen when comparing the 2D plots for Figure 6.19, 4a and Figure 6.19, 1a.

- For $S_f = -20\%$, consider Figure 6.19, 5a and 5b. The limiter setting reduces the left motor torque limit by 20% and as a results, the load torque transferred to the right motor is amplified. The distance plot in Figure 6.19, 5b shows a large gradient reduction when compared to Figure 6.19, 1b resulting in the EW cornering for far less of a distance as seen when comparing the 2D plots for Figure 6.19, 4a and Figure 6.19, 1a. The EW is extremely responsive to a load increase on the left motor.

Table 6.4 EW response to user defined S_f

S_f (%)	EW response
$S_f < 0$	$T_L\_limit_{MAX}$ is reduced by the low pass limiter to a value less than T_L_ref. By reducing the toque limit, the EW is more responsive to loads on the left hub motor. To maintain tracking, the right motor will reduce speed when the left motor experiences an increase in load. This is an important feature for individuals whose disabilities hinder vision or awareness on the left hand side.
$S_f = 0$	$T_L\_limit_{MAX}$ is equal to T_L_ref. The response of the EW will be the same to a load irrespective of which hub motor it occurs on.
$S_f > 0$	$T_L\_limit_{MAX}$ is larger than T_L_ref. This allows speed control to be more prominent on the left motor, and able to maintain tracking without reducing the speed on the right motor. The sensitivity of a load on the left motor is reduced. This is an important feature for individuals whose disabilities hinder vision or awareness on the right hand

> side because the EW is more responsive to loads on the right motor. However if S_f is set too high, the EW response will tend towards that of control configuration 3.
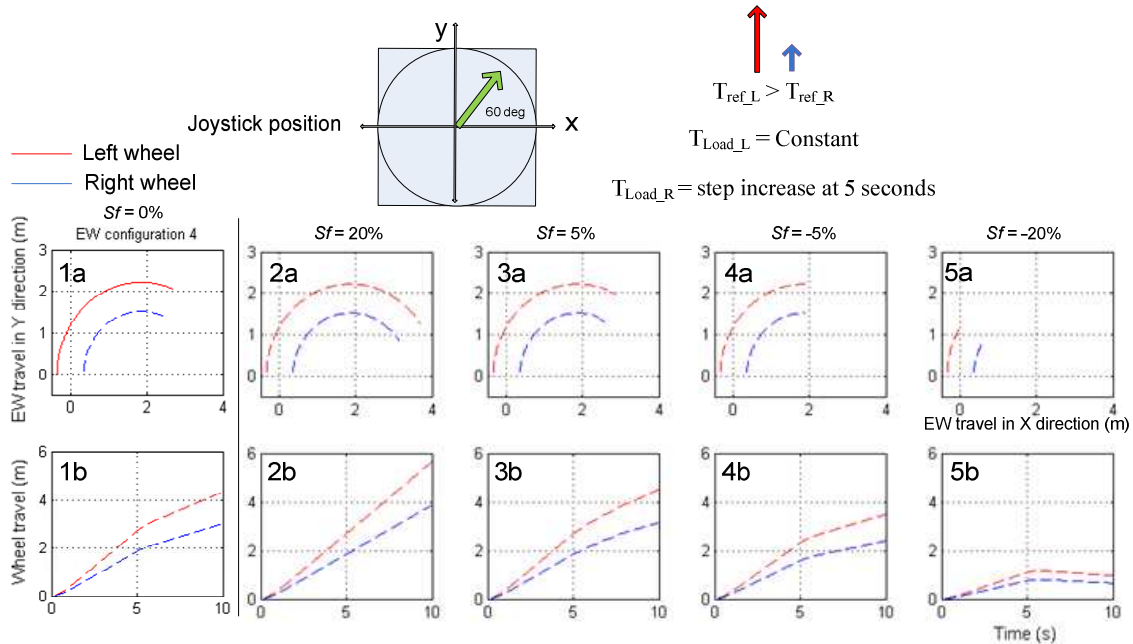
Figure 6.19 EW response variations due to different low pass limiter settings

6.6   **Summary**

The steering algorithm for an EW is the innovation in this chapter. Traditional configurations using torque or speed control show significant disadvantages. Neither can satisfy the two design requirements that the EW should give an intuitive response to the user for load disturbances on either of the hub motors, whilst providing direction tracking based on the user input. Finally a new control algorithm is proposed and the principle demonstrated by means of simulation. Due to limitations in hardware and time constraints, the solution has not been implemented on a full prototype electric wheelchair system. This is a topic for further work.

Chapter 7 - Conclusion and Further Work

_____

7.1   Introduction

With the continuous rise in both cost and demand of fossil fuels, research into environmentally friendly and efficient alternatives has been a large focus in recent years [1]. The general theme of this thesis revolves around electric motors as substitutes for the internal combustion engine in traction applications. Electric vehicles have progressed mainly due to the progression in electrical motor, power electronic and battery technology. The particular focus of this thesis is on the use of a controlled brushless DC hub motor (BLDCHM) system as applied to an electric wheelchair.

7.2   Investigation and contribution

A systematic approach towards the research, simulations and practical results was undertaken. This section summarizes each chapter's contents.

- Chapter 2 – Literature Review: This chapter described the available research regarding EV applications. The fields of research included motor and braking systems, torque control of various alternating current (AC) and direct current (DC) electric motors (EMs), motor drive technologies, energy sources and steering solutions. Based on the research a brushless DC hub motor was selected for this investigation, together with an appropriate power electronic circuit topology.

- Chapter 3 – BLDC Hub Motor Operation Theory: This chapter provided more detail on the BLDCHM selected in Chapter 2. The mechanical structure of the rotor and stator were described, as well as the position-based electrical commutation for driving this machine as a motor, and regenerating with it as a generator. The inverter topology and switching sequences were also developed.

- Chapter 4 – Dynamic and Electrical Model of a BLDCHM: In this chapter a mathematical analysis of the BLDCHM and the power electronics inverter was performed using an a,b,c reference axis approach for developing the equations. The final state space equation for a three-phase, star-wound, trapezoidal back EMF BLDCHM was obtained and the chapter also described the mechanical and electrical dynamic behavior of the BLDCHM.

- Chapter 5 – BLDCM Simulation and Controller Design: Based on the final state space equation developed in Chapter 4, a simulation model of the BLDCHM was developed using VisSim v6.0, a simulation package and embedded control developer from Texas Instruments®. A comparison of the simulated results for motor current, torque and rotational speed was compared to practical measurements on the motor and its inverter drive, illustrating the correct modeling and simulation of a BLDCHM. A torque controller based on current control was then designed and implemented on a Texas Instruments® DSP. Once again the simulated and practical results were compared. A sensorless torque controller during regeneration was then developed.

- Chapter 6 – Electric Vehicle Steering Algorithm: This chapter summarized the requirements for an electric wheelchair (EW) to have a response to the control input which is intuitive for the user. The traditional control systems in an EW were simulated and compared with two novel systems proposed in this research, which are designed to provide user vector tracking.

7.3   **Novel contribution**

The novel finding of this research is the development of a steering methodology for an EW with two BLDCHMs. It ensures that the wheelchair accurately tracks the directional command of the user, irrespective of differences in the smoothness of the individual terrains traversed by the left and right wheels. The control algorithm utilizes a torque controller on one motor and a speed controller on the other motor. Whilst this control configuration may not seem to be intuitive, when coupled with the designed control algorithm, all of the user requirements for an ergonomically acceptable driving experience, with direction tracking, are met.

7.4   **Objectives and further work**

The primary objectives were as follows:

a)   *The correct commutation and torque control of the motor.*
   - This objective was met. Chapter 3 documented the required commutation strategy for a BLDCHM. This strategy was practically implemented in Chapter 5, in which torque control loops were designed and implemented.

b)   *A commutation algorithm which provides two axis control (x and y directions) as the speed differential between the independent front hub motors is used to steer the EV.*

- This objective was met. Chapter 6 documented the novel contribution for this thesis which not only allows for steering of the EW, but also enables user vector tracking despite differences in the smoothness of the individual terrains traversed by the left and right wheels.

c) *Use of the system to increase battery life, thereby increasing the total travel distance of the EV.*

- This objective was met. Chapter 3 documented regenerative breaking by using the BLDCHM in generator mode. This recharged the batteries and thereby extended vehicle operating range.

d) *The implementation of a braking scheme which continues to allow for steering.*

- This objective was met. In Chapter 5 a sensorless torque controller was designed to operate during regeneration. The vector tracking algorithm described in Chapter 6 utilized this torque control to maintain steering during braking conditions.

The secondary objectives were as follows:

e) A complete prototype system solution to demonstrate the practical implementation.

f) The design and manufacturing of custom circuitry for both control and power electronics.

g) The solution should be robust, light weight and compact with low maintenance.

These objectives were not met and are considered as further work for this project. However implementation of traction control and an expansion to a four wheel drive system on a full scale electric vehicle, as a replacement for internal combustion transportation, is the ultimate progression for this research.

Appendix A   -   Parameter Identification of a BLDCHM

A1.   **Introduction**

This appendix describes the testing procedure used to determine the electrical and mechanical parameters of a star-wound, three-phase BLDCHM. Testing is performed at room temperature (22°C) to acquire the parameters for the final state space equation (SSE) below.

$$
\frac{d}{dt}\begin{bmatrix} I_a \\ I_b \\ I_c \\ \omega_m \\ \theta_e \end{bmatrix} = \begin{bmatrix} -R/L1 & 0 & 0 & -F_a(\theta_e)/L1 & 0 \\ 0 & -R/L1 & 0 & -F_b(\theta_e)/L1 & 0 \\ 0 & 0 & -R/L1 & -F_c(\theta_e)/L1 & 0 \\ F_a(\theta_e)/J & F_b(\theta_e)/J & F_c(\theta_e)/J & -B/J & 0 \\ 0 & 0 & 0 & P & 0 \end{bmatrix}\begin{bmatrix} I_a \\ I_b \\ I_c \\ \omega_m \\ \theta_e \end{bmatrix} + \begin{bmatrix} 1/L1 & 0 & 0 & 0 \\ 0 & 1/L1 & 0 & 0 \\ 0 & 0 & 1/L1 & 0 \\ 0 & 0 & 0 & -1/J \\ 0 & 0 & 0 & 0 \end{bmatrix}\begin{bmatrix} V_a \\ V_b \\ V_c \\ T_l \end{bmatrix} \quad (A.1)
$$

The state space equation is derived in Chapter 4 and is based on the BLDCHM equivalent circuit diagram in Figure A.2. The state variables are I_a, I_b, I_c, ωm and θ_m. The input variables are V_a, V_b, V_c, T_l.

A2.   **Instrumentation and parameter identification**

The evaluated parameters are described in Table A.1 and the testing equipment setup appears in Figure A.1, consisting of the following:

- Brushless DC hub motor (BLDHM) under test.
- Three phase induction motor (IM) used as a load motor.
- Siemens Micro Master 440 drive to control the IM.
- Torque Master TM 200 Series torque transducer.
- Leine & Linde 1024 quadrature ppr encoder connected to the IM.
- Custom built DC to three-phase inverter.
- eZdsp™TMS320F2812 development board with analogue cards.
- LEM PR30 current probe.
- Agilent 100Mhz oscilloscope (4-channel with BNC Probes).
- Lutron DM-9093 multimeter.
- Escort 3145A milli ohm meter.

- Fujitsu Siemens desktop computer.

The software required for the motor parameter testing consists of:

- Matlab® R2009a to simulate the motor and steering solution model, plot and evaluate the data.

- VisSim 6.0b9 to program the eZdsp™TMS320F2812 which controls the inverter.

- Drive Monitor to control and set parameters in the Siemens Micro Master 440 Drive.

- Auto Desk Inventor 9, a computer aided design package, to model the motor stator, and then calculate the mechanical inertia.
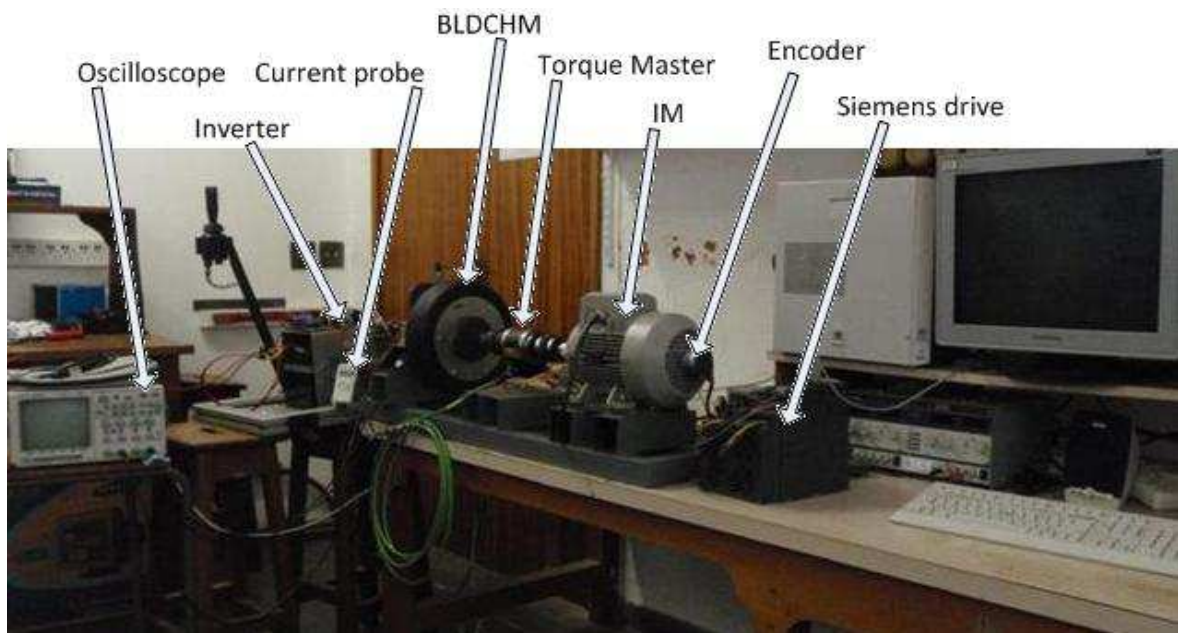
Figure A.1 Test bed setup
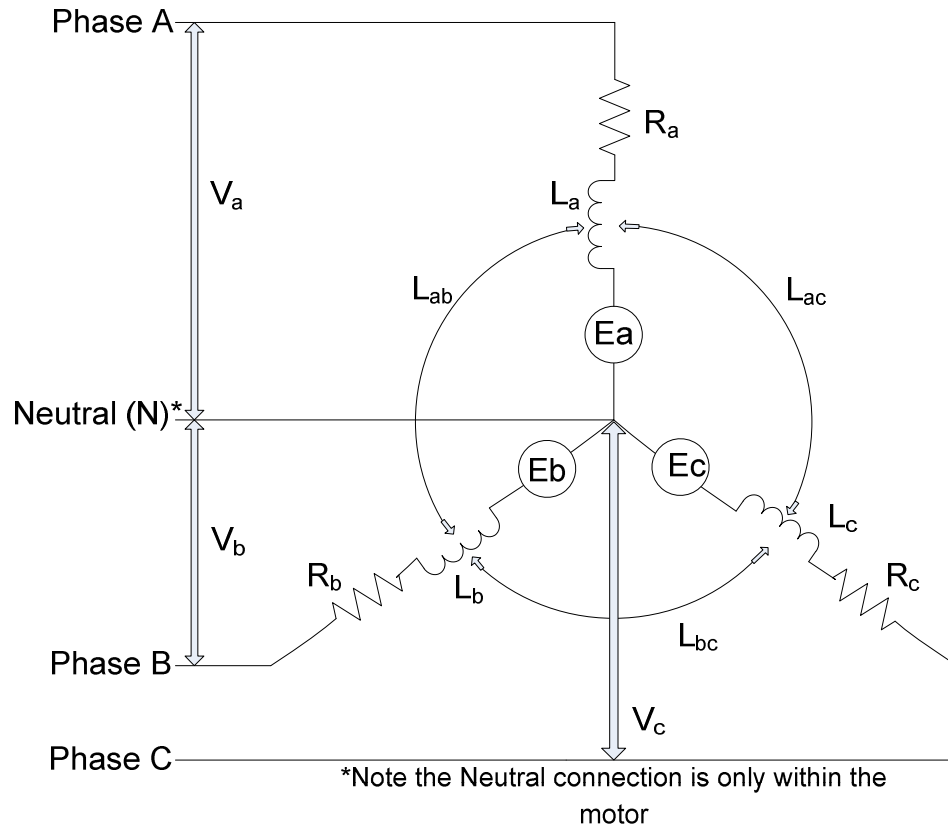
Figure A.2 BLDC equivalent circuit diagram [4]

Table A.1 BLDC motor parameters

	Parameter	Unit	Description
1.	P_r	W	Rated motor power (RMS)
2.	V_s	V	Supply voltage (RMS)
3.	I_r	A	Rated motor current (RMS)
4.	ω_b	rad/s	Motor mechanical base speed
5.	R	Ω	The individual phase resistances Ra, Rb, Rc and R (the average phase resistance to be used in the SSE)
6.	L	Henry	The individual phase inductances, La, Lb, Lc and L (the average phase inductances to be used in the SSE)
7.	L	Henry	The mutual inductance between phases, Lab, Lac, Lca and M (the average mutual inductances to be used in

			the SSE)
8.	J	kg.m^2	The inertia of the rotor
9.	P	-	The number of pole pairs thus: $[number\ of\ poles]/2$
10.	E	V	The back EMF generated by each phase, Ea, Eb and Ec
11.	K$_v$	V.s/rad	Motor speed constant
12.	K$_t$	N-m/A	Motor torque constant
13.	T$_r$	N-m	Rated motor torque
14.	B	N-m/rad.sec^{-1}	The coefficient of friction due to bearing and windage losses

A3.   **Motor parameter measurements**

1. The provided BLDCHM is a 500W motor form Brilliant Wheels, South Africa.
2. The supply consists of two 12V (18AH deep cycle lead acid batteries). Their peak charged potential is 12.5V, and are wired in series to produce a 25 V source.
3. The rated current is calculated from the rated power and supply voltage.

$$P_r = I_r * V_s \tag{A.2}$$

$$I_r = \frac{P_r}{V_s} = \frac{500}{25} = 20\ Amps \tag{A.3}$$

4. The base speed (ω_b) of the BLDCHM is defined as the maximum speed the motor will reach under no-load conditions and without the implementation of field-weakening techniques. To determine this parameter the inverter is used to ramp-up the phase voltages of the BLDCHM, under the standard 120 degree commutation strategy (using a PWM fed inverter as described in Chapter 3), until the phase voltages equal V_s. At this potential the steady state speed of $\omega_b = 14$ rad/sec is reached, and is shown in Figure A.3. The figure plots the analogue Hall effect sensors' feedback from within the BLDCHM and displays the calculated electrical and mechanical motor position, as well as the mechanical

rotational speed (ω_m). A filtered value of ω_m is also plotted and then used to obtain the value of ω_b.
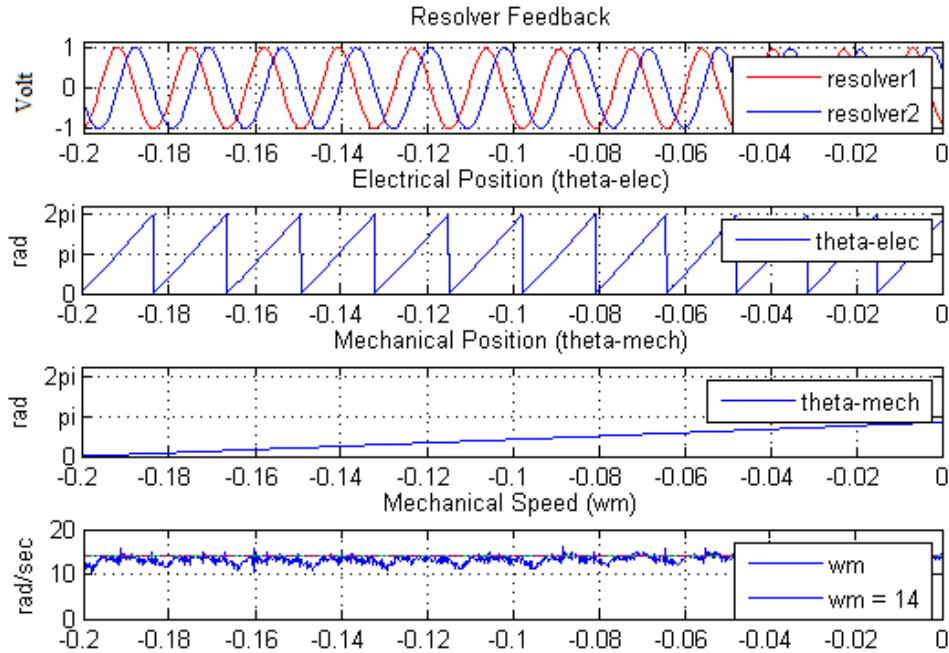
Figure A.3 Base speed estimation

5. The phase resistance is determined using an Escort 3145A milli ohm meter. The rotor is removed from the stator and a neutral point connection added (purely for monitoring purposes). The individual phase resistances are then measured (R_a, R_b, R_c) and appears in Table A.2, in which R is the average of the three phase values.

Table A.2 Phase resistances at 22° C

Phase	Resistance (Ω)
R_a	0.455
R_b	0.434
R_c	0.450
R	0.450

6. The phase inductance (or self-inductance) is determined using the Lutron DM-9093 inductance meter. The rotor is removed and each phase inductance (L_a, L_b and L_c) is

measured to the neutral point and documented in Table A.3, in which L is the average value of the three phase values.

Table A.3 Phase inductance at 22° C

Phase	Inductance (mH)
L_a	0.00148
L_b	0.00144
L_c	0.00159
L	0.0015

If the rotor is not removed from the stator, the phase inductance measurements are affected by the permanent magnet rotor. The effect is position dependent as shown in Figure A.4. This shows the importance of removing the rotor for inductance measurements, when permanent magnets are used in the motor construction. The values appearing in Table A.3 are used in this thesis.
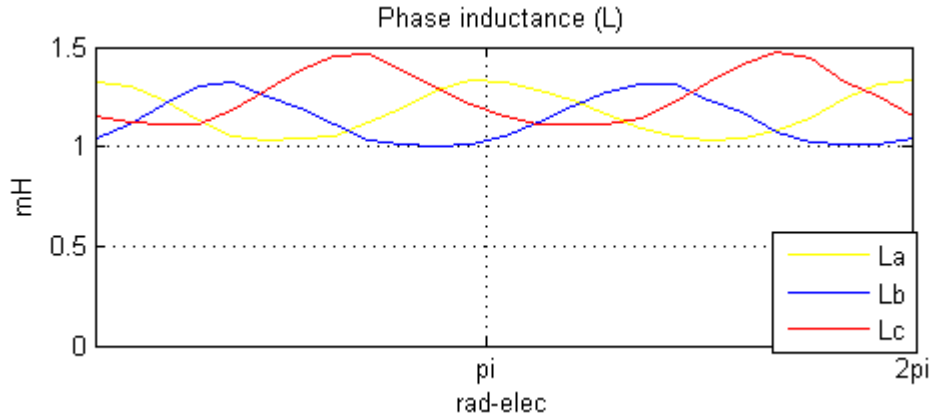
Figure A.4 Varying phase inductance measurements due to rotor permanent magnets

7. The mutual inductance between phases is measured with the rotor separated from the stator, by using the same Lutron inductance meter. The measurement is taken over two phases as total inductance (L_t) is the sum of each self-inductance and the mutual inductance between the two phases. For example:

$$L_t = L_a + L_b + L_{ab} \qquad (A.4)$$

$$L_{ab} = L_t - L_a - L_b \qquad (A.5)$$

The resulting mutual inductances in Table A.4 are determined in this manner.

Table A.4 Mutual inductances at 22° C

Phase	Inductance (mH)
L_{ab}	0.00002
L_{bc}	0.00005
L_{ca}	0.00004
L_m	0.000033

8. The inertia of the rotor is a property of the mass and distance between the mass and the centre of rotation. The mathematical equation to determine inertia for a rotating disk with a hole in the centre is shown below [34].

$$J = 0.5 * mass * (a^2 + b^2) \tag{A.6}$$

Where *a* and *b* are the inner and outer radii respectively in meters and the mass is in kg. Implementing this equation over a complex profile becomes difficult. Auto Desk Inventor, a computer aided design program, is used to model the rotor structurally, with each component's mass inserted, allowing the package to accurately calculate the inertia. The final 3D model is shown in Figure A.5 and the resulting model produces a value of 0.04335 kg.m^2.
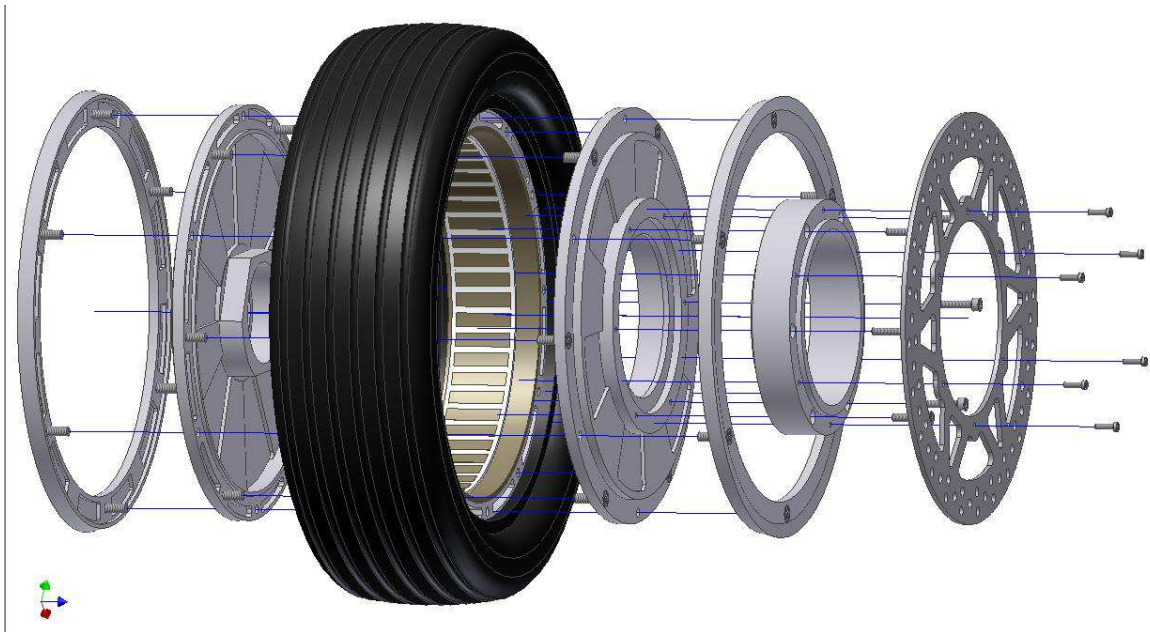
Figure A.5 Autodesk 3D model of the rotor to determine inertia.

9. The total number of 56 poles is determined by counting the magnets within the rotor and thus the number of pole pairs is P = 28.

10. To obtain the back EMF waveforms for the BLDCHM, the IM acts as a driving motor and an oscilloscope is used to capture the potentials from the neutral connection to each phase terminal of the BLDCHM. The expected waves are trapezoidal but the measured waves have sinusoidal properties. This is as a result of the high pole count and appears in Figure A.6. To accurately represent the back EMF for simulation, a hybrid waveform is obtained by imposing a sinusoidal wave onto the back EMF wave.
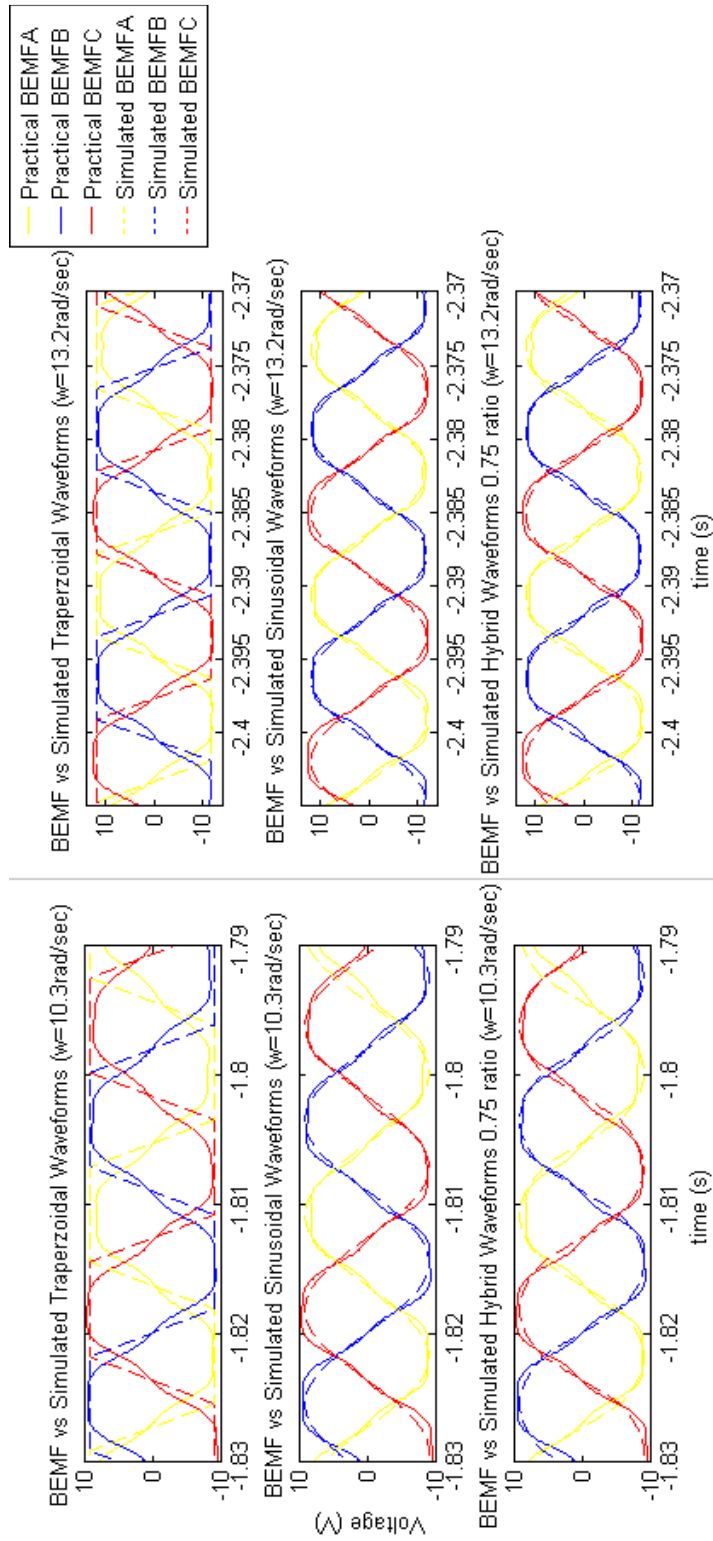
Figure A.6 Back EMF wave form estimation

11. The speed constant is the proportional factor between the mechanical motor speed and the amplitude of the back EMF waveforms at that speed. The base speed is determined above and the back EMF potential is acquired using the test-bed in Figure A.1. The IM is used to rotate the BLDM at 14rad/sec and the peak potential for the back EMF is measured to be 12.81 V. Thus

$$K_v = \frac{|E|}{\omega_b} = \frac{12.81}{14} = 0.915 \, V.s/rad \tag{A.7}$$

12. The motor torque constant relates the BLDCHM phase currents to the output torque. To determine this value, the inverter supplies V_s to the motor. The BLDCHM is coupled through the torque transducer, to the IM which is driven in vector speed control mode as a load. The test begins at the BLDCM base speed and is ramped down to stand still. The output torque and inverter current for the BLDCM will increase as the speed decreases and these values are logged and compared. An offset of 1.3 Amps for the current is required, representing the electrical torque needed to overcome frictional losses in (A.1). A torque constant is then calculated to be 1.2 N-m/A based on the data shown in Figure A.7 which displays the data from four independent practical tests in order to validate consistency of the derived equation. The noise seen on the current signal is due to the PWM switching on the inverter and the 120 degree commutation strategy of the BLDCHM as described in Chapter 3.
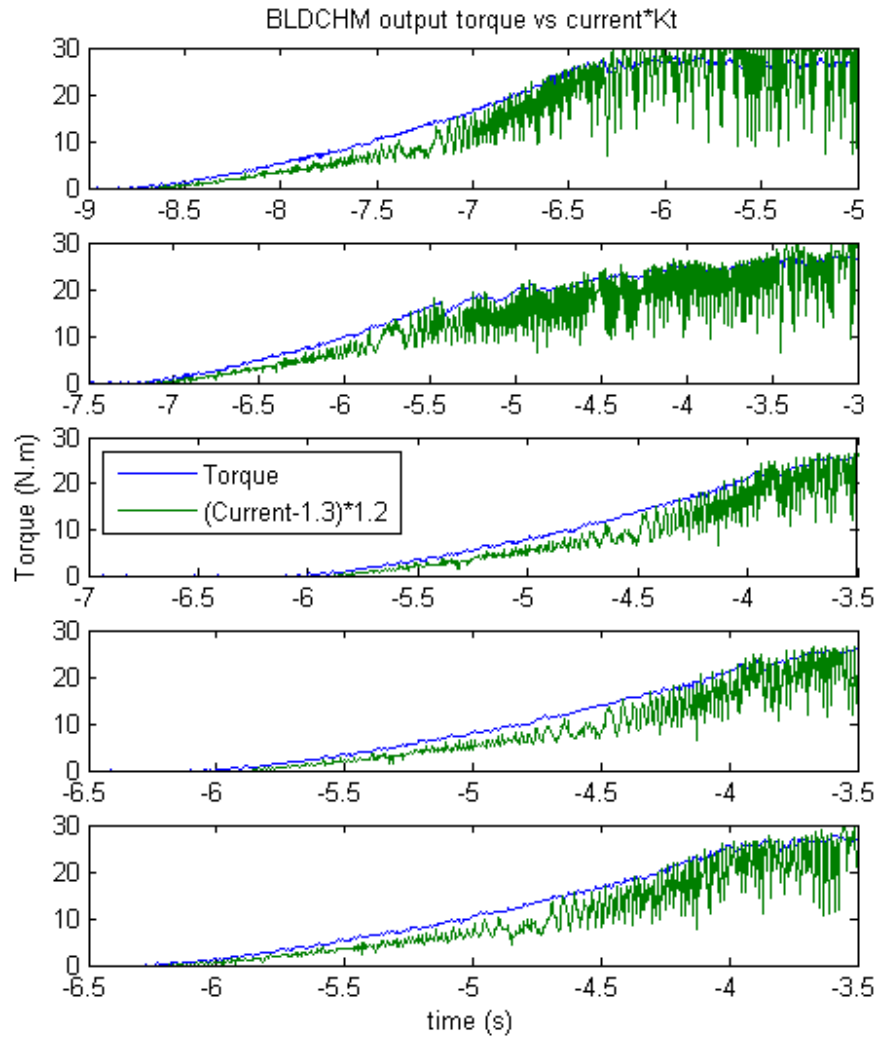
Figure A.7 K_t relating current to output torque

13. The rated motor torque (RMS) is defined and calculated using the rated current (RMS) and motor torque constant.

$$T_r = I_r * K_t = 1.2 * 20.833 = 25\ N - m \tag{A.8}$$

14. The mechanical equation for motion of the BLDCHM is shown below and is used to determine the coefficient of friction B.

$$J\left[\frac{d\omega_m}{dt}\right] + B\omega_m = T_e - T_l \qquad (A.9)$$

The coefficient of friction is determined at steady state base speed. This reduces the mechanical equation for the BLDCHM to (A.1), as the speed is constant and no load is applied. The measured current is 0.6 Amps and the base speed is 14 rad/sec.

$$B = \frac{T_e}{\omega_b} = \left[\frac{I * K_t}{\omega_b}\right] = 0.0514 \; N - m/rad.sec^{-1} \qquad (A.10)$$

A4.   **Summary**

This appendix lists the BLDCHM parameters, as well as the testing equipment and the test-bed configuration required to perform the necessary testing. The method for determining each parameter is discussed and the data is evaluated to determine the final values.

Appendix B   -   BLDCHM Transfer Functions

B1.   **Introduction**

This appendix describes the Matlab® script used to determine the transfer function of the total current in a brushless DC hub motor (BLDCHM) with respect to the input voltage. The result is based on a 120-degree commutation strategy, where only two of the three phases conduct at any moment in time. Based on this, the phase resistance and inductance values are double the individual phase resistance and inductance values measured in Appendix A.

B2.   **Matlab® script**

```
%Title: Transfer Functions for the BLDCHM

%Description: This Matlab script shows the code used to determine the
BLDCHM transfer function based on the statespace equations (SSE)
developed in section 5.4
%The motor is operated in 120 degree commutation mode, so two phases
conduct at any point in time.

%Author: Bradley Shields

%These are the motor constants measured in Appendix A
L = 3e-3;        %Armature Inductance
R = 0.9;         %Armature Resistance
Kv = 0.9;        %Machine Constant
J = 0.04335;     %Machine Load & Inertia
beta = 0.05;     %Machine Viscous Friction
TL = 10;          %Load Torque

%Below the A, B, C and D matrices for the SSE are developed
A = [-R / L, -Kv / L; Kv / J, -beta/J];
B = [1 / L, 0; 0, -1/J];
C = [1, 0; 0, 1];
D = [0, 0; 0, 0];

%Below the transfer functions for total current (I) and mechanical speed
(spd) are developed with respect to the inverter voltage (V).
[num, den] = ss2tf (A, B, C, D, 1);
tf_V2I = tf (num (1,:), den); %current
tf_V2spd = tf (num (2,:), den); %torque
```

```
%Below the transfer functions for total current (I) and mechanical speed
(spd) are developed with respect to the load torque (TL).
[num, den] = ss2tf (A, B, C, D, 2);
tf_TL2I = tf (num (1,:), den); %current
tf_TL2spd = tf (num (2,:), den); %torque


%The VisSim simulated current and the Matlab transfer function are
compared
%in VisSim. The data is saved to a file and imported below.
importdatfile('E:\masters\matlab\simulation_vs_transfer_function.dat');
Simulated_I = data(:,1);    %this is the VisSim simulated current
Transfer_function_I = data(:,2);    %this is the Matlab transfer function
time = linspace(0, 0.3, 300);


%This section of code creates a new figure (with limited screen size)
%the figure shows both the VisSim and Matlab estimation with labled axes.
scrsz = get(0,'ScreenSize');
figure('OuterPosition',[1 scrsz(4)/3 scrsz(3)/2.2 scrsz(4)/1.85])
plot(time, Transfer_function_I, 'r', time, Simulated_I, 'b');
h = legend('Transfer Function','Simulated',2);
set(h,'Location','SouthEast', 'Orientation','Vertical')
ylabel('Current (Amps)');
xlabel('Time (s)');
ylim ([0 18])
xlim ([0 0.3])
grid
```
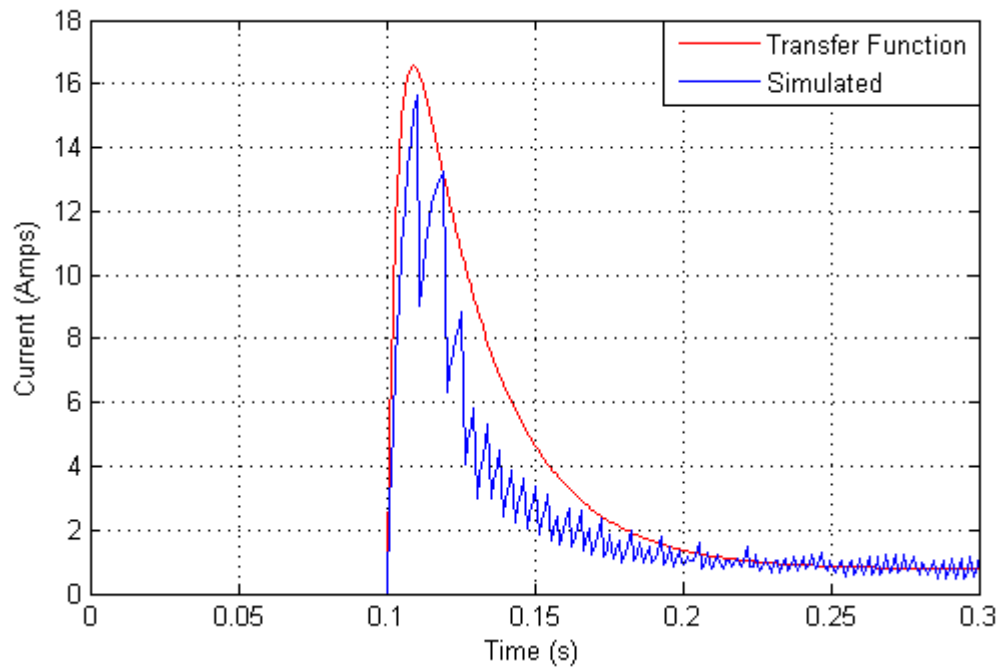
Figure B.8 Current step response to 20V supply

$$Gp(s) = TF\_V2I = \frac{333.3\,s\;+\;384.5}{s2\;+\;301.2\,s\;+\;6574} \qquad\qquad\text{(B.1)}$$

B3.   **Summary**

This appendix describes the Matlab® script used to determine the transfer function of input voltage to output current in a BLDCHM. The transfer function is shown in B.1, and the response is compared to the VisSim controller response (The VisSim controller is developed in Chapter 5). As expected ((B.1) does not take into account the phase commutation and thus produces a smooth current response.

Appendix C   -   Fourth-Order Regeneration Polynomial

C1.   **Introduction**

The implementation for regenerative torque control in the brushless DC hub motor (BLDCHM) can be implemented using any one of three strategies. The first strategy is direct torque control with a transducer supplying feedback to the controller. The second strategy is current control. This is effective because the output torque is directly proportional to the individual phase currents. The third strategy is implemented using a lookup table. It is not practical for a BLDCHM, on an electric vehicle (EV) to have a torque transducer, thus eliminating the first strategy. The hardware implementation for the EV has only one current transducer, thus eliminating the second strategy. The third strategy is therefore implemented in the form of a fourth order polynomial equation as developed in Chapter 5. This Appendix provides details of the regeneration polynomial which has an RR value of 0.8741.

C2.   **Polynomial estimations of the modified regeneration properties**
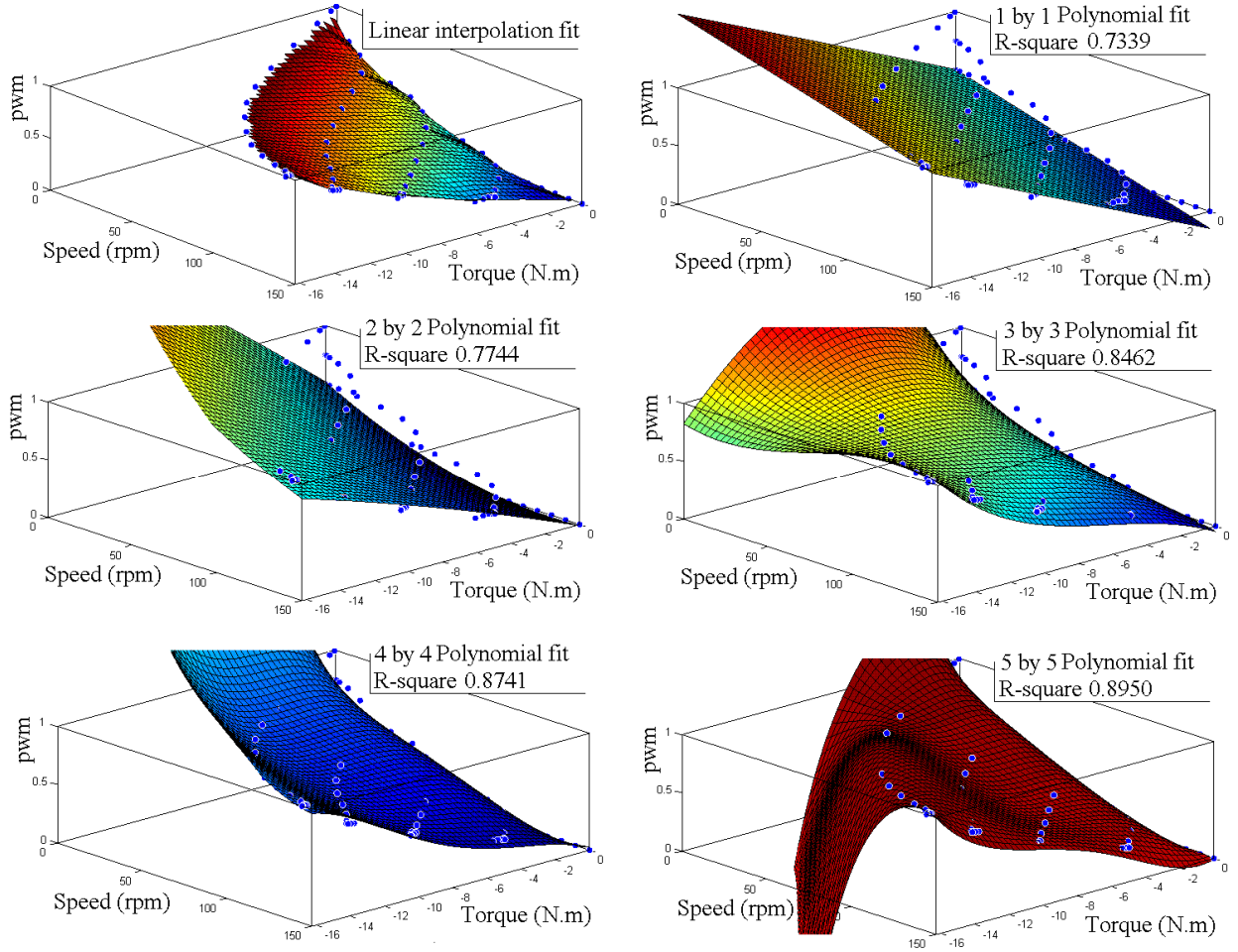
Figure C.9 Polynomial estimations of the modified regeneration properties

The traces above are discussed in section 5.4 and the 4-by-4 polynomial fit is selected. The output is limited between an upper value of one, and a lower value of zero as these are the bounds for the inverter pulse-width-modulation (PWM) mark-to-space ratio. The equation for the fourth-order polynomial is:

$$f(x,y) = \begin{aligned} &p00 + \\ &(p10 * x + p01 * y) + \\ &(p20 * x^2 + p11 * x * y + p02 * y^2) + \\ &(p30 * x^3 + p21 * x^2 * y + p12 * x * y^2 + p03 * y^3) + \\ &(p40 * x^4 + p31 * x^3 * y + p22 * x^2 * y^2 + p13 * x * y^3 + p04 * y^4) \end{aligned} \qquad (C1)$$

where:

- *x* is the rotational speed (rpm).
- *y* is the regeneration torque reference (N-m).
- *f(x,y)* is the inverter pulse-width-modulation mark-to-space ratio.

The coefficients for the polynomial equation are:

p00	=	0.7139
p10	=	-0.3436
p01	=	-0.1086
p20	=	-0.0695
p11	=	-0.06621
p02	=	-0.3486
p30	=	-0.07003
p21	=	-0.05388
p12	=	0.2395
p03	=	-0.399
p40	=	0.0731
p31	=	0.04395
p22	=	0.1091
p13	=	0.2363
p04	=	-0.0588

C3.   **Summary**

A fourth order polynomial equation has been developed to implement deceleration toque control during regeneration. Based on the BLDCHM speed and the torque references, the correct PWM ratio is applied to the inverter.

References

[1]   C.C. Chan. "The State of the Art of Electric and Hybrid Vehicles," Proceedings of the IEEE, Vol. 9, No.2, pp. 247–275, Feb. 2002.

[2]   Y. Hori, "Future Vehicle Driven by Electricity and Control – Research on Four-Wheel-Motored UOT Electric March II," IEEE Transactions on Industrial Electronics, Vol. 51, No. 5, pp. 954-962, Oct. 2004.

[3]   D. Xue, K. Cheng and N. Cheung, "Selection of Electric Motor Drives for Electric Vehicles," IEEE Power Engineering Conference, AUPEC '08, Australasian Universities, Sydney, pp. 1-6, Dec. 2008.

[4]   M.T. Wishart, "Field Orientated Control of AC Machines with Particular Reference to Permanent Magnet AC Machines," MScEng Thesis Submitted to The University of Natal, Jan. 1991.

[5]   A. de Almeinda, F. Ferreira, J. Fony and P. Fonseca, "EUP LOT11-Motors," University of Coimbra, Portugal, Feb. 2008.

[6]   D. Rai, "Brushless DC Motor Simulink Simulator," Department of Electronics and Communication Engineering, National Institute of Technology Karnataka, India.

[7]   P. Pillay and R. Krishnan, "Modeling, Simulation and Analysis of High Performance, Vector Controlled, Permanent Magnet Synchronous Machine," IEEE Transactions on Industry Applications, Vol. 25, No. 2, pp. 265-272, Mar./Apr. 1989.

[8]   W. Brown, Microchip Technologies Inc. "Brushless DC Motor Control Made Easy", Application Note AN857, DS00857A, Jan. 2002.

[9]   P. Pillay, Y. Liu and T. Sebastian, "Multi Phase Operation of Switched Reluctance Motor Drives," IEEE Industrial Application Conference, New Orleans, Vol. 1, pp. 310-317, Oct. 1997.

[10]   IEEE Power Engineering Society, "IEEE Standard Test Procedure for Polyphase Induction Machines and Generators," Electric Machines Committee of the IEEE Power Engineering Society, ISBN 1-55937-891-3, 1997.

[11]   C. Kleinhans, "Simulation and Practical Implementation of Field Orientated Control on the Current-Fed Induction Motor," MScEng Thesis Submitted to The University of Natal, May 1995.

[12]   G. Diana and R. Harley, "An Aid For Teaching Field Oriented Control Applied to Induction Machines," IEEE Transactions on Power Systems, Vol. 4, No. 3, pp. 1258-1262, Aug. 1989.

[13]   P. Kraus, "Analysis of Electrical Machinery," Wiley IEEE Press Series on Power Engineering, ISBN-10: 0780311019, Oct. 1995.

[14]   S. Wang, "Modeling and Torque Control Implementation for an 8/6 Switched Reluctance Motor," MScEng Thesis Submitted to The University of Natal, 2006.

[15]   I. Husain and M. Ehsani, "Torque Ripple Minimization in Switched Reluctance Motor Drives by PWM Current Control," IEEE Transactions on Power Electronics, Vol. 11, No. 1, pp. 72-77, Jan. 1996.

[16]   F. Soares and P.C. Branco, "Simulation of a 6/4 Switched Reluctance Motor Based on Matlab/Simulink Environment," IEEE Transactions on Aerospace and Electronic Systems, Vol. 37, No. 3, pp. 989-1009, Jul. 2001.

[17]   M. Rashid, "Power Electronics Handbook," 3rd Edition, ISBN-13: 978-0-12-382036-5, Oct. 2010.

[18] A. Wintrich, U. Nicolai, W. Tursky and T. Reimann "Application Manual Power Semiconductors," Semikron International, ISBN 978-3-938843-66-6, 2011.

[19] S. Vukosavic and V.R. Stefanovic, "SRM inverter topology: A Comparative Evaluation," IEEE Industry Applications Society Annual Meeting, ISBN: 0-87942-553-9, pp. 946-958, Oct. 1990.

[20] A. Kusko, "Solid-State DC Motor Drives," The MIT Press, Cambridge, Massachusetts and London, ISBN 0262-11031-8, 1969.

[21] S. Pay and Y. Baghzouz, "Effectiveness of Battery-Supercapacitor Combinations in Electric Vehicles," IEEE Power Tech Conference, Vol. 3, Bologna, pp. 42-46, Jun. 2003.

[22] E. Ozatary, B. Zile, J. Anstrom and S. Brennan, "Power Distribution Control Coordinating Ultracapacitors and Batteries for Electric Vehicles," Proceedings of the American Controls Conference, Vol. 5, Boston, pp. 4716-4721, Jun./Jul. 2004.

[23] T. Guilin, M. Zhiyun, Z. Libing and L. Langru, "A novel driving and control system for direct-wheel-driven electric vehicle," IEEE Electromagnetic Launch Technology Symposium, Snowbird, pp. 514-517, May 2005.

[24] E. Muljadi and J. Green, "Cogging Torque Reduction in a Permanent Magnet Wind Turbine Generator," Presented at the 21st American Society of Mechanical Engineers Wind Energy Symposium Reno, Nevada, January 2002.

[25] A. Guermazi, M. Sahbi, A. Masmoundi and A. Elantably, "On the Analysis and Control of Four-Switch Three-Phase Inverter fed Brushless Motor Drives," The International Journal for Computation and Mathematics in Electrical and Electronic Engineering, Vol. 26, No. 5, pp.1247-1261, Jan. 2007.

[26]   D. Ohm and J. Park. "About Commutation and Current Control methods for Brushless Motors," Drivetech Research, Blacksburg, Virginia and Virginia Polytechnic Institute and State University, Presented at the 29th IMCSD (Incremental Motion Control Systems and Devises) Symposium, San Jose, Jul. 1999.

[27]   Y Jani. "Implementing Embedded Speed Control For BLDC Motors", Renesas Technology America, Presented at the Embedded Systems Control Conference, Boston, Sep. 2006.

[28]   D.G. Dorrel, D.A. Staton, J. Hahout, D. Hawkins and M.I. McGlip. "Linked Electromagnetic and Thermo Model of Permanent Magnet Motor," IEEE Power Electronics, Machines and Drives, 3rd IET International Conference, pp. 536-554, Mar. 2006.

[29]   J. Dixon and A. Leal, "Current Control Strategy for Brushless DC Motors Based on a Common DC Signal," IEEE Transactions on Power Electronics, Vol. 17, No. 2, pp. 232-240, Mar. 2002.

[30]   C. Jia-Xin, J. Jian-Zhong and W. Xian-Yao, "Research of Energy Regeneration Technology in Electric Vehicles," Journal of Shanghai University, Vol. 7, No. 2, pp. 173-177, June 2003.

[31]   T. Chen, T. Ren, Y. Chen and Y. Lou, "Driving and Regenerative Braking of Brushless DC Motor for Energy-Saving Wheel Motor," SICE (Society of Instrument and Control Engineers) Annual Conference, Taiwan, pp. 2654-2659, Aug. 2010.

[32]   K. Ogata, "Discrete-Time Control Systems," 2nd Edition, ISBN 0130342815, Jan. 1995.

[33]   S. Ozturk, W. Alexander and H. Toliyat, "Direct Torque Control of Four-Switch Brushless DC Motor with Non-sinusoidal Back-EMF," IEEE Power Electronics Specialist Conference (PESC 2008), Rhodes, ISSN : 0275-9306, pp. 4730-4736, Jun. 2008.

[34]   H.D. Young and R.A. Freedman, "University Physics," 9th Edition, Addison Wesley Publishing Company, ISBN 0-201-84769-8, Sep. 1995.

[35]   A. Sattar, "Insulated Gate Bipolar Transistor (IGBT) Basics," IXYS Corporation, Application note Ixan 0063, pp. 1-15, 2008.

[36]   L. Liu, W. Liu and D. Cartes, "Permanent Magnet Synchronous Motor Parameter Identification using Particle Swarm Optimization," International Journal of Computational Intelligence Research, ISSN 0973-1873 Vol.4, No.2, pp. 211-218, 2008.

[37]   P. Luk and P. Jinupun, "A Novel In-wheel Switched Reluctance Motor," IEEE Vehicle Power and Propulsion Conference, Windsor, pp. 1-5, Sep. 2006.

[38]   S. Mehta and J. Chiasson, "Nonlinear Control of a Series DC Motor: Theory and Experiment," IEEE Transactions on Industrial Electronics, Aachen, Vol. 45, No. 1, pp. 134-142, Feb. 1998.

[39]   C. Gencer and M. Gedikpinar, "Modeling and simulation of BLDCM using MATLAB/SIMULINK," Journal of Applied Sciences, ISSN 1812-5654, pp. 688-691, 2006.

[40]   G. Su, J. McKeever and K. Samson, "Modular PM Motor Drives for Automotive Traction Applications". The 27th Annual Conference of the IEEE Industrial Electronics Society, IECON '01, Denver, Vol. 1, pp. 119-124, 2001.